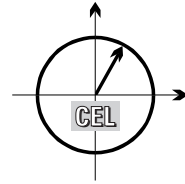


■ *Forschungsberichte aus dem
Institut für Nachrichtentechnik des
Karlsruher Instituts für Technologie*



Martin Braun

■ **OFDM Radar Algorithms in Mobile Communication Networks**

■ Band 31

Copyright: Institut für Nachrichtentechnik (CEL)
Karlsruher Institut für Technologie (KIT)
2014

Druck: Frick Digitaldruck
Brühlstraße 6
86381 Krumbach

ISSN: 1433-3821

**Forschungsberichte aus dem Institut für Nachrichtentechnik
des Karlsruher Instituts für Technologie**

Herausgeber: Prof. Dr. rer. nat. Friedrich Jondral

- Band 1 Marcel Kohl
**Simulationsmodelle für die Bewertung von
Satellitenübertragungsstrecken im
20/30 GHz Bereich**
- Band 2 Christoph Delfs
**Zeit-Frequenz-Signalanalyse: Lineare und
quadratische Verfahren sowie vergleichende
Untersuchungen zur Klassifikation von Klaviertönen**
- Band 3 Gunnar Wetzker
**Maximum-Likelihood Akquisition von Direct
Sequence Spread-Spectrum Signalen**
- Band 4 Anne Wiesler
**Parametergesteuertes Software Radio
für Mobilfunksysteme**
- Band 5 Karl Lütjen
**Systeme und Verfahren für strukturelle
Musteranalysen mit Produktionsnetzen**
- Band 6 Ralf Machauer
Multicode-Detektion im UMTS
- Band 7 Gunther M. A. Sessler
**Schnell konvergierender Polynomial Expansion
Multiuser Detektor mit niedriger Komplexität**
- Band 8 Henrik Schober
**Breitbandige OFDM Funkübertragung bei
hohen Teilnehmergegeschwindigkeiten**
- Band 9 Arnd-Ragnar Rhiemeier
Modulares Software Defined Radio
- Band 10 Mustafa Mengüç Öner
**Air Interface Identification for
Software Radio Systems**

**Forschungsberichte aus dem Institut für Nachrichtentechnik
des Karlsruher Instituts für Technologie**
Herausgeber: Prof. Dr. rer. nat. Friedrich Jondral

- Band 11 Fatih Çapar
**Dynamische Spektrumverwaltung und
elektronische Echtzeitvermarktung von
Funkspektren in Hotspotnetzen**
- Band 12 Ihan Martoyo
Frequency Domain Equalization in CDMA Detection
- Band 13 Timo Weiß
OFDM-basiertes Spectrum Pooling
- Band 14 Wojciech Kuropatwiński-Kaiser
**MIMO-Demonstrator basierend
auf GSM-Komponenten**
- Band 15 Piotr Rykaczewski
**Quadratureempfänger für Software Defined Radios:
Kompensation von Gleichlauf Fehlern**
- Band 16 Michael Eisenacher
Optimierung von Ultra-Wideband-Signalen (UWB)
- Band 17 Clemens Klöck
Auction-based Medium Access Control
- Band 18 Martin Henkel
**Architektur eines DRM-Empfängers
und Basisbandalgorithmen zur Frequenzakquisition
und Kanalschätzung**
- Band 19 Stefan Edinger
**Mehrträgerverfahren mit dynamisch-adaptiver
Modulation zur unterbrechungsfreien
Datenübertragung in Störfällen**
- Band 20 Volker Blaschke
Multiband Cognitive Radio-Systeme

**Forschungsberichte aus dem Institut für Nachrichtentechnik
des Karlsruher Instituts für Technologie**

Herausgeber: Prof. Dr. rer. nat. Friedrich Jondral

- Band 21 Ulrich Berthold
**Dynamic Spectrum Access using OFDM-based
Overlay Systems**
- Band 22 Sinja Brandes
**Suppression of Mutual Interference in
OFDM-based Overlay Systems**
- Band 23 Christian Körner
**Cognitive Radio – Kanalsegmentierung und
Schätzung von Periodizitäten**
- Band 24 Tobias Renk
**Cooperative Communications: Network Design and
Incremental Relaying**
- Band 25 Dennis Burgkhardt
**Dynamische Reallokation von spektralen Ressourcen
in einem hierarchischen Auktionssystem**
- Band 26 Stefan Nagel
**Portable Waveform Development for
Software Defined Radios**
- Band 27 Hanns-Ulrich Dehner
**Interferenzuntersuchungen für inkohärente
Multiband Ultra-Breitband (UWB) Übertragung**
- Band 28 Maximilian Hauske
Signalverarbeitung für optoelektronische Sensoren
- Band 29 Jens Elsner
**Interference Mitigation in
Frequency Hopping Ad Hoc Networks**
- Band 30 Georg Vallant
**Modellbasierte Entzerrung
von Analog/Digital-Wandler-Systemen**
- Band 31 Martin Braun
**OFDM Radar Algorithms in
Mobile Communication Networks**

Vorwort des Herausgebers

Vor zwanzig Jahren wurden mit dem Begriff Radar (*Radio Detection and Ranging*) fast ausschließlich teure, komplexe Systeme zur Schifffahrts-, Flug- und Landverkehrsüberwachung, manchmal auch zur Steuerung sowie zur Abwehr von Marschflugkörpern, verbunden. Aufgrund ihrer Kostenstruktur war die klassische Radarindustrie zur Entwicklung und Fertigung von Radargeräten für den Massenmarkt nicht in der Lage. Dafür ist es der Kraftfahrzeugzuliefererindustrie gelungen, kostengünstige und zuverlässige Abstandswarnradare auf den Markt zu bringen. Seitdem ist der Trend, Radargeräte breitflächig als Sensoren in Fahrzeugen, in der Automatisierungstechnik und in anderen Bereichen des täglichen Lebens einzusetzen, nicht mehr aufzuhalten. Gleichzeitig wird erforscht, welchen Nutzen der Einsatz von Fahrzeug-zu-Fahrzeug Funkkommunikation z.B. für die Verkehrssicherheit oder die Verkehrslenkung haben könnte. Da Radar und Funkkommunikation elektromagnetische Wellen benutzen, die von den jeweiligen Verkehrspartnern reflektiert bzw. empfangen werden, liegt die Idee nahe, beide Aufgaben simultan mit demselben Gerät auf derselben Welle durchzuführen. Als durchaus gewünschter Nebeneffekt stellt sich dabei ein, dass ein solches System offensichtliche Vorteile bezüglich einer ökonomischen Frequenznutzung bietet.

Die erfolgreiche gemeinsame Bearbeitung beider Aufgaben setzt voraus, dass ein Übertragungsverfahren identifiziert wird, das simultan sowohl für Radar- als auch für Kommunikationsaufgaben nutzbar ist. Wichtige Randbedingungen sind dabei die erreichbare Abstands- und Geschwindigkeitsauflösung für das Radar und die Mehrnutzerfähigkeit für die Kommunikation. Die in der vorliegenden Dissertation verfolgte Lösung setzt auf OFDM (*Orthogonal Frequency Division Multiplex*), ein Übertragungsverfahren, das bereits in erfolgreichen Standards der Funkkommunikation (z.B. IEEE 802.11a, LTE) genutzt wird. OFDM Radarsysteme werden seit mehreren Jahren untersucht und auch über die gemeinsame Realisierung von Radarsensorik und Funkkommunikation mit OFDM-Signalen wurde bereits gearbeitet und berichtet.¹

Um einen erfolgversprechenden Lösungsweg beschreiten zu können, müssen darüber hinaus grundsätzliche Fragen zum vernetzten Zusammenspiel beider Komponenten geklärt werden. Hierzu gehört insbesondere, dass die benötigte Signalverarbeitung auf ein tragfähiges theoretisches Fundament gestellt und der Ad-hoc Charakter sowie die zufällige, zeitvariante Topologie eines Radar-/Kommunikationsnetzes berücksichtigt werden. Die Arbeit von Martin Braun legt im Kapitel 3 das Fundament für die Signalverarbeitung mit Methoden der Fouriertransformation, der Wahrscheinlichkeitsrechnung und der Statistik, die während eines zeitgemäßen Studiums der Elektrotechnik und Informationstechnik vermittelt werden. Der Ad-hoc Charakter und die zufällige, zeitvariante Netztopologie werden, wie in Kapitel 4 dargestellt, durch Anwendung von Ergebnissen aus der stochastischen Geometrie, deren Kenntnis weit über das normale Studium hinausgeht und die auch in Karlsruhe ein aktueller Gegenstand mathematischer Forschung ist,² berücksichtigt. Die gewählte Vorgehensweise führt unter anderem dazu, dass statistische Aussagen über die Netzausfallwahrscheinlichkeit abgeleitet werden können, die dann ihrerseits zur optimalen Parameterwahl für das zur simultanen Nutzung von Radar und Funk auf derselben elektromagnetischen Welle eingesetzte OFDM System beitragen.

Karlsruhe, im Januar 2014
Friedrich Jondral

¹Christian Sturm: *Gemeinsame Realisierung von Radarsensorik und Funkkommunikation mit OFDM-Signalen*. Karlsruher Forschungsberichte aus dem Institut für Hochfrequenztechnik und Elektronik, Band 66, 2011

²Siehe: <http://www.math.kit.edu/stoch/seite/raumstoch>

OFDM Radar Algorithms in Mobile Communication Networks

Zur Erlangung des akademischen Grades eines

DOKTOR-INGENIEURS

von der Fakultät für

Elektrotechnik und Informationstechnik

des Karlsruher Instituts für Technologie

genehmigte

DISSERTATION

von

Dipl.-Ing. Klaus Martin Braun

geb. in

Speyer

Tag der mündlichen Prüfung:

23. Januar 2014

Hauptreferent:

Prof. Dr. rer. nat. Friedrich K. Jondral

Korreferent:

Prof. Dr.-Ing. Gerd Wanielik

Acknowledgements

Five years and two months – this is the time it took from my first day at the Communications Engineering Lab until handing in this thesis. It would not have happened as smoothly (or maybe never at all) had it not been for the help of certain people, and I would like to use this opportunity to thank them.

My advisor Prof. Dr.rer.nat. Friedrich Jondral has certainly had a great influence not only on the success of my dissertation, but also on my career. He was the one who introduced me to the fascinating topic of software defined radio, a field in which I am still working even after my time at CEL – although I admit the more interesting lessons I learned from him were not actually related to engineering at all! I would also like to thank Prof. Dr.-Ing. Gerd Wanielik for being the second advisor for my thesis and his interest in my work.

I very much enjoyed working with all of my colleagues at CEL. During my time there, I shared an office with Jens Elsner and Ankit Kaushik, who were always open for discussions and exchanging ideas, as well as Angelika Olbrich, who was a great help getting my slides sorted out. I would also like to thank Dr.-Ing. Holger Jäkel for many cups of tea, reminding me to go swimming and most importantly for discussing my

research – he pointed out a lot of loose ends and inconsistencies in my research which I would not have found otherwise. Ralph Tanbourgi introduced me to the topic of stochastic geometry, for which I am very grateful, and without him, this thesis' Chapter 4 would certainly have looked a lot different! Beate Mast and Brigitte Single were always patient when paperwork was incomplete, or important administrative tasks had to be done quickly, and I would like to thank them as well. It says a lot about a job when you can both discuss work as well as have a good time outside of the lab with all of your colleagues, and for me, this was certainly true at CEL. Apart from those previously mentioned, I would like to thank (in order of office numbers) Noha El Gemayel, Michael Mühlhaus, Dennis Burgkhardt, Sebastian Koslowski, Michael Schwall, Stefan Nagel, Johannes Fink, and Fabrizio Massaro for all the great times we had.

During my time as a PhD candidate, I had the opportunity to mentor many students on their way to getting a degree. Most of the time, I enjoyed this a lot, and while I can't say if I was of any help to them, some of them were definitely an inspiration to me. In particular, I would like to thank Gerald Baier, Johannes Demel, Moritz Fischer, Manuel Fuhr, Marcus Müller and Nico Otterbach for very insightful discussions and wish them all the best for their future endeavours.

My thanks go beyond those at CEL, though. My involvement in the GNU Radio project has helped me, in many ways, to become a better engineer, and I would like to thank all who are part of this great project. The notion that participating in free software projects is a waste of time is ridiculous and could not be further from the truth.

Finally, my thanks go out to my family, who was always supportive of my career choices (and still is). My parents continue to claim that they never actually did anything to help me with my endeavours – I say that seems unlikely. My wife Judith was always and continues to be a source of motivation, inspiration, and fun. It's a good thing we both were working on our dissertations at the same time, and I hope I can express my thanks by being equally supportive.

Zusammenfassung

Radarsysteme haben sich auf ähnliche Art und Weise verändert wie der Mobilfunk. Was einst teure und nur einem beschränkten Nutzerkreis zugängliche Technologie war, ist heute allgemein zugänglich. Radar-Sensoren sind billiger geworden, haben eine geringere Leistungsaufnahme und sind in vielen verschiedenen Anwendungsgebieten anzutreffen, sowohl in Bereichen der Industrieautomation bis hin zu Consumer-Anwendungen wie beispielsweise Autos.

Viele dieser Anwendungen profitieren auch von der Möglichkeit, kommunizieren zu können. Da drahtlose Kommunikation und Radar ähnlichen Prinzipien unterliegen – beide senden und empfangen elektromagnetische Wellen – ist es naheliegend zu versuchen, beide Komponenten in einem einzigen Gerät zu vereinigen. Solch ein kombiniertes System würde weniger Hardware benötigen, weniger Energie verbrauchen und weniger Spektrum belegen als zwei getrennte Systeme. All diese Eigenschaften sind in Massenanwendungen von großem Vorteil.

Eine Lösung hierfür ist es, OFDM als Wellenform zu verwenden, was heutzutage in vielen Kommunikationsstandards bereits üblich ist. OFDM-basiertes Radar wurde im letzten Jahrzehnt mehrfach vorgeschlagen; einige wesentliche Fragen hierzu sind allerdings bislang unbeantwortet.

In dieser Arbeit werden zwei Aspekte von OFDM-basiertem Radar untersucht. Der erste bezieht sich auf die Signalverarbeitung bei OFDM-Radar: Ausgehend von einem gesendeten und einem empfangenen rückgestreuten Signal, was ist die optimale Vorgehensweise um eine Liste von Radar-Zielen zu erhalten? Die in dieser Arbeit verwendeten Algorithmen knüpfen teilweise an vorangehende Arbeiten an, die hier vorgestellten Ergebnisse sind allerdings ein erster Versuch, den zugrundeliegenden Schätzprozess vollständig zu beschreiben und zu bewerten und beinhalten eine umfassende Beschreibung aller Komponenten der Zieldetektion. Die gewonnenen Erkenntnisse können u.a. bei der Implementierung verwendet werden, liefern aber insbesondere eine Grundlage zur Bewertung von Signalparametrisierungen. In der vorliegenden Arbeit wird beispielsweise die Verwendung von Signalen wie sie in WLANs eingesetzt werden diskutiert.

Ein wesentlicher Grund OFDM als Wellenform einzusetzen ist die Option gleichzeitig zum Radarbetrieb Kommunikation betreiben zu können. In diesem Fall bilden mehrere OFDM-basierte Knoten ein drahtloses Kommunikationsnetzwerk, was allerdings zwangsläufig dazu führt, dass die Datenübertragungen anderer Knoten die eigene Radarbildgebung stören.

Der zweite hier untersuchte Aspekt von OFDM-Radar ist daher die Analyse des Einfluss der Eigeninterferenzen. Es wird eine neue Metrik eingeführt, welche die Leistungsfähigkeit von OFDM-Radar-Netzwerken im Bezug auf diese Interferenzen beschreibt: die *Radarnetzwerk-Ausfallwahrscheinlichkeit (radar network outage)*. In manchen Fällen können analytische Ausdrücke gewonnen werden, welche als gute Approximation für diese neue Metrik verwendet werden können.

Alle Ergebnisse wurden mit Simulationen und teilweise auch mit Messungen verifiziert. Insgesamt kann eine gute Anwendbarkeit von OFDM für kombinierte Radar- und Kommunikationssysteme bestätigt werden.

Abstract

Radar systems have changed in a similar way to mobile communications. What once used to be expensive technology, restricted to a limited circle of users, has become accessible to anyone. Radar sensors have become cheaper, less power-consuming and can be found in many different applications, ranging from industrial automation to consumer products such as automobiles.

Many of these applications also require communication capabilities, and given the similarities between the nature of wireless data transmission and radar – both emit and receive electromagnetic waves – it is an obvious question to ask if both components could be combined into a single device. Such a combined system would require less hardware, less power and allocate less spectrum – all of these characteristics being highly desirable in mass-produced technology.

One solution for this is to use OFDM waveforms, which nowadays are commonly used in communications standards already. OFDM-based radar has been suggested several times independently in the last decade, but many important questions remain unanswered.

In this work, two aspects of OFDM-based radar are analyzed. The first is the signal processing side of OFDM radar: Given a transmitted and received signal, what is the best way to compute a list of targets? While the results here build on previously suggested algorithms, this work is a first attempt to fully understand the properties of the underlying estimation process, and features a comprehensive description of all parts of the target detection.

This helps not only with the implementation of OFDM radar, but also with evaluation of signal parametrizations. As an example, OFDM waveforms used in wireless LAN signals are analyzed with regard to their radar capabilities.

One major reason to choose OFDM is to enable communications simultaneously to the radar operation. In this case, multiple OFDM-based nodes will form a network to transmit data, but at the same time, the transmissions from the other systems will interfere with the radar sensing.

The second aspect of OFDM radar analyzed in this work is this impairment through co-channel interference. A new metric, the *radar network outage*, is introduced to describe the performance of OFDM radar in presence of such interference. For certain cases, it is possible to derive an analytical expression which can be used as a close approximation for this metric.

All results are verified with simulations and some measurements, all of which suggest high applicability of OFDM for combined radar and communication systems.

Contents

1	Introduction	1
1.1	Background	2
1.2	Outline	2
2	Radar Sensing and Communication Networks	4
2.1	Vehicular networks	5
2.2	Radar Systems	6
2.2.1	Mutual interference in radar networks	8
2.3	Combined Communication and Radar systems	9
3	OFDM Radar Algorithms	11
3.1	Physical structure of an OFDM signal	11
3.1.1	PAPR	16
3.2	The OFDM radar estimation problem	18
3.2.1	Accuracy of the sinusoidal model	22
3.2.2	Unambiguous ranges	24
3.3	Periodogram-based estimation algorithms	24
3.3.1	Signal-to-noise ratio and processing gain	26
3.3.2	Efficient calculation of the periodogram	30
3.3.3	Estimation theoretic observations	31

3.3.4	Window functions	41
3.3.5	Quantization issues and interpolation	45
3.3.6	Signal detection and false alarm rate	52
3.3.7	Multi-target detection	55
3.3.8	Non-contiguous sub-carrier allocations	62
3.4	Parametric target estimation	72
3.4.1	ESPRIT	72
3.4.2	Comparison	76
3.5	Non-spectral estimation based algorithms	77
3.6	Signal Parametrization	78
3.6.1	Constraints and Requirements	79
3.6.2	Examples for parameter sets	83
3.6.3	Frame Design and Channel Coding	90
4	Multi-user OFDM Radar networks	95
4.1	Multi-user access	96
4.1.1	Practical considerations	98
4.2	Radar network outage	98
4.3	Interference model	100
4.3.1	Influence of directivity	102
4.4	Analytical bounds	104
4.4.1	Stochastic modeling	105
4.4.2	Outage probability analysis	106
4.4.3	Empirical verification	111
4.5	Consequences for the system parametrization	112
4.5.1	Network feasibility study	115
4.5.2	Evaluation of the detection performance	116
4.5.3	Choice of sub-carrier spacing	120
5	Radar performance verification	121
5.1	Simulation and Measurement Tools	121
5.1.1	Simulation Control	123
5.1.2	Simulated Environment	123
5.1.3	Software Radio-based Measurement Setup	126
5.1.4	Radar Estimator	127
5.1.5	Evaluation	130
5.2	Single-node radar performance	131
5.2.1	Single-target accuracy	132
5.2.2	Multi-target accuracy	139
5.3	Multi-node performance	141

6 Conclusion	144
6.1 Contributions	144
6.2 Future Applications	145
A Influence of modulation schemes with variable amplitude	147
B Quadratic Interpolation	150
Notations & Symbols	153
Abbreviations	156
Bibliography	158
Supervised Theses	170
Index	173
Curriculum Vitae	176

1

Introduction

Not too long ago, both wireless communications and radar systems involved either expensive terminals or large infrastructure. On the communication side, this changed with the advent of cellular networks, when it became possible to manufacture mobile wireless terminals very cheaply. Further development, in particular on side of transceiver ICs, continued this trend up to a point where nowadays most electronic devices are equipped with one or even several wireless connections, and with some wireless standards, there is no more need for expensive infrastructure. IEEE 802.11 is an example of such a ubiquitous communication standard, connecting devices over short ranges at high data rates.

Radar has undergone a similar development, albeit somewhat delayed: Where several decades ago, radar was synonymous with either military technology or large-range civilian applications such as airspace or nautical surveillance, the miniaturization of mass-produced, high-frequency components has allowed radar to become a versatile tool for medium ranges (up to several hundred metres) or even short-range applications (very few metres, usually with sub-centimetre precision).

A major leader for development in these fields is the automotive industry. A modern vehicle may be equipped with multiple radar sensors to provide

driver assistance functionality. Also, the aspect of car-to-car or car-to-infrastructure communication has gained interest, making the vehicle another participant of wireless communication.

1.1 Background

Radar and communication have a lot in common: Both transmit and receive electromagnetic waves and use signal processing methods to extract information from the received signal. It is therefore not a far-fetched idea to combine these systems: The signal used to transmit information to others could also be used to image the surroundings and detect scatterers. Suggestions to this effect go back as far as the 1940s [76], yet it has not found wide-spread use (the exception being passive radar systems, which typically use broadcasting signals to perform radar measurements).

If anything, the potential utility of such combined systems has increased. Performing both functions at once saves hardware, which returns cost and allows for mass production. The spectrum is also used more efficiently, as radar and communications do not require separate bands.

In 2008, a joint research project between the Communications Engineering Lab (CEL) and the Institut für Hochfrequenztechnik und Elektronik (IHE) at the Karlsruhe Institute of Technology (KIT) was launched, initially funded by the Deutsche Forschungsgemeinschaft (DFG). Called “RadCom”, its aim was to investigate OFDM signals as the waveform for a communication/radar combination. The research presented here is partly a result of this project.

1.2 Outline

The development of OFDM radar is far from being the only new development in the field of short- and medium-range communication and radar systems. The automotive industry in particular has been very active developing and applying new technologies in this domain. To put this work into perspective, Chapter 2 will give an overview of current technologies, with a focus on vehicular and mobile ad hoc networks, medium-range radar systems and OFDM-based technologies.

All the fundamentals of OFDM and OFDM radar are covered in Chapter 3. Beginning with a very brief introduction to the OFDM technique, the problem of estimating range and Doppler of targets is applied to the case where the source of the scattered signal is an OFDM transmitter.

To solve the estimation problem, both non-parametric and parametric methods are considered. The main novelty of this research is a comprehensive analysis of OFDM radar, which includes aspects of signal processing, estimation theory and implementation issues.

For the majority of this chapter, the specifics of the OFDM signal parametrization are irrelevant. However, many aspects discussed in this chapter limit the choice of these parameters. Therefore, two possible parametrizations are described, which are then also used in the following chapters.

The transition from single nodes to OFDM radar networks is discussed in Chapter 4. OFDM radar systems only make sense if operated in networks, but this also means an increased level of interference, as it is unavoidable that multiple radar systems will attempt to perform radar imaging at the same time. Unlike other research on radar networks, which most often uses empirical models for the network geometry, a stochastic model for the distribution of the individual nodes was chosen. Also, a novel figure of merit for radar networks is introduced: *radar network outage* describes the event when individual nodes cannot detect a reference object due to the increased interference by other network participants. Due to the stochastic model, it is possible to calculate the outage probability analytically for certain cases, which is a useful tool for radar interference research.

While the vast majority of Chapters 3 and 4 is theoretical in nature, Chapter 5 provides some empirical research to confirm the previous results. A set of tools was developed to perform both simulations and live measurements, which is described here. Using software radio technology, it is possible to switch quickly between a simulated environment and a live setup. The rest of this chapter consists of measurements and simulation results. These are then compared to the theoretical results from the previous chapters. Finally, Chapter 6 lays out the conclusions reached.

2

Radar Sensing and Communication Networks

In the past, the most common configuration for wireless networks was focussed around a base station, which provides connectivity to a wired infrastructure. The most common examples are the mobile networks, which rely on standards such as GSM, UMTS or LTE, and wi-fi networks, which most often make use of the IEEE 802.11 family of standards. In all these systems, the end user (or mobile terminal) depends on a single point of access.¹

In some cases, there might be a need for devices to directly communicate with each other, thereby removing the requirement for any central infrastructure. There are several reasons to do so, such as the necessity to remove any delay caused by accessing the base station.

¹More precisely, the mobile terminal depends on a single base station at any given time; the actual base station may change.

Car-to-car (or vehicle-to-vehicle, V2V) communication is such a case. Here, vehicles are in direct contact with each other, which allows them to pass information about their traffic situation, broadcast potential dangers or coordinate maneuvers. As an example, a vehicle could announce an emergency brake to trailing vehicles in order to avoid a collision. Clearly, it is desirable to transmit this information with the smallest delay possible, which suggests a direct transmission between participating nodes rather than a detour via a base station.

Such networks are called *vehicular ad hoc networks* (VANETs) or, more generally, *mobile ad hoc networks* (MANETs). Compared to centrally coordinated wireless networks, VANETs introduce a multitude of new challenges. On the signal processing side, terminals have to cope with unreliable wireless links due to fast and frequency-selective fading channels, which may fluctuate rapidly. On the networks side, the network topology is random, and always changing. This makes VANETs a challenging topic of research.

The complexity of such vehicles is further increased when additional sensors, such as radar, are introduced. In particular, when communication and radar are combined, as discussed in the following two chapters, the signalling is subject to additional constraints.

However, before going into the details of OFDM radar, a short introduction to vehicular networks and radar systems shall be given.

2.1 Vehicular networks

The development of new technologies for the automotive sector is driven by new requirements for future vehicles. The desire for safer driving (in 2004, traffic-related injuries were identified as the single most lethal type of injury [80]), less fuel consumption and better driver's assistance all call for innovation in this new field, labelled intelligent transportation systems (ITS). This is not made easier by the fact that traffic density has been increasing ever since the inception of the automobile industry, in Germany alone there were more than 52 million registered vehicles in 2013 [79].

Car-to-car communication is one component of ITS [28, 29, 30]. Connectivity between cars makes driving a collaborative effort, rather than

every driver acting as a individual. Vehicles can transmit information about lane changes, emergency braking and other maneuvers. This can be used to alert and assist drivers of other vehicles. Another example for the application of car-to-car communication is a concept known as platooning, where vehicles run at close range. An excellent overview of car-to-car communication systems and their functions is given in [32].

The European Union in particular has been very active pursuing the development of car-to-car communication systems, and has launched several research programs in this field (see [28] for a full list). The Car-to-car Communication Consortium (C2C-CC) is a collaboration between industry and academia to create European standards for vehicular communication.

The IEEE 802.11p standard has globally become accepted as the standard for ad hoc, inter-vehicular communications [28]. It uses OFDM signals on its physical layer, which prompts the question as to whether it could be used for OFDM radar (this is discussed in the following chapter).

2.2 Radar Systems

Another major advancement in ITS technology are radar sensors. The first development on such sensors was started in the 1960s, and they have been commercially available since 1972 [51, 52].

A modern vehicle may have several radar sensors on board for several purposes; the most common being radars at the front for adaptive cruise control (ACC) and collision avoidance, at the side for blind spot detection and the rear for rear crash protection and lane change assistance [50].

Recent developments in the domain of vehicular radar show a clear trend towards FMCW radars operating in the 24 GHz and even more so in the 77 GHz bands [49, 51].

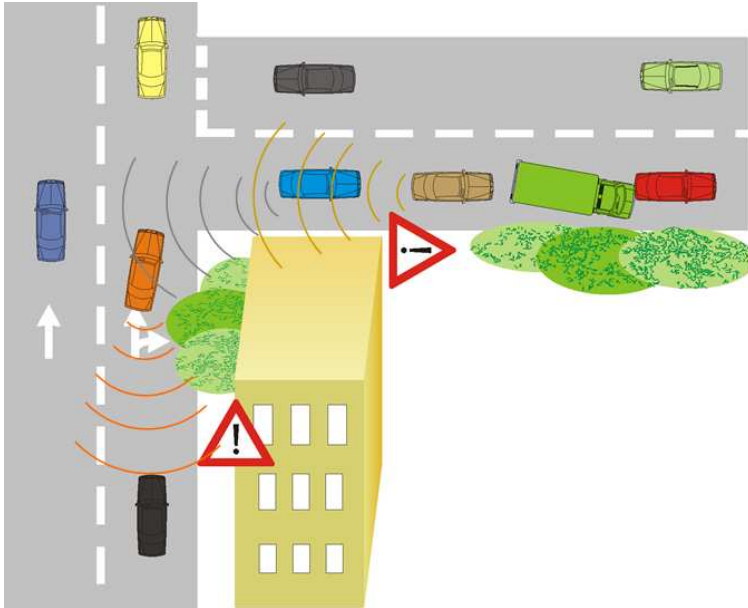


Figure 2.1: A traffic situation where ITS can be beneficial: Cars use their sensors to detect an accident and transmit this information to other vehicles which might not have line of sight to the danger.

2.2.1 Mutual interference in radar networks

With the possibility of integrating a radar system into every vehicle, radar systems are facing an entirely new challenge: Because they all operate in similar bands, in close proximity and possibly at the same time, they cause *mutual interference*. This topic has recently become a focus of research. The European Union has even made this a core research program [60], which is an indication of how relevant this topic has become.

Radar interference has been researched both analytically and empirically. Brooker [67] provides a very thorough analysis of interference in automotive radar systems at 77 and 94 GHz; his metric of choice is the probability of interference. Brooker argues that in case of interference, radar systems cease to work and interference-avoidance techniques must be introduced. As will be discussed in Chapter 4, this is not a suitable metric for OFDM radar systems (and possibly for any radar system where the interfering radar signals appear as additional white noise).

Goppelt et al. chose the probability of ghost target detection as a figure of merit [65, 66]. However, their results cannot be generalized to OFDM radar, as the derivations are specific to FMCW radar (despite being a commonly applied waveform, OFDM is rarely considered for radar networks). They also lack a random modelling of the interfering signal's attenuation. Similarly, the analysis of Oprisan et al. [69] is also very specific to certain waveforms.

In general, current research focuses on interference avoidance and mitigation techniques, which is exemplified by the results from the MOSARIM project, e.g. [61]. Here, OFDM is in fact considered as a method to cope with mutual interference, but further analysis is not given. One suggestion as to how to handle interference instead of avoiding it is given in [20], which is also the only publication which directly researches interference in OFDM radar networks. The paper suggests an interference mitigation technique, but only for the very specific scenario of one single interferer.

The difficulty of limiting the scope to a single interferer is also identified by Hischke [64]. He introduces a very useful quantity: The distribution of SINR as cause of mutual interference, as a function of the spacing

between vehicles, from a given geometry. However, his results are derived from simulations, emphasizing the need for an analytical solution.

The importance of simulations is underlined by the work of Zwick et al. [68], who have done considerable work in the research of mutual radar interference. Their approach is empirical in nature, and consists of elaborate software tools packaged under the name *Virtual Drive* [63]. The results generated are highly useful, but emphasize the fact that highly sophisticated simulations are the only means to research radar networks, motivating the derivation of analytical solutions.

In general, there has been little effort to create a “fundamental radar network theory”, analogous to what information theory is for communication networks. Hischke’s approach seems the most promising in this respect: If a probability distribution of the SINR could be derived for a given radar interferer density, this would allow a stochastic analysis of the interferer problem. More importantly, it would ground the research on radar networks with theoretical results and provide benchmarks for the empirical results – at this point, there is no theoretical bound for the performance of radar networks. This motivated the results in Chapter 4, which aims to be a first step towards a theoretical understanding of radars operating under mutual interference.

2.3 Combined Communication and Radar systems

The idea of combining communication and radar first came up during the developments triggered by the Second World War [76]. However, active development on combined systems is rare. One of the few examples of deployed combined systems was implemented in the NASA Space Shuttle “Orbiter” [77]. This system could switch between radar and communications functionality, but not perform both at the same time.

A software defined radio, where the entire signal processing can be modified, could be an ideal candidate for implementing such a combined radar and communication device. This was hinted on by Wiesbeck in 2001 [78].

This idea was first applied to vehicular applications in 1998 by Takeda et al. [23]. Here, a spread spectrum technique was employed.

The idea to use OFDM for this purpose was first suggested in 2000 by Levanon [46] and further researched in 2006 by Franken et al. [35] as well as by Donnet et al. [36]. Garmatyuk et al. were the first to fully describe how OFDM can be used to perform both radar and communications without degrading the performance of either subsystem, and presented both results for the quality of the radar imaging as well as the data link [39, 40, 41, 42, 44]. However, they did fail to describe the signal processing aspect correctly and identify potential optimizations. Sturm and Wiesbeck were the first to suggest a simple signal processing algorithm for OFDM radar, which is identified as a two-dimensional periodogram in Chapter 3, and present some simulations and measurement results to prove the applicability [19, 18].

Experimental proof of the suitability of OFDM for radar has been given in various setups by Falcone [38], Sturm [14] and Reichardt [45].

None of these publications address theoretical aspects of the signal processing methods. Questions of optimality or theoretical performance are never discussed, and the aspect of mutual interference and how it affects radar performance are also unclear. This work aims to close these gaps in the following two chapters.

3

OFDM Radar Algorithms

In this chapter, methods to obtain radar measurements from OFDM signals shall be discussed. For the entirety of this work, the focus will lie on OFDM radar algorithms based on spectral estimation, as it will be shown that these are well suited to include a communications subsystem. Other types of OFDM radar algorithms have been proposed and will briefly be discussed in Section 3.5.

The following sections will explain how the spectral estimation-based algorithms work. First, a brief introduction to OFDM signals is given. From there, the effects of the radar propagation channel on OFDM signals are derived in a manner that results in the spectral estimation based algorithms.

3.1 Physical structure of an OFDM signal

Before discussing the details of OFDM radar, this section will briefly recapitulate the parameters relevant for an OFDM signal. This is not

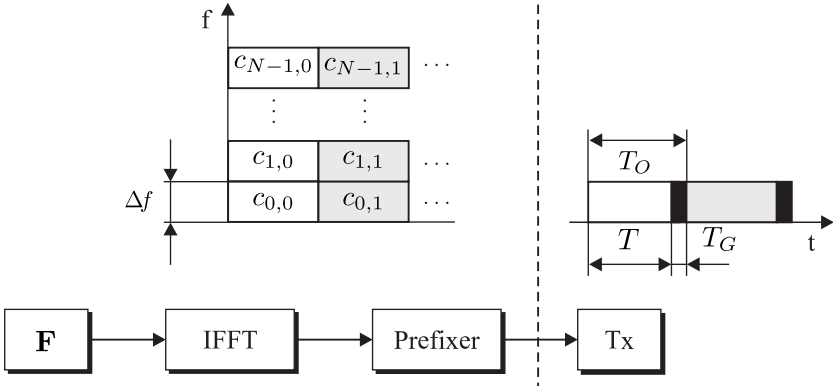


Figure 3.1: Schematic of an OFDM frame

meant as an introduction to OFDM; a more complete description of an OFDM system can be found in most introductory textbooks on digital communications, such as [94] or [99].

As the name indicates, OFDM is a frequency multiplexing scheme which transmits data on several orthogonal frequencies in parallel. Compared to a single-carrier scheme with identical data rate, OFDM thus has a lower symbol rate, but transmits several symbols at once.

Fig. 3.1 illustrates how an OFDM signal distributes information in the time-frequency plane. First, complex symbols $c_{k,l} \in \mathcal{A}$ are chosen from a modulation alphabet $\mathcal{A} \subset \mathbb{C}$. Suitable choices of \mathcal{A} for practical application in car-to-car scenarios are BPSK ($\mathcal{A} = \{\pm 1\}$) and QPSK alphabets ($\mathcal{A} = \{\pm\sqrt{2} \pm \sqrt{2}j\}$); however, for the following derivations \mathcal{A} could be any alphabet, including higher PSK and QAM schemes.

Sub-carriers and OFDM symbols The OFDM signal utilizes N carriers, with frequencies f_0 through f_{N-1} , respectively. In complex baseband, $f_{\lceil N/2 \rceil}$ is at DC. Once the entire signal is shifted to the pass band, the centre carrier's frequency shall be defined as the *centre frequency* f_C . For the radar application, it is assumed that the OFDM signal has a limited length of M time slots. This is true in any case if the connected communication system is packet-based, but is also applicable

for continuously broadcasting transmitters which can be interpreted as transmitting many time-limited signals one after another.

A set of modulation symbols transmitted in the same time slot is called an *OFDM symbol*. The entirety of $N \times M$ transmitted symbols is called a *frame*.

Carrier and symbol orthogonality The orthogonality of the frequency division is achieved by choosing a constant sub-carrier distance $\Delta f := f_{k+1} - f_k$ of the inverse OFDM symbol duration,

$$\Delta f = \frac{1}{T}. \quad (3.1)$$

Assuming a rectangular pulse shape of duration T for the modulation symbols $c_{k,l}$, this choice is easily explained with such a pulse's Fourier transform

$$\text{rect}_T(t) = \begin{cases} 1 & \text{for } |t| \leq \frac{T}{2} \\ 0 & \text{for otherwise} \end{cases} \quad \circ \bullet T \frac{\sin(\pi f T)}{\pi f T}, \quad (3.2)$$

which has its first zero crossing at a distance of $1/T$ from its peak. The sub-carriers' frequencies can thus be represented as a function of the sub-carrier index k ,

$$f_k = f_0 + k\Delta f, \quad (3.3)$$

and the carrier for the symbol $c_{k,l}$ may be written as

$$s_{k,l}(t) = \text{rect}_T(t - lT_O) e^{j2\pi k \Delta f t}. \quad (3.4)$$

The orthogonality condition now holds in time and frequency,

$$\int_{-\infty}^{\infty} s_{k_1, l_1}(t) s_{k_2, l_2}^*(t) dt = \begin{cases} \text{const} & \text{for } k_1 = k_2 \text{ and } l_1 = l_2 \\ 0 & \text{for otherwise.} \end{cases} \quad (3.5)$$

To prove this, first assume that $l_1 \neq l_2$. Then, the product $\text{rect}_T(t - l_1 T_O) \cdot \text{rect}_T(t - l_2 T_O)$ is always zero (as the two rect -functions do not share any support), and so is (3.5). Next, assume $l_1 = l_2$ but $k_1 \neq k_2$

and solve (3.5):

$$\begin{aligned} \int_{-\infty}^{\infty} s_{k_1, l_1}(t) s_{k_2, l_1}^*(t) dt &= \int_0^T e^{j2\pi(k_1 - k_2)\Delta f t} dt \\ &= \frac{1}{2\pi(k_1 - k_2)\Delta f} \left[e^{j2\pi(k_1 - k_2)\Delta f t} \right]_0^T \\ &\stackrel{(\Delta f T = 1)}{=} 0. \end{aligned} \quad (3.6)$$

Only for $k_1 = k_2$ and $l_1 = l_2$, (3.6) becomes

$$\int_0^T e^{j2\pi(k_1 - k_2)\Delta f t} dt = \int_0^T 1 dt = T. \quad (3.7)$$

This leaves the question on how to choose Δf (or T), which is discussed in greater depth in Section 3.6.

Cyclic Prefix In a final step, a *guard interval* is inserted before every OFDM symbol. It is of duration T_G , which is chosen as an integer fraction of the symbol duration. Typical values are $T_G/T = 1/4$ or $T_G/T = 1/8$; choosing a valid guard interval duration is discussed in Section 3.6. Of course, this increases the total OFDM symbol duration to $T_O = T + T_G$.

Without a guard interval, a time-dispersive (i.e. frequency-selective) channel would leak energy from one OFDM symbol into the next, causing *inter-symbol interference* (ISI). A guard interval therefore prevents the loss of orthogonality between adjacent OFDM symbols. The most common way to create a guard time is to prepend a cyclic prefix (CP), which is a copy of the last T_G/T -th part of the OFDM symbol (see [94] for more details on cyclic prefixes and why they are used). For the rest of this work, the usage of a CP is assumed.

Sampling rate and IFFT length These two parameters are relevant for the implementation and specify the bandwidth of the OFDM signal. It is well-known that the modulation of an OFDM signal can efficiently be performed using an inverse fast Fourier transform (IFFT). Consider a discrete-time representation of the sum of modulation symbols on the 0-th OFDM symbol, multiplied by their carriers, sampled at time intervals

T_S :

$$\begin{aligned} s(nT_S) &= \sum_{k=0}^{N-1} c_{k,0} \text{rect}_T(nT_S) e^{j2\pi k \Delta f n T_S} \\ &= \sum_{k=0}^{N-1} c_{k,0} e^{j2\pi k \Delta f n T_S}. \end{aligned} \quad (3.8)$$

By setting the sampling time to

$$T_S = \frac{T}{N} = \frac{1}{\Delta f N}, \quad (3.9)$$

(3.8) becomes

$$s(nT_S) = \sum_{k=0}^{N-1} c_{k,0} e^{j2\pi \frac{n k}{N}}, \quad (3.10)$$

which shows that the discrete-time signal for an OFDM symbol is the result of an IFFT of the modulation symbols and the sampling rate for the modulator $f_S = 1/T_S$ is fixed to $f_S = N \cdot \Delta f$.

Sub-carrier allocation This leaves one open parameter: the sub-carrier selection. As the previous paragraph indicates, the OFDM sub-carriers occupy the entire Nyquist zone. For the digital/analog conversion step, it is advisable to not occupy the entire Nyquist bandwidth, which can be achieved by setting the modulation symbols closest to $\pm f_S/2$ to zero. The same is also true for the DC carrier, which is usually set to zero as well.

By extending this notion of disabling individual sub-carriers, a whole new degree of freedom becomes available. Assume the total number of available sub-carriers (i.e. the IFFT-length) is N_{Total} . From these, any $N \leq N_{\text{total}}$ carriers can be activated for transmission. This could be a consecutive range of carriers in the middle of the Nyquist bandwidth, or even a completely random subset of carriers. Different sub-carrier allocations are discussed in Section 3.3.8.

Fig. 3.2 shows a schematic of an OFDM transmitter and illustrates where all the individual parameters have an effect. A list of all relevant parameters is shown in Table 3.1.

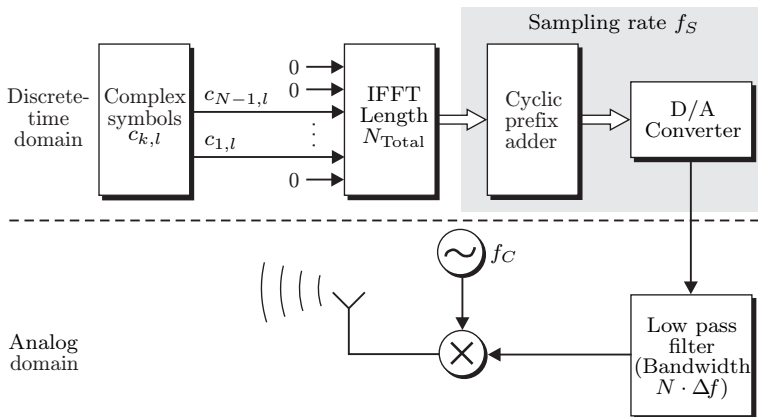


Figure 3.2: Block diagram of an OFDM transmitter

3.1.1 PAPR

For OFDM systems in particular, the peak-to-average power ratio (PAPR) is an important metric. It is defined as

$$\text{PAPR} = \frac{\max[|s(t)|^2]}{\text{mean}[|s(t)|^2]}, \quad (3.11)$$

i.e. as the peak power divided by the mean power of the signal.

In OFDM, PAPR can be very high when compared to other modulation schemes. Assume $s(t)$ describes a single OFDM symbol with unit mean power. In this case, PAPR can be as high as the number of sub-carriers N , which happens when all sub-carriers transmit the same symbol.

Practical OFDM systems scramble the information to be transmitted, which causes the transmit data to appear pseudo-random. In this case, it has been shown that PAPR rarely exceeds a value of $2 \ln N$ [33].

For more details on PAPR in OFDM, cf. [94, Chap. 6] and [99, Chap. 16].

Symbol	Parameter
\mathcal{A}	Modulation alphabet
N	Number of sub-carriers
M	Number of OFDM symbols
Δf	Sub-carrier spacing
$T = 1/\Delta f$	OFDM symbol duration
T_G	Duration of cyclic prefix
$T_O = T + T_G$	Total duration of OFDM symbol
$N_{\text{Total}} \geq N$	IFFT length
$f_S = N_{\text{Total}}\Delta f$	Sampling rate
n/a	Sub-carrier allocation

Table 3.1: Parameters in an OFDM transmitter

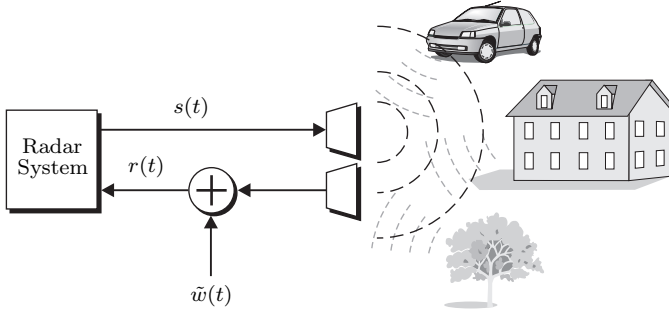


Figure 3.3: Schematic of a radar system

3.2 The OFDM radar estimation problem

Before developing algorithms to perform radar imaging,¹ it is essential to understand how OFDM signals are affected by the radar operation. Fig. 3.3 shows a very basic schematic of a monostatic radar system: To obtain an image, it transmits a signal $s(t)$. At the exact same time, it receives a signal $r(t)$ which consists of a superposition of reflections of the original signal by objects positioned in the way of $s(t)$'s wave front, as well as receiver noise. Generally speaking, a radar system analyzes the received signal to determine range and relative velocity of the objects.

In practice, the direction from which the target backscatters energy towards the radar system is also important. However, this is not discussed in this chapter, because the detection of the angle is not specific to OFDM radar, and any established technique such as digital beamforming or MUSIC [88] can be used, whereas the detection of range and relative velocity is. For this chapter, it is therefore assumed that there is only one receive antenna, and that the radar is not attempting to estimate the direction of arrival of the backscattered signal.

Assuming a total of H reflecting objects, the received signal has the form

$$r(t) = \sum_{h=0}^{H-1} b_h s(t - \tau_h) e^{j2\pi f_D, h t} e^{j\tilde{\varphi}_h} + \tilde{z}(t). \quad (3.12)$$

This includes the following effects:

- First, the magnitude of every signal reflection is attenuated by a factor b_h . This factor depends on the distance of the target d_h and its radar cross section (RCS) $\sigma_{\text{RCS}, h}$. Applying the point scatter model, the attenuation is

$$b_h = \sqrt{\frac{c_0 \sigma_{\text{RCS}, h}}{(4\pi)^3 d_h^4 f_C^2}}, \quad (3.13)$$

where c_0 is the speed of light.

¹*Radar imaging* describes the process of obtaining an estimate of the surroundings from the backscattered signal.

- The signal is delayed by the time it takes for it to travel to the object and back,

$$\tau_h = 2 \frac{d_h}{c_0}. \quad (3.14)$$

- A relative velocity $v_{\text{rel},h}$ of the object will cause a Doppler shift of the signal by

$$f_{D,h} = 2 \frac{v_{\text{rel},h}}{c_0} f_C. \quad (3.15)$$

- Also, the signal is rotated by an additional random phase $\tilde{\varphi}_h$.
- Finally, it is overlaid with white Gaussian noise $\tilde{z}(t)$.

To apply (3.12) to OFDM signals specifically, a new notation is introduced. A transmitted OFDM frame is represented by a matrix

$$\mathbf{F}_{\text{Tx}} = \begin{pmatrix} c_{0,0} & \cdots & c_{0,M-1} \\ c_{1,0} & \cdots & c_{1,M-1} \\ \vdots & \ddots & \vdots \\ c_{N-1,0} & \cdots & c_{N-1,M-1} \end{pmatrix} \in \mathcal{A}^{N \times M}. \quad (3.16)$$

Each row of \mathbf{F}_{Tx} represents a sub-carrier; each column represents an OFDM symbol of the transmitted frame. If sub-carriers are left empty (such as the DC carrier), the corresponding elements $c_{k,l}$ are set to zero, although empty sub-carriers at the edge may be discarded (therefore, the matrix has N rows even if $N < N_{\text{Total}}$).

In combination with the knowledge of the parameters given in Table 3.1, this matrix is all that is necessary to describe the time domain signal. By traversing the transmitter in reverse order, converting the received signal $r(t)$ to a *received frame matrix* \mathbf{F}_{Rx} is straightforward, i.e. by

- analog/digital conversion of the signal,
- removing the CP and
- calculating an FFT of length N_{Total} for every column of the matrix.

The next step is to derive how a received matrix \mathbf{F}_{Rx} looks given a transmit matrix and a set of H reflecting objects.

To simplify this, assume that $H = 1$ and analyze the effects individually. First, the Doppler shift is studied. It is useful to think of every row of

\mathbf{F}_{Tx} as an individual discrete-time signal sampled at intervals of length T_O . A frequency shift by f_D is therefore simply a modulation of every row of \mathbf{F}_{Tx} with a discretely sampled complex sinusoid $e^{j2\pi f_D T_O l}$, $l = 0 \dots M - 1$.

The delay causes a phase shift of the individual elements $c_{k,l}$. The phase shift value is different for every sub-carrier, depending on its frequency. For a delay τ , the phase shift on the k -th sub-carrier is thus $e^{-j2\pi(k\Delta f + f_0)\tau}$.

By combining these effects, \mathbf{F}_{Rx} for $H = 1$ becomes

$$(\mathbf{F}_{\text{Rx}})_{k,l} = b_0(\mathbf{F}_{\text{Tx}})_{k,l} \cdot e^{j2\pi T_O f_{D,0} l} e^{-j2\pi\tau_0(k\Delta f + f_0)} e^{j\tilde{\varphi}_0} + (\tilde{\mathbf{Z}})_{k,l}. \quad (3.17)$$

$\tilde{\mathbf{Z}} \in \mathbb{C}^{N \times M}$ is the matrix representation of the AWGN. Its elements are i.i.d. complex random variables from a circular, zero-mean Gaussian distribution with variance σ^2 . As f_0 and $\tilde{\varphi}_0$ are constant, define $\varphi_h := \tilde{\varphi}_h - 2\pi f_0 \tau_h$ and thus simplify (3.17) to

$$(\mathbf{F}_{\text{Rx}})_{k,l} = b_0(\mathbf{F}_{\text{Tx}})_{k,l} \cdot e^{j2\pi T_O f_{D,0} l} \cdot e^{-j2\pi\tau_0 \Delta f k} \cdot e^{j\varphi_0} + (\tilde{\mathbf{Z}})_{k,l}. \quad (3.18)$$

\mathbf{F}_{Rx} now contains the parameters τ and f_D which are to be estimated, the nuisance parameters φ and b , as well as \mathbf{F}_{Tx} . The latter serves no purpose for the estimation problem. It is therefore removed from the equation by element-wise division,

$$(\mathbf{F})_{k,l} = \frac{(\mathbf{F}_{\text{Rx}})_{k,l}}{(\mathbf{F}_{\text{Tx}})_{k,l}} = b_0 \cdot e^{j2\pi l T_O f_{D,0}} \cdot e^{-j2\pi k \tau_0 \Delta f} \cdot e^{j\varphi_0} + \frac{(\tilde{\mathbf{Z}})_{k,l}}{(\mathbf{F}_{\text{Tx}})_{k,l}}. \quad (3.19)$$

Again, matters can be simplified by defining an alternative noise matrix $(\mathbf{Z})_{k,l} = (\tilde{\mathbf{Z}})_{k,l} / (\mathbf{F}_{\text{Tx}})_{k,l}$, which removes the influence of the transmitted data from the model. How \mathbf{Z} and $\tilde{\mathbf{Z}}$ are connected depends on the modulation alphabet utilized; for constant-amplitude modulation alphabets, such as all PSK variations, they have the same statistical properties. For other alphabets, such as 16-QAM, a more detailed analysis is presented in Appendix A. In any case, \mathbf{Z} is still a white noise process if $\tilde{\mathbf{Z}}$ is white.

Using \mathbf{Z} , \mathbf{F} results in

$$(\mathbf{F})_{k,l} = b_0 e^{j2\pi l T_O f_{D,0}} e^{-j2\pi k \tau_0 \Delta f} e^{j\varphi_0} + (\mathbf{Z})_{k,l}. \quad (3.20)$$

Next, this result is generalised to H targets. Since both operations used to calculate \mathbf{F}_{Rx} from $r(t)$ (FFT and removal of the CP) are linear w.r.t. their input signal, the sum from (3.12) can be reintroduced, yielding

$$(\mathbf{F})_{k,l} = \sum_{h=0}^{H-1} b_h e^{j2\pi l T_O f_{D,h}} e^{-j2\pi k \tau_h \Delta f} e^{j\varphi_h} + (\mathbf{Z})_{k,l}. \quad (3.21)$$

This last form clearly shows what the estimation problem looks like for the case of OFDM radar: The estimation of the round trip delay and the Doppler shift (and, accordingly, the targets' distance and relative velocity) is transformed into a spectral estimation problem; more precisely: the estimation of the *frequencies of a superposition of discretely sampled complex sinusoids*, as well as the number of such sinusoids. For the one-dimensional case, this is a thoroughly researched field, and many algorithms exist which can be made use of.

Another advantage results from the fact that Doppler and delay estimations are completely independent. They do not influence each other as is the case e.g. with FMCW radar systems and can be estimated independently from each other.

From (3.21), a generic target estimation problem can be formulated:

1. Estimate the number of targets.
2. For every target, estimate the respective sinusoids' frequencies $\hat{\Omega}_d$ (column-wise) and $\hat{\Omega}_r$ (row-wise).
3. Translate these frequencies into distance and relative velocity by

$$\hat{d} = \frac{1}{2} \hat{\tau} c_0 = \frac{\hat{\Omega}_d c_0}{2(2\pi)\Delta f}, \quad (3.22)$$

and

$$\hat{v} = \frac{\hat{f}_D c_0}{2f_C} = \frac{\hat{\Omega}_v c_0}{2(2\pi)f_C T_O}. \quad (3.23)$$

4. For every target, obtain an estimate \hat{b}_h for the attenuation of the sinusoids. Use this for an estimate of the radar cross section by inverting (3.13),

$$\hat{\sigma}_{\text{RCS},h} = \frac{1}{c_0} \hat{b}_h (4\pi)^3 \hat{d}_h^4 f_C^2. \quad (3.24)$$

At this point, it is worth mentioning that the calculation of \mathbf{F} from the input signal is very simple: it merely consists of the CP removal, a total of M FFTs of length N_{Total} (these operations demodulate the OFDM signal and produce \mathbf{F}_{Rx}) and the division of the transmit symbols. For BPSK and QPSK alphabets, the latter operation is as simple as changing a sample's sign or swapping registers. All these operations can be calculated very quickly and efficiently on signal processing components such as FPGAs.

3.2.1 Accuracy of the sinusoidal model

This derivation of the problem statement – and therefore the validity of the signal model (3.21) – implies five assumptions, which are listed in the following.

- (A1) No other distortion other than AWGN is induced by the transmit and receive front-ends.

This assumption is an idealisation which eliminates all hardware-related issues from the analysis, including the *entire* signal processing chain. Direct coupling into the receive antenna is not necessarily a problem, as it will appear as a very strong and close target, although it will restrict the dynamic range of the radar system.

- (A2) The CP duration is larger than the round-trip propagation time for the furthest target.
- (A3) The sub-carrier distance is at least one order of magnitude larger than the largest occurring Doppler shift.

These assumptions can easily be met by choosing the signal parameters appropriately, which is discussed in greater detail in Section 3.6. The only problem here is the choice of the maximum values for distance and Doppler shift. However, these can often be deduced from the application. For instance, in car-to-car communication networks radar systems rarely need to cope with distances larger than a few hundred metres, and relative velocities usually stay well under 150 m/s. None of these values pose serious restrictions to the signal design.

- (A2) and (A3) guarantee no de-orthogonalisation will occur in the received matrix. Simply put, it ensures the element-wise division in (3.20)

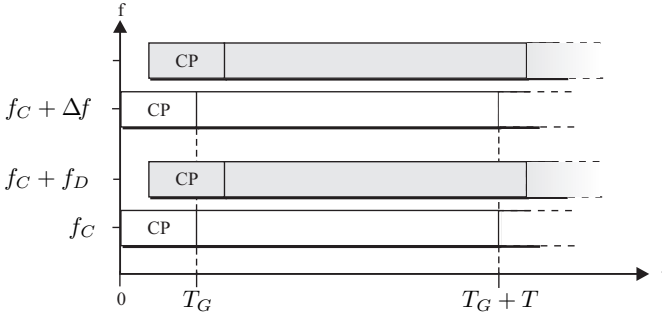


Figure 3.4: If the received signal (indicated as gray boxes) is delayed for more than the CP, or if it is shifted by a large Doppler shift, modulation symbols are aligned incorrectly and de-orthogonalization occurs.

divides the correct elements $c_{k,l}$. Fig. 3.4 illustrates this: as long as these assumptions are met, the OFDM symbols are not shifted too far from their original position and can correctly be demodulated.

It must be noted that while maintaining orthogonality in time is trivial, perfect orthogonality in frequency can never be achieved when there is a non-zero Doppler shift. By choosing an appropriate sub-carrier spacing, this error can be minimized at least for small values of f_D .

- (A4) The Doppler shift is the same on every sub-carrier.
- (A5) The target's distance remains constant during the transmission of one frame.

These last assumptions are never exactly true for non-zero Doppler shifts, but they simplify the design of the algorithm immensely as they imply that the sinusoids have identical frequencies on all the rows and columns, respectively. Besides, they are by no means crude approximations: (A4) is a fair assumption if the centre frequency is much larger than the total bandwidth. (A5) is also reasonable as OFDM frame durations are usually on the order of milliseconds. Even fast objects will not move a distance larger than the available range resolution in this time.

3.2.2 Unambiguous ranges

The discrete nature of \mathbf{F} implies that the estimation result is only non-ambiguous if $|T_O f_D| < 1/2$ and $\tau \Delta f < 1$ are always true. The maximum unambiguous range is therefore

$$d_{\text{unamb}} = \frac{c_0 \tau_{\text{unamb}}}{2} = \frac{c_0}{2\Delta f}, \quad (3.25)$$

and the maximum unambiguous velocity is

$$v_{\text{unamb}} = \frac{f_{D,\text{unamb}} c_0}{2f_C} = \frac{c_0}{2f_C \cdot T_O}. \quad (3.26)$$

As long as the true distances stay within $d < d_{\text{unamb}}$ and the true relative velocity stays within $|v| < v_{\text{unamb}}$, there will be no ambiguity due to aliasing. However, two targets at distances d and $d + d_{\text{unamb}}$ cannot be distinguished. If the parameters are chosen well, this is not a problem because either the unambiguous range is large enough to encompass all targets, or the scattered energy from targets beyond d_{unamb} received is too small to be detected.

3.3 Periodogram-based estimation algorithms

For the (one-dimensional) case of identifying sinusoids in a discrete-time signal, the periodogram is a well-understood tool and is in fact the optimal solution if the sinusoids are well resolved (i.e. they do not lie too closely together) [85, Chap. 13]. Given a discrete-time signal $s(k)$ of length N samples, the periodogram is defined as

$$\text{Per}_{s(k)}(f) = \frac{1}{N} \left| \sum_{k=0}^{N-1} s(k) e^{-j2\pi f k} \right|^2. \quad (3.27)$$

The common way to calculate this in digital systems is to quantize the frequency in regular intervals and use the Fast Fourier Transformation

(FFT),

$$\text{Per}_{s(k)}(n) = \frac{1}{N} \left| \sum_{k=0}^{N-1} s(k) e^{-j2\pi \frac{nk}{N_{\text{Per}}}} \right|^2 \quad (3.28)$$

$$= \frac{1}{N} |\text{FFT}_{N_{\text{Per}}} [s(k)]|^2, \quad (3.29)$$

where the notation $\text{FFT}_{N_{\text{Per}}} [s(k)]$ is used to denote an FFT of length N_{Per} on the input vector $s(k)$. Note that N_{Per} does not have to be equal to N . If $N_{\text{Per}} > N$, zero-padding is used to increase the length of $s(k)$ to N_{Per} . This increases the number of supporting points of the discrete periodogram and hence the accuracy at which frequencies can be estimated.

Since OFDM radar algorithms are sinusoidal identification algorithms (see Section 3.2), the periodogram can be applied here with some modifications, which was first proposed by Sturm et al. in [13, 12, 15] and is fully described in [18].

The input data for the periodogram is the matrix \mathbf{F} . Since this is a two-dimensional object, the periodogram has to be extended to two dimensions. The proposed solution is [18, 4]

$$\text{Per}_{\mathbf{F}}(n, m) = \frac{1}{NM} \left| \underbrace{\sum_{k=0}^{N_{\text{Per}}-1} \left(\sum_{l=0}^{M_{\text{Per}}-1} (\mathbf{F})_{k,l} e^{-j2\pi \frac{lm}{M_{\text{Per}}}} \right) e^{j2\pi \frac{kn}{N_{\text{Per}}}}}_{N_{\text{Per}} \text{ IFFTs of length } N_{\text{Per}}} \right|^2 \quad (3.30)$$

$$= \frac{1}{NM} |\text{CPer}_{\mathbf{F}}(n, m)|^2. \quad (3.31)$$

The result of the sums inside the modulus operator is called *complex periodogram* (CPer) in the following.

Sinusoids in \mathbf{F} will result in a peak in $\text{Per}_{\mathbf{F}}(n, m)$. Periodogram-based algorithms therefore must first detect these peaks. Then, if $\text{Per}_{\mathbf{F}}(\hat{n}, \hat{m})$ corresponds to a peak value, \mathbf{F} has a column-wise oscillation of frequency $\hat{\Omega}_d = 2\pi\hat{n}/N_{\text{Per}}$ and a row-wise oscillation of frequency $\hat{\Omega}_v = 2\pi\hat{m}/M_{\text{Per}}$. By applying (3.22) and (3.23), this corresponds to a target estimate of

$$\hat{d} = \frac{\hat{n}c_0}{2\Delta f N_{\text{Per}}} \quad \text{and} \quad \hat{v} = \frac{\hat{m}c_0}{2f_c T_O M_{\text{Per}}}. \quad (3.32)$$

To further adapt this periodogram to the radar case, the indices n and m are chosen such that

$$n = 0, \dots, N_{\text{Per}} - 1 \quad \text{and} \quad m = \lfloor \frac{-M_{\text{Per}}}{2} \rfloor, \dots, \lfloor \frac{-M_{\text{Per}}}{2} \rfloor - 1. \quad (3.33)$$

This allows for negative Doppler shifts (which correspond to targets moving away from the sensor) but not for negative distances, which have no physical meaning. Any periodogram-based estimate must therefore automatically lie within the intervals $0 \leq \hat{d} \leq d_{\text{max}}$ and $-v_{\text{rel,max}} \leq \hat{v} \leq v_{\text{rel,max}}$ introduced in Section 3.2.2.

The target's RCS can also be estimated from the periodogram if the point-scatter model (3.13) is used for the signal attenuation. Since the received power of the backscattered signal depends on the RCS, the amplitude of the periodogram at a peak location can directly be translated into an estimate of the RCS by

$$\hat{\sigma}_{\text{RCS}} = c_{\text{norm}} \frac{\text{Per}_{\mathbf{F}}(\hat{n}, \hat{m})}{P_{\text{Tx}} \cdot NM} \frac{(4\pi)^3 f_c^2 \hat{d}^4}{Gc_0^2}, \quad (3.34)$$

where c_{norm} is a hardware-dependant normalization factor (simulations were configured such that $c_{\text{norm}} = 1$, but for measurements this value must be calibrated).

Fig. 3.5 shows an example of a periodogram. The axes have already been converted from bin indices to range and Doppler values. The colour of the periodogram bins corresponds to the power received from the target including the processing gain from the periodogram, as will be discussed in the next section.

To improve readability, the power axis is omitted in some cases. Whenever this is the case, the normalization is chosen identically to that in Fig. 3.5.

Fig. 3.6 shows a block diagram of an entire OFDM radar system. The individual components will be discussed in the following sections.

3.3.1 Signal-to-noise ratio and processing gain

Before going into a detailed analysis of the periodogram, the signal-to-noise ratio (SNR) must be defined. Assume a target is present which

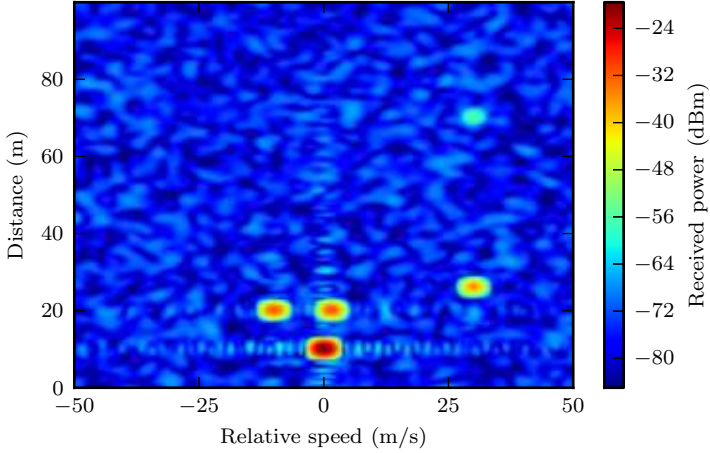


Figure 3.5: Example of a periodogram caused by five objects and WGN

backscatters a signal with power P_{Rx} . The relevant SNR is that just before the signal processing, in the matrix \mathbf{F}_{Rx} , which is given by

$$\text{SNR}_{\mathbf{F}_{\text{Rx}}} = \frac{P_{\text{Rx}}}{\underbrace{k_B \vartheta \cdot \text{NF}}_{\text{Noise power density}} \cdot N \Delta f}. \quad (3.35)$$

The noise power density consists of the Boltzmann constant k_B , the temperature ϑ and the noise figure NF, which incorporates the noise from all the components of the receiver chain, including the ADC. By multiplying this with the actual occupied bandwidth ($N \Delta f$), this becomes the total noise power.

Note that the division with \mathbf{F}_{Tx} in (3.21) does not change the SNR, as it scales noise and received power alike. The \mathbf{F} -matrix thus has the same SNR as the matrix \mathbf{F}_{Rx} ,

$$\text{SNR}_{\mathbf{F}} = \text{SNR}_{\mathbf{F}_{\text{Rx}}}. \quad (3.36)$$

However, the target detection is performed on the periodogram, not on \mathbf{F} . Its signal-to-noise ratio, SNR_{Per} is therefore defined for the bin

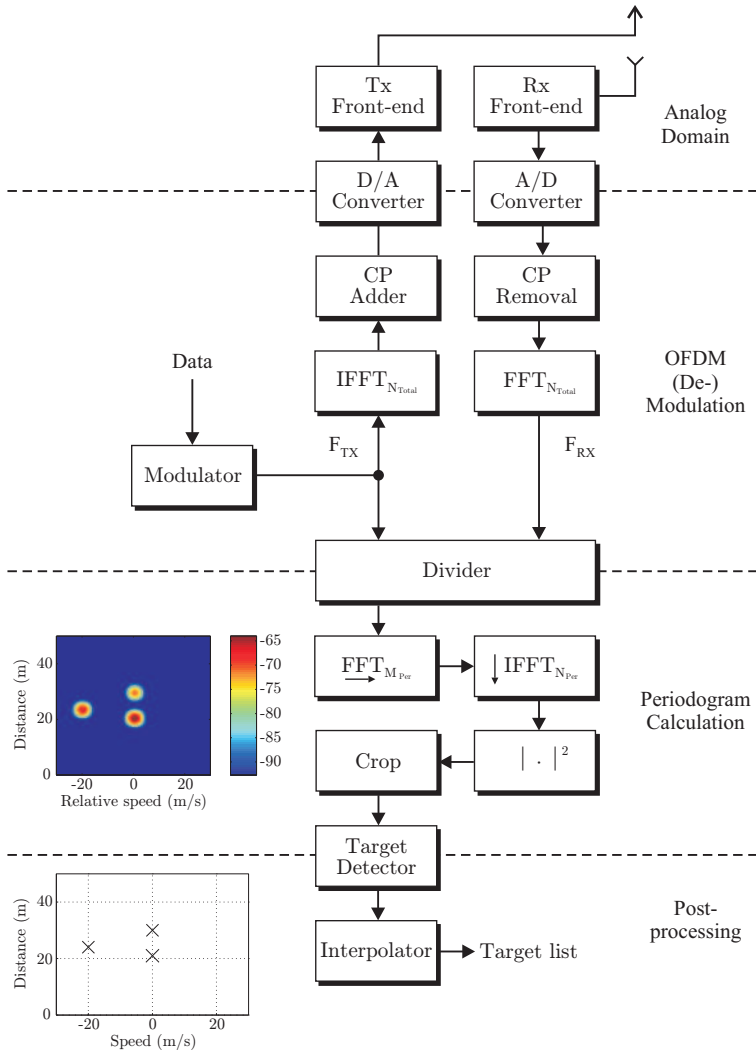


Figure 3.6: Block diagram of a periodogram-based OFDM radar system

containing the target's corresponding peak only. Intuitively, it makes sense that an optimal estimator would accumulate the received energy from all elements of \mathbf{F} into one bin of the periodogram, thereby increasing the SNR by factor NM . On a logarithmic scale, this results in

$$\text{SNR}_{\text{Per}} = \text{SNR}_{\mathbf{F}} + \text{PG}, \quad (3.37)$$

where $\text{PG} = 10 \log_{10}(NM)$ is the *processing gain*² due to the periodogram.

To show this is true, consider \mathbf{F} for $H = 1$ as in (3.20). First, the delay and Doppler shift are expressed by m and n ,

$$(\mathbf{F})_{k,l} = b_0 e^{j2\pi l \frac{m}{M_{\text{Per}}}} e^{-j2\pi k \frac{n}{N_{\text{Per}}}} e^{j\varphi_0} + (\mathbf{Z})_{k,l}. \quad (3.38)$$

The signal-to-noise ratio for (3.38) is

$$\text{SNR}_{\mathbf{F}} = \frac{b_0^2}{\text{E}[|(\mathbf{Z})_{k,l}|^2]}. \quad (3.39)$$

The SNR of the periodogram is, by the definition given above, the power of the signal in bin with index (n, m) divided by the noise power in that bin (note that, due to the whiteness of the noise power, the noise power is identical in all the bins):

$$\begin{aligned} \text{SNR}_{\text{Per}} = & \\ & \frac{\left| \sum_{k=0}^{N_{\text{Per}}-1} \left(\sum_{l=0}^{M_{\text{Per}}-1} b_0 e^{j2\pi l \frac{m}{M_{\text{Per}}}} e^{-j2\pi k \frac{n}{N_{\text{Per}}}} e^{j\varphi_0} e^{-j2\pi \frac{lm}{M_{\text{Per}}}} \right) e^{j2\pi \frac{kn}{N_{\text{Per}}}} \right|^2}{\text{E} \left[\left| \left(\sum_{l=0}^{M_{\text{Per}}-1} \mathbf{Z}_{k,l} e^{-j2\pi \frac{lm}{M_{\text{Per}}}} \right) e^{j2\pi \frac{kn}{N_{\text{Per}}}} \right|^2 \right]} \end{aligned} \quad (3.40)$$

$$= \frac{b_0^2 (NM)^2}{NM \cdot \text{E}[|(\mathbf{Z})_{k,l}|^2]} = NM \cdot \text{SNR}_{\mathbf{F}}. \quad (3.41)$$

As can be seen, the SNR is indeed increased by a factor NM . The numerator is a coherent accumulation of all the elements in \mathbf{F} , whereas the denominator is a superposition of complex Gaussian random variables.

It is important to realise that this definition of SNR_{Per} is only meaningful on a per-target basis. If several targets are present, more energy is backscattered towards the receiver—however, unless the targets are very close, this does not affect the SNR in one individual bin of the periodogram.

²In [98, Chap. 15], the general term chosen for this is *integration gain*.

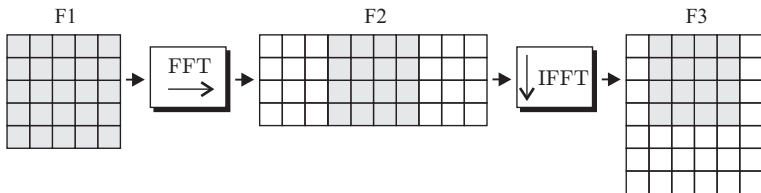


Figure 3.7: Calculation of the periodogram from \mathbf{F} . The grey area indicates periodogram elements within $n < N_{\max}$ and $|m| < M_{\max}$

3.3.2 Efficient calculation of the periodogram

As indicated in (3.30), $\text{Per}_{\mathbf{F}}(n, m)$ can be calculated from \mathbf{F} by means of FFTs and IFFTs. Fig. 3.7 illustrates how this is done: first, every row of \mathbf{F} is processed with an FFT. From the results of these FFTs, a new matrix is created which has M_{Per} columns if zero-padding is used for the FFTs. This new matrix is then further processed by calculating the IFFT of every column. Again, zero-padding will increase the number of rows to N_{Per} . Finally, the complex values resulting from the IFFT must be turned into their magnitude-squared.

Upon further inspection, it turns out that not all $N_{\text{Per}} \times M_{\text{Per}}$ elements of the periodogram correspond to useful values. As an example, assume that there is a peak at row index $\hat{n} = N_{\text{Per}} - 1$. This would correspond to a round-trip propagation time of $\tau = \frac{N_{\text{Per}} - 1}{N_{\text{Per}}} T$. Unless the guard interval T_G equals the OFDM symbol duration ($T = T_G$), this contradicts assumption (A2) (cf. Section 3.2.1)! Analogously, a peak at column index $\hat{m} = \lfloor \frac{M_{\text{Per}} - 1}{2} \rfloor$ would contradict assumption (A3). If the signal parametrization is chosen correctly, there is a confined area within the periodogram with indices $n \leq N_{\max}$, $m \leq M_{\max}$ which contains all the peaks, where N_{\max} and M_{\max} are chosen appropriately.

The exact amount of calculations required to obtain this cropped periodogram from \mathbf{F} therefore consists of:

- M IFFTs of length N_{Per} . The resulting vectors are cropped to length N_{\max} .

- N_{\max} FFTs of length M_{Per} . Again, the resulting vectors are cropped to length $2M_{\max} + 1$.
- One magnitude-square operation for every of the remaining $N_{\max} \times (2M_{\max} + 1)$ complex values.

Calculating $\text{Per}_{\text{F}}(n, m)$ thus only consists of basic signal processing steps, which can easily be implemented on FPGA- or GPP-based platforms. There are two major ways to implement this:

Serialized implementation Here, the processing is set up as a pipeline, such that the output of one step can directly be used as an input for the next, as in the block diagram in Fig. 3.6. This approach requires a very small memory footprint and is suitable for FPGA platforms which can operate at high clock rates.

Parallel implementation An alternative way is to load the entire matrix into a buffer and perform the (I)FFT operations in situ. This type of implementation is ideal for platforms which support Single-Instruction Multiple-Data (SIMD) operations, which can execute many identical signal processing operations simultaneously. With maximum parallelization, all FFTs can be executed at once (the same is true for the IFFTs), resulting in a very small execution time.

For this project, a GPP-based parallel implementation was created using the GNU Radio framework [119]. Depending on the frame size, it was possible to calculate a few hundred periodograms per second on a standard PC platform without even utilizing the entire CPU.

3.3.3 Estimation theoretic observations

The periodogram is a practical method (and, as was shown in the previous section, computationally inexpensive), but can it be justified by estimation theory as well? To answer this question, the Maximum Likelihood Estimator (MLE) shall be derived for the case where there is exactly one target and there is no prior information about the target (e.g. from a tracking system). The derivations in this section largely follow [4, 6].

A parameter vector is defined as

$$\boldsymbol{\theta} = (\tau, f_D, b, \varphi). \quad (3.42)$$

This vector also includes the phase offset, which is not required for the radar image. However, since it is unknown, it affects the estimation process, as will be seen later on.³

The derivation of a maximum likelihood estimator requires the likelihood function for \mathbf{F} for a given parameter vector. As the entries of \mathbf{F} are considered uncorrelated, the likelihood function is

$$f(\mathbf{F}|\boldsymbol{\theta}) = \prod_{k=0}^{N-1} \prod_{l=0}^{M-1} \frac{1}{\pi\sigma_N^2} e^{-\frac{|(\mathbf{F})_{k,l} - be^{j(2\pi(lT_O f_D - k\tau\Delta f) + \varphi)}|^2}{\sigma_N^2}}, \quad (3.43)$$

where σ_N^2 is the variance of the elements of \mathbf{Z} . The maximization process is simplified when the log-likelihood function is considered,

$$\ell(\mathbf{F}|\boldsymbol{\theta}) = \sum_{k=0}^{N-1} \sum_{l=0}^{M-1} \left(-\log \pi\sigma_N^2 - \frac{1}{\sigma_N^2} \left| (\mathbf{F})_{k,l} - be^{j(2\pi(lT_O f_D - k\tau\Delta f) + \varphi)} \right|^2 \right). \quad (3.44)$$

This function can be simplified further. The first term does not depend on any of the estimation parameters and thus does not affect maximization; it can safely be ignored. The same goes for the constant positive factor $1/\sigma_N^2$ in the second term.

The modulus squared is further evaluated using the identity $|a|^2 = a^* a$, where a^* denotes the complex conjugate:

$$\begin{aligned} & \left| (\mathbf{F})_{k,l} - be^{j(2\pi(lT_O f_D - k\tau\Delta f) + \varphi)} \right|^2 = \\ & |(\mathbf{F})_{k,l}|^2 + b^2 - 2b \operatorname{Re} \left[(\mathbf{F})_{k,l} e^{-j(2\pi(lT_O f_D - k\tau\Delta f) + \varphi)} \right] \end{aligned} \quad (3.45)$$

Again, the constant terms can be ignored for maximization. The simplified log-likelihood function is thus

$$\tilde{\ell}(\mathbf{F}|\boldsymbol{\theta}) = 2b \sum_{k=0}^{N-1} \sum_{l=0}^{M-1} \operatorname{Re} \left[(\mathbf{F})_{k,l} e^{-j(2\pi(lT_O f_D - k\tau\Delta f) + \varphi)} \right] - b^2. \quad (3.46)$$

³In spectral estimation literature, it is often referred to as a *nuisance parameter*.

The maximum likelihood estimate (MLE) for the parameter vector is defined as the value which maximizes the logarithmic likelihood function [85],

$$\hat{\boldsymbol{\theta}}_{\text{ML}} = \arg \max_{\boldsymbol{\theta}} \tilde{\ell}(\mathbf{F}|\boldsymbol{\theta}). \quad (3.47)$$

The question remains as to how the MLE can be calculated in accordance with (3.47). Directly calculating the MLE from (3.46) would require solving $\nabla_{\boldsymbol{\theta}} \ell(\mathbf{F}|\hat{\boldsymbol{\theta}}_{\text{ML}}) = \mathbf{0}$ which is anything but trivial as $\hat{\boldsymbol{\theta}}_{\text{ML}}$ is only given implicitly in a non-linear set of equations.

A simpler approach can be found by rearranging (3.46):

$$\tilde{\ell}(\mathbf{F}|\boldsymbol{\theta}) = 2b \operatorname{Re} \left[e^{j\varphi} \sum_{k=0}^{N-1} \left(\sum_{l=0}^{M-1} (\mathbf{F})_{k,l} e^{-j2\pi l T_O f_D} \right) e^{j2\pi k \tau \Delta f} \right] - b^2. \quad (3.48)$$

The sum inside the real operator can be interpreted as a continuous complex periodogram. By discretizing it in the same manner as (3.29) and (3.30), a quantized log-likelihood function is given as

$$\ell_Q(\mathbf{F}|n, m, b, \varphi) = 2b \operatorname{Re} [e^{j\varphi} \text{CPer}_{\mathbf{F}}(n, m)] - b^2, \quad (3.49)$$

which is maximized w.r.t. n and m . These values can be translated into Doppler shift and delay by

$$\tau(n) = \frac{n}{N_{\text{Per}} \Delta f}, \quad (3.50)$$

$$f_D(m) = \frac{m}{M_{\text{Per}} T_O}. \quad (3.51)$$

The maximum of $\ell_Q(\mathbf{F}|n, m, b, \varphi)$ can still not be evaluated analytically, but as there is only a finite number of values for n and m , it can be solved algorithmically by searching the range of all possible values.

Finally, the phase φ has to be taken care of. If $b > 0$, then the value φ which maximizes $\ell_Q(\mathbf{F}|n, m, b, \varphi)$ is $\varphi = \arg [\text{CPer}_{\mathbf{F}}(n, m)]$. By inserting this into (3.49), $\ell_Q(\mathbf{F}|n, m, b, \varphi)$ becomes

$$\ell_Q(\mathbf{F}|n, m, b) = 2b |\text{CPer}_{\mathbf{F}}(n, m)| - b^2, \quad (3.52)$$

As $b > 0$, the values (n, m) which maximize (3.52) are those which maximize $|\text{CPer}(n, m)|$, or, equivalently, $|\text{CPer}_{\mathbf{F}}(n, m)|^2 = \text{Per}_{\mathbf{F}}(n, m)$. Finding the periodogram's peak is thus equivalent to the MLE.

Finding the value b which maximizes (3.52) can be obtained by solving $\partial/\partial b \ell_Q(\mathbf{F}|n, m, b) \stackrel{!}{=} 0$, which results in $\hat{b} = |\text{CPer}_{\mathbf{F}}(\hat{n}, \hat{m})|$. Given the point scatter model, (3.34) is thus the ML estimate for the RCS.

As discussed in the previous section, not all values (n, m) correspond to useful results. There exist values M_{\max}, N_{\max} which limit the search range, which means not all $N_{\text{Per}} \times M_{\text{Per}}$ values need to be searched for a maximum. This reduces both the computational load as well as the chance of false detections.

Quantization Error

The estimates (\hat{n}, \hat{m}) are ML estimates, but the discretization of f_D and τ causes a quantization error. There are two ways to mitigate this: Either create a finer mesh (i.e. increase N_{Per} and M_{Per}), or find a way to locally maximize $\tilde{\ell}(\mathbf{F}|\boldsymbol{\theta})$ near $\tau(\hat{n}), f_D(\hat{m})$. Both solutions are discussed in Section 3.3.5.

Cramér-Rao Bound

The Cramér-Rao lower bound (CRB) for the frequency estimate of line spectra in discrete-time, one-dimensional processes is well known, its derivation is found in [86, 87] among others.

For a single complex sinusoid with unit amplitude in AWGN with noise power σ_N^2 and N discrete samples, the CRB for the estimate of the frequency assuming unknown phase is

$$\text{var}\{\hat{\omega}\} \geq \frac{6\sigma_N^2}{(N^2 - 1)N}. \quad (3.53)$$

To transfer this to the case of distance estimation, first assume there is only one OFDM symbol available ($M = 1$). It consists of N values, and using (3.32), (3.53) can directly be converted into a CRB for the distance estimate:

$$\text{var}\{\hat{d}\} \geq \frac{6\sigma_N^2}{(N^2 - 1)N} \left(\frac{c_0}{4\pi\Delta f} \right)^2. \quad (3.54)$$

Calculating the CRB for the entire frame is highly complex due to the fact that the matrix \mathbf{F} consists of M OFDM symbols, each with a different, random and unknown initial phase, due to the unknown Doppler shift. Here, use is made of the fact that the presented estimators have some kind of implicit averaging to identify a simpler lower bound: First, realize that every OFDM symbol can be used for one estimation $d_i, i = 1 \dots M$. As *white* noise is postulated as the source of error, the d_i represent *independent* estimates of d . Probability theory dictates that by averaging, an estimate \hat{d} is obtained with variance

$$\text{var}[d] = \frac{1}{M} \text{var}\{d_i\}. \quad (3.55)$$

This is now applied to (3.54), yielding

$$\text{var}[\hat{d}] \geq \frac{6\sigma_N^2}{(N^2 - 1)NM} \left(\frac{c_0}{4\pi\Delta f} \right)^2. \quad (3.56)$$

This bound is called the *averaged* CRB because it is not a true CRB any more, but is still a useful lower bound for the analyses presented here.

In a similar fashion, a lower bound for \hat{v}_{rel} can be given,

$$\text{var}[\hat{v}_{\text{rel}}] \geq \frac{6\sigma_N^2}{(M^2 - 1)MN} \left(\frac{c_0}{4\pi T_O f_C} \right)^2. \quad (3.57)$$

It is worth pointing out the influence of SNR on the bounds, since they both share dependencies. By using $\text{SNR} = 1/\sigma_N^2$ and $B = N\Delta f$, insert (3.13) into (3.56) and (3.57), yielding

$$\text{var}[\hat{d}] \geq \frac{6(4\pi)N_0}{P_{\text{Tx}}G} \cdot \frac{r^4}{\sigma_{\text{RCS}}} \cdot \frac{f_C^2}{(N^2 - 1)M\Delta f}, \quad (3.58)$$

$$\text{var}[\hat{v}] \geq \underbrace{\frac{6(4\pi)N_0}{P_{\text{Tx}}G}}_{\text{Hardware}} \cdot \underbrace{\frac{r^4}{\sigma_{\text{RCS}}}}_{\text{Target}} \cdot \underbrace{\frac{\Delta f}{(M^2 - 1)MT_O^2}}_{\text{Signal parameters}}. \quad (3.59)$$

Interpreting (3.58) and (3.59) gives three insights in particular into the system design:

- Given the point-scatter approximation, f_C only influences \hat{d} in a manner that lowering the frequency decreases the lower bound, whereas \hat{v}_{rel} is unaffected.

- Increasing M decreases the lower bound for both estimates, but as this means increasing the signal duration, it also increases medium access and allows for fewer measurements per time unit.
- When increasing the bandwidth, it is advantageous to increase N rather than Δf . This is only possible within limits given by the channel characteristics, most importantly the channel's coherence bandwidth (see also Section 3.6 and [1]).

Finally, it must not be forgotten that the CRB is a suitable quality metric only for *unbiased* estimators, and comparing to the actual estimates only makes sense above a certain SNR as will be discussed in the following.

Estimation error

In [87], Rife argues that below a certain SNR (the *SNR threshold*), any point in the periodogram has an equal chance of being the largest due to the whiteness of AWGN. In OFDM radar, this is the same: When the energy backscattered by the target is too small, it becomes indistinguishable from noise in the periodogram, and any point can be the largest.

Already, this reveals several things about the estimator: At low SNR, it cannot be unbiased, and it can potentially “detect” targets which are in reality artefacts of noise (false alarms). This motivates the introduction of a threshold test to the estimation process, which involves comparing the amplitude of the detected target with a predetermined threshold to verify it as a valid target. Section 3.3.6 discusses this in greater detail.

The metric to test the performance of the MLE is thus the probability with which the estimates (\hat{n}, \hat{m}) are correct. Let (n_0, m_0) be the true

values, and define a “root periodogram”,

$$\begin{aligned}
 C(n, m) &:= \sqrt{\text{Per}_{\mathbf{F}}(n, m)} \\
 &= \frac{1}{\sqrt{NM}} \left| \sum_{k=0}^{N_{\text{Per}}-1} \left(\sum_{l=0}^{M_{\text{Per}}-1} (\mathbf{F})_{k,l} e^{-j2\pi \frac{lm}{M_{\text{Per}}}} \right) e^{j2\pi \frac{kn}{N_{\text{Per}}}} \right| \\
 &= \left| \underbrace{\sum_{k=0}^{N_{\text{Per}}-1} \left(\sum_{l=0}^{M_{\text{Per}}-1} e^{-j2\pi l \frac{m-m_0}{M_{\text{Per}}}} \right)}_{\text{Signal term } A(n,m)} e^{j2\pi k \frac{n-n_0}{N_{\text{Per}}}} + (\mathbf{Z})_{m,n} \right|. \quad (3.60)
 \end{aligned}$$

The signal term is given by

$$A(n, m) = b\sqrt{NM} \left| \frac{\sin(\pi N \frac{n-n_0}{N_{\text{Per}}})}{N \sin(\pi \frac{n-n_0}{N_{\text{Per}}})} \frac{\sin(\pi M \frac{m-m_0}{M_{\text{Per}}})}{M \sin(\pi \frac{m-m_0}{M_{\text{Per}}})} \right|. \quad (3.61)$$

As discussed in Section 3.3.1, the summation causes the amplitude to be scaled by \sqrt{NM} , whereas the noise term is still AWGN with noise power σ_N^2 , the same as on the input.

Every value $C(n, m)$ is thus a random variable with a Rician distribution of the form

$$f_{C(n,m)}(x) = \frac{2x}{\sigma_N^2} e^{-\frac{(x^2 + A^2(n,m))}{\sigma_N^2}} I_0 \left(\frac{2xA(n, m)}{\sigma_N^2} \right), \quad (3.62)$$

where $x \geq 0$ and $I_0(x)$ denotes the modified Bessel function of order zero.

The estimator result is also a random variable and shall be denoted by $(\hat{\mathbf{m}}, \hat{\mathbf{n}})$. Its PDF is given by $f_{(\hat{\mathbf{n}}, \hat{\mathbf{m}})}(n, m | n_0, m_0)$ and depends on (n_0, m_0) . From all (n, m) within the search range, the estimator decides for the particular value (\hat{n}, \hat{m}) whenever $C(\hat{n}, \hat{m})$ is larger than any other

$C(n, m)$. The probability for this is

$$\begin{aligned}
 f_{\hat{\mathbf{n}}, \hat{\mathbf{m}}}(\hat{n}, \hat{m}|n_0, m_0) &= \Pr [C(\hat{n}, \hat{m}) > C(n, m) | \forall n \neq \hat{n}, m \neq \hat{m}] \\
 &= \int_x \Pr [C(n, m) < x | n \neq \hat{n}, m \neq \hat{m}] f_{C(\hat{n}, \hat{m})}(x) dx \\
 &= \int_0^\infty f_{C(\hat{n}, \hat{m})}(x) \left[\prod_{\substack{n \neq \hat{n} \\ m \neq \hat{m}}} \int_0^x f_{C(n, m)}(y) dy \right] dx \\
 &= \int_0^\infty f_{C(\hat{n}, \hat{m})}(x) \left[\prod_{\substack{n \neq \hat{n} \\ m \neq \hat{m}}} F_{C(n, m)}(x) \right] dx
 \end{aligned} \tag{3.63}$$

where $F_{C(n, m)}(x)$ is the cumulative density of the value of $C(n, m)$,

$$F_{C(n, m)}(x) = 1 - Q_1 \left(\frac{A(n, m)\sqrt{2}}{\sigma_N}, \frac{x\sqrt{2}}{\sigma_N} \right) \tag{3.64}$$

and $Q_1(\cdot, \cdot)$ is the Marcum Q-function.

The complete PDF for $(\hat{\mathbf{n}}, \hat{\mathbf{m}})$ is calculated for a given (n_0, m_0) and SNR by solving the integral for every possible value of (\hat{n}, \hat{m}) in the search range.⁴

Having calculated the PDF $f_{\hat{\mathbf{n}}, \hat{\mathbf{m}}}(\hat{n}, \hat{m}|n_0, m_0)$, it is now possible to calculate the expected value and variance of the estimator. Using these and (3.32) to translate \hat{n} and \hat{m} into a range and velocity, respectively,

⁴(3.63) can be solved numerically, but requires special attention due to the combination of Bessel and exponential functions, which can have extremely large or small values and can thus become numerically unstable. Numerically demanding calculations were done with the help of the arbitrary precision tools for the Python programming language. The methods used to calculate $Q_1(\cdot, \cdot)$ are those explained in [70].

equations for bias and variance of the range and Doppler are

$$\text{bias}[d] = \frac{c}{2N_{\text{Per}}\Delta f} (\mathbb{E}\{\hat{\mathbf{n}}\} - n_0), \quad (3.65)$$

$$\text{var}[d] = \left(\frac{c}{2N_{\text{Per}}\Delta f} \right)^2 \mathbb{E}\{(\hat{\mathbf{n}} - \mathbb{E}\{\hat{\mathbf{n}}\})^2\}, \quad (3.66)$$

$$\text{bias}[v_{\text{rel}}] = \frac{c}{2M_{\text{Per}}T_{\text{OfC}}} (\mathbb{E}\{\hat{\mathbf{m}}\} - m_0), \quad (3.67)$$

$$\text{var}[v_{\text{rel}}] = \left(\frac{c}{2M_{\text{Per}}T_{\text{OfC}}} \right)^2 \mathbb{E}\{(\hat{\mathbf{m}} - \mathbb{E}\{\hat{\mathbf{m}}\})^2\}. \quad (3.68)$$

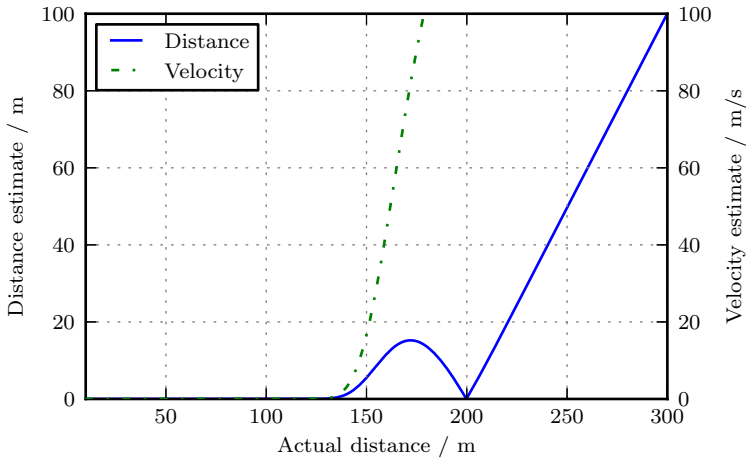
Fig. 3.8 shows bias and variance for an OFDM radar system parametrized as described in Section 3.6.2 (wideband signal). The target RCS was fixed to $\sigma_{\text{RCS}} = 10 \text{ m}^2$, which means the SNR is directly proportional to $\propto 1/d^4$. It can be seen that bias and variance stay close to zero until a certain range is exceeded (i.e. SNR falls below a certain value). As soon as this occurs, the estimation error rises very quickly, making the estimator unusable in practice beyond this SNR threshold.

Fig. 3.9 shows the probability $\Pr[\hat{n} = n_0, \hat{m} = m_0]$ of estimating the correct values. The results confirm that the estimator works very well above the SNR threshold, but very poorly below.

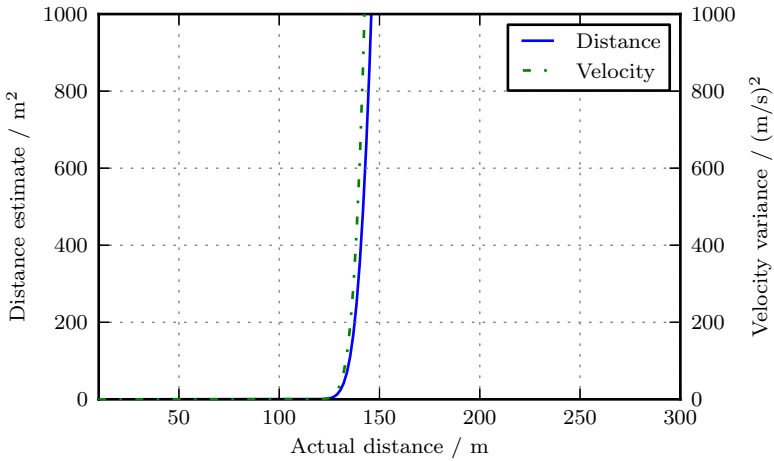
It is emphasized that (3.65) through (3.68) are calculated from an estimator for (n, m) , and not (d, v_{rel}) ! Because of the aforementioned quantization error, the range and Doppler estimates are worse than the estimates for n and m . The value of this analysis is that it provides a way to numerically calculate bias and variance of an otherwise mathematically intractable problem.

To obtain true bias and variance of a complete OFDM radar system, including quantization error and interpolation algorithms to remove the latter, simulations are required which are presented in Section 5.2.

It can be argued that the bias is not a useful metric in this case, as it does not show a systematic error of the estimation, but rather a random offset. A large bias is thus more of an indicator that the estimation is not working correctly, the numeric value of the bias itself does not hold any useful information about the estimation process. For this reason, the probability of estimating the correct bin can be chosen to determine the quality of the estimator, which is less misleading.



(a) Bias of the distance and velocity estimates.



(b) Variance of the distance and velocity estimates.

Figure 3.8: Performance of target velocity and distance estimation against actual distance

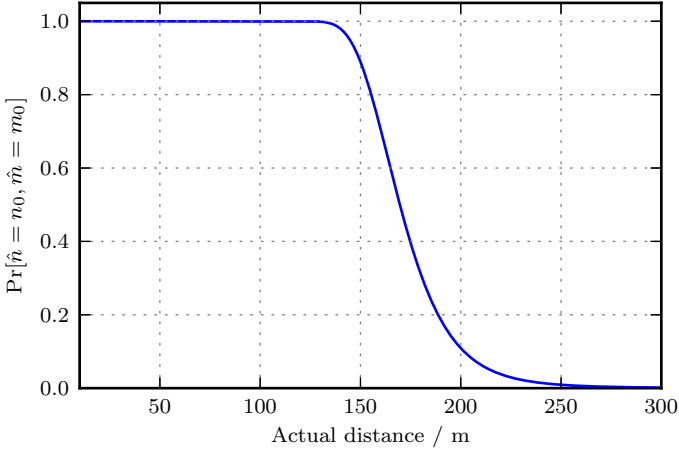


Figure 3.9: Probability of correct value estimation.

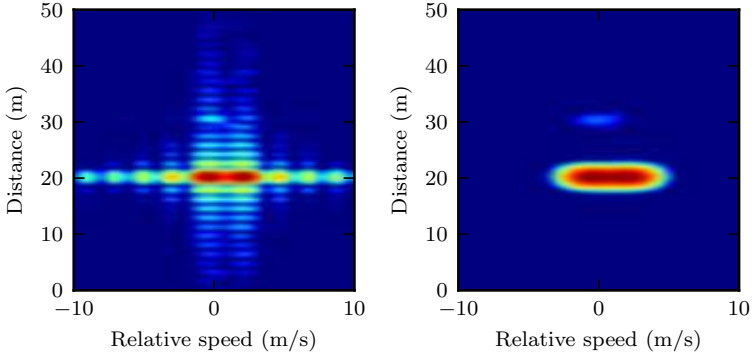
3.3.4 Window functions

In periodogram-based spectral estimation, window functions⁵ are commonly applied to the input data. Window functions have two relevant properties: the width of the main lobe Ω_s , where $-\pi \leq \Omega_s \leq \pi$, and the sidelobe attenuation a_{\min} , given in dB.

The main advantage is the precise control of sidelobe levels, which is useful for the reliable detection of targets. Fig. 3.10 shows the same periodogram for two identical cases, but each using a different window. In the first case, the main lobe width is very small and close targets can be distinguished (i.e. the resulting radar resolution is better). The second periodogram uses a window with high sidelobe attenuation; this allows weaker targets to be distinguished from sidelobes of the stronger targets, but reduces the resolution.

For the two-dimensional periodogram, a two-dimensional window matrix $\mathbf{W} \in \mathbb{R}^{N \times M}$ is defined, which is multiplied element-wise with the matrix

⁵Sometimes referred to as *taper functions*.



(a) Rectangular window. The two targets at 20 m are easily distinguished. (b) Dolph-Chebyshev window. The target at 30 m now clearly stands out.

Figure 3.10: Periodogram of three targets.

F. (3.30) is thus refined to

$$\text{Per}_{\mathbf{F}}(n, m) = \frac{1}{NM} \underbrace{\left(\sum_{k=0}^{N_{\text{Per}}-1} \left(\sum_{l=0}^{M_{\text{Per}}-1} (\mathbf{F})_{k,l} (\mathbf{W})_{k,l} e^{-j2\pi \frac{lm}{M_{\text{Per}}}} \right) \right)}_{M_{\text{Per}} \text{ IFFTs of length } N_{\text{Per}}} e^{j2\pi \frac{kn}{N_{\text{Per}}}} \Bigg|^2. \quad (3.69)$$

If \mathbf{W} is left out, as in (3.30), a boxcar window ($(\mathbf{W})_{k,l} = 1$) is implicitly used.

Window matrices are designed by calculating the outer product of two one-dimensional windows,

$$\mathbf{W} = \frac{1}{\|\mathbf{w}_d\|^2 \|\mathbf{w}_v\|^2} \mathbf{w}_d^T \otimes \mathbf{w}_v, \quad \mathbf{w}_d \in \mathbb{R}^{1 \times N}, \quad \mathbf{w}_v \in \mathbb{R}^{1 \times M}. \quad (3.70)$$

The normalization factor is introduced to ensure that the total energy in the periodogram is independent of the chosen window matrix.

It is possible to choose different window types for \mathbf{w}_d and \mathbf{w}_v , but this would only be useful for some rare cases, e.g. if there is a large difference

Window	Main lobe width	Sidelobe attenuation
Rectangular	$\Omega_s = 2\pi/N$	$a_{\min} = 13.3 \text{ dB}$
Hamming	$\Omega_s = 4\pi/N$	$a_{\min} \approx 42 \text{ dB}^7$
Blackman-Harris	$\Omega_s \approx 8\pi/N$	$a_{\min} = 92.1 \text{ dB}$
Dolph-Chebyshev	$\Omega_s \approx \frac{1.46\pi(\log_{10} 2 + a_{\min}/20)}{N-1}$	user-defined

Table 3.2: Properties of window functions used.

between the values of N and M . Here, only window matrices with identical window types for rows and columns are considered (for the sake of readability, only the definition for \mathbf{w}_d is given; \mathbf{w}_v can be calculated in an analog fashion by replacing N with M). The following window types are of interest for the OFDM radar application:⁶

Rectangular (boxcar) windows This can also be interpreted as a “lack” of a window function as all entries are of unit value,

$$(\mathbf{w}_d)_k = 1, \quad k = 0, \dots, N-1. \quad (3.71)$$

The rectangular window has the smallest main lobe width (which is optimal for the radar resolution). However, it also has the smallest side lobe attenuation (which is bad for the dynamic range), which makes it generally not a good choice for the radar system.

Hamming windows Compared to the rectangular window, these windows have a higher sidelobe attenuation (see Table 3.2), but twice the main lobe width. Hamming windows have been used in combination with radar systems before (e.g. in [38]) and therefore were analyzed here as well. They are defined by

$$(\mathbf{w}_d)_k = 0.54 - 0.46 \cos\left(\frac{2\pi k}{N-1}\right). \quad (3.72)$$

⁶For more information on these windows, cf. [102, Chap. 7], and [101] for details on the Blackman-Harris window.

⁷This value is only correct for $N \geq 32$.

Blackman-Harris windows An alternative to the Hamming window with an extremely high sidelobe attenuation is the Blackman-Harris window, which is defined as

$$\begin{aligned}
 (\mathbf{w}_d)_k &= a_0 - a_1 \cos\left(\frac{2\pi k}{N-1}\right) - a_2 \cos\left(\frac{4\pi k}{N-1}\right) - a_3 \cos\left(\frac{6\pi k}{N-1}\right) \\
 a_0 &= 0.35875, a_1 = 0.48829, a_2 = 0.14128, a_3 = 0.01168.
 \end{aligned}
 \tag{3.73}$$

The main lobe is nearly twice as wide as that of the Hamming window, but the very high sidelobe attenuation effectively allows sidelobes to be treated as if they were non-existent, because in most cases the dynamic range will actually be smaller than a_{\min} .

Dolph-Chebyshev windows Dolph-Chebyshev windows have a unique property: the sidelobe attenuation is constant over the entire frequency band. It is also parametrizable, which means the sidelobe attenuation can be configured according to the required dynamic range. The main lobe width depends on the chosen sidelobe attenuation (see Table 3.2). Because the sidelobe energy is constant outside the main lobe and does not decrease with Ω as with the other windows, the main lobes of Dolph-Chebyshev windows are usually slightly smaller than those of the other windows at equivalent sidelobe attenuations (e.g. a Dolph-Chebyshev window with 92.1 dB sidelobe attenuation has a slightly smaller main lobe than a Blackman-Harris window of equal length).

Dolph-Chebyshev windows are designed in the frequency domain, the final window is calculated with an Inverse Discrete Fourier Transformation (IDFT) (or Inverse Fast Fourier Transformation (IFFT)):

$$\mathbf{w}_d = \text{IFFT}_N \left[\mathbf{W}_d e^{-j(N-1)\Omega/2} \right],
 \tag{3.74}$$

where

$$(\mathbf{W}_d)_k = \begin{cases} \cosh\left((N-1) \cdot \text{arccosh}\left(\frac{\cos(\frac{\pi k}{N})}{\cos(\Omega_s/2)}\right)\right), & 0 \leq \Omega \leq \Omega_s, \\ \cos\left((N-1) \cdot \text{arccos}\left(\frac{\cos(\frac{\pi k}{N})}{\cos(\Omega_s/2)}\right)\right), & \Omega_s \leq \Omega \leq \pi. \end{cases}
 \tag{3.75}$$

SNR loss by windowing

The application of a window does not affect the signal-to-noise ratio at the input of the periodogram, because the element-wise multiplication with \mathbf{W} affects noise and signal in the same manner. The choice of the window function has an impact on the signal-to-noise ratio in the periodogram, though. Because the main lobe's widths differ between the presented windows, the height of their peaks also varies, resulting in an SNR loss.

Fig. 3.19 shows several windows both in time- and frequency domain. The SNR loss can be seen in the frequency domain; the rectangular window has the highest peak.

Such a loss needs to be factored into the processing gain. For arbitrary windows, it is therefore calculated as

$$\text{PG} = 10 \cdot \log_{10}(NM) + \text{SNR}_{\mathbf{w}_d} + \text{SNR}_{\mathbf{w}_v}, \quad (3.76)$$

where $\text{SNR}_{\mathbf{w}_d}$ and $\text{SNR}_{\mathbf{w}_v}$ are the SNR losses for the row- and column-wise windows, respectively. They are given by

$$\text{SNR}_{\mathbf{w}_d} = \frac{1}{\|\mathbf{w}_d\|^2 N} \left| \sum_{k=0}^{N-1} (\mathbf{w}_d)_k \right|^2, \quad (3.77)$$

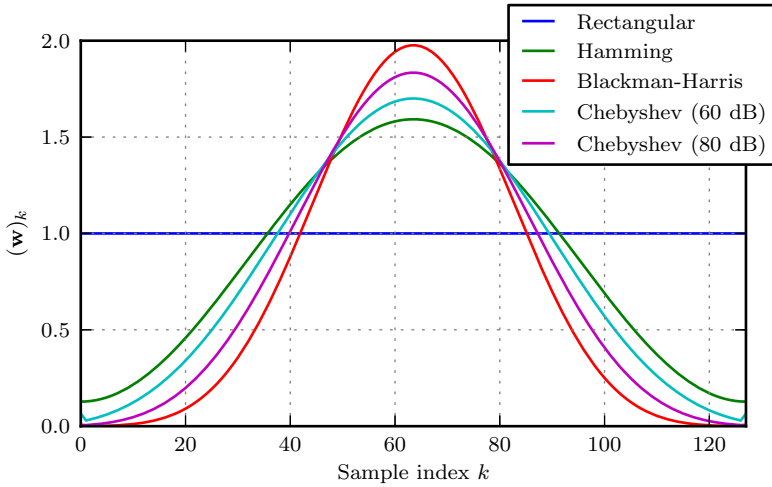
$$\text{SNR}_{\mathbf{w}_v} = \frac{1}{\|\mathbf{w}_v\|^2 M} \left| \sum_{k=0}^{M-1} (\mathbf{w}_v)_k \right|^2, \quad (3.78)$$

$$(3.79)$$

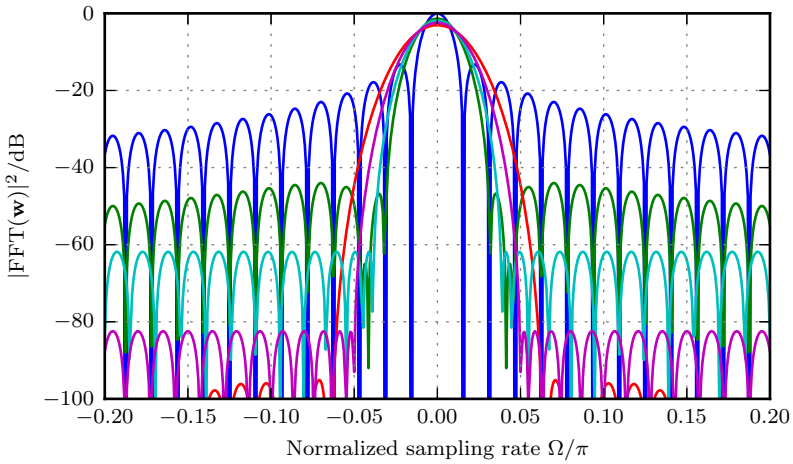
which corresponds to the DC bin of the individual windows' periodogram normalized to the height of the rectangular window. Table 3.3 gives some values for different types of windows and lengths. It should be noted that some windows induce a significant loss of SNR.

3.3.5 Quantization issues and interpolation

Up until now, the range of possible estimates is quantized on a regular grid, as the values \hat{n} and \hat{m} in (3.32) are integer values. This introduces two negative effects: quantization noise and scalloping loss. These are discussed in the following, as well as a solution for the quantization problem.



(a) Time-domain representation. Windows are normalized to unit energy.



(b) Frequency-domain representation (logarithmic). Windows are normalized to peak of rectangular window.

Figure 3.11: Different window functions in one dimension with length $N = 128$.

	Rectangular	Hamming	Blackman-Harris	Dolph-Chebyshev
$N = 52$	0 dB	-1.40 dB	-3.10 dB	-1.88 dB
$N = 256$	0 dB	-1.36 dB	-3.04 dB	-1.82 dB
$N = 1024$	0 dB	-1.35 dB	-3.02 dB	-1.81 dB

Table 3.3: SNR loss for different window types and -lengths

Quantization noise

On a quantized grid, estimates are only correct up to a quantization error. Assuming a uniform distribution of true range and Doppler shifts, the estimation is distorted by zero-mean, uniformly distributed quantization noise with variances (or quantization noise power)

$$\text{var}_Q[\hat{d}] = \frac{1}{12} \left(\frac{c_0}{2\Delta f N_{\text{Per}}} \right)^2, \quad (3.80)$$

$$\text{var}_Q[\hat{v}] = \frac{1}{12} \left(\frac{c_0}{2f_C T_O M_{\text{Per}}} \right)^2. \quad (3.81)$$

Not only does this mean that the estimates are incorrect, but also that the error on the estimates is non-Gaussian, and possibly not uncorrelated between measurements. This can affect some post-processing components, such as tracking algorithms, if they assume a Gaussian distribution of the estimation error, such as Kalman filters do (cf. also [98, Chap. 19]).

Scalloping loss

Scalloping loss⁸ is another effect caused by the regular grid of FFT-based processing.⁹ If the true frequency of a sinusoid does not lie directly on one of the DFT bins, not only is the frequency estimate incorrect (which distorts the range or the Doppler estimation), but also its amplitude. In the worst case, this can cause a valid target to be mistaken for noise, but even if it is detected, the estimated amplitude is probably too low, thereby increasing the error of the Radar Cross Section (RCS).

⁸In radar literature [98], this effect is usually referred to as *straddle loss*.

⁹R. Lyons [108] gives an excellent introduction to this topic.

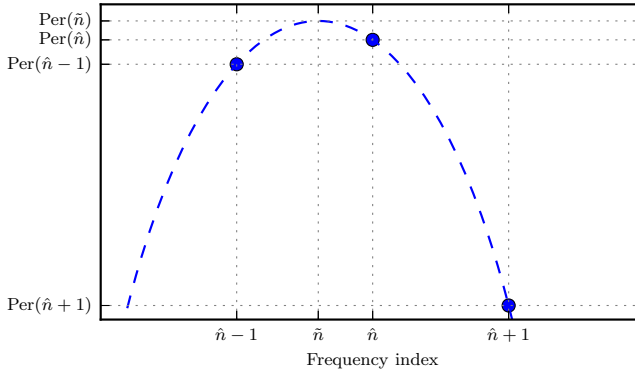


Figure 3.12: Part of the periodogram of a sinusoid with a frequency between the discrete DFT bins, normalized to its maximum value. If the maximum value of the discrete periodogram is used, the estimate will have a quantization error of $\hat{n} - \tilde{n}$ and a scalloping loss of $\text{Per}(\hat{n}) - \text{Per}(\tilde{n})$.

Fig. 3.12 shows the periodogram of a one-dimensional sinusoid, multiplied with a rectangular window. The maximum value of the continuous periodogram is between two bins, thereby causing scalloping loss and quantization noise if the FFT's peak is used as an estimate.

Interpolation

To overcome these problems, the estimation can be augmented by interpolation. One way to interpolate is to simply increase N_{Per} and M_{Per} , i.e. to pad with more zeros. While this does not change the fact that the quantization noise is uniformly distributed, its power can be decreased until the receiver noise dominates the estimation error. However, this method is not very efficient, as it interpolates the *entire* periodogram and thereby increases memory usage and computational cost.

A more efficient way is to use a periodogram with little or no zero padding to first get a coarse, quantized estimate and then interpolate

locally, which means the computational cost increases as a function of the number of detected targets.

In the following, three interpolation methods are discussed, which differ by complexity and accuracy. All three methods assume that the results from the coarse estimate are accurate within quantization, i.e. that the coarse estimate correctly identified a target (and not detected a false alarm). Also, these methods make use of the shape of the windows' main lobes, which means they work less accurately when two targets are closer to each other than the available resolution. This highlights the fact that the *accuracy* of a radar system can be improved with such methods, but the range and Doppler resolution are always fixed by the bandwidth and frame duration, respectively.

Relying on a correct initial estimate also implies that missed detections caused by scalloping loss cannot be improved using interpolation.

All interpolation methods result in *fractional* (i.e. real-valued) periodogram indices (\tilde{n}, \tilde{m}) . These indices can be used instead of \hat{n} and \hat{m} in (3.32) to obtain a non-quantized estimate for range and Doppler.

Linear interpolation Here, not only $\text{Per}_{\mathbf{F}}(\hat{n}, \hat{m})$ is considered but also the four points in the periodogram directly adjacent. The periodogram must have a local maximum at $\text{Per}_{\mathbf{F}}(\hat{n}, \hat{m})$. Fractional periodogram indices \tilde{n} and \tilde{m} are calculated by

$$\tilde{n} = \frac{(\hat{n} - 1) \text{Per}_{\mathbf{F}}(\hat{n} - 1, \hat{m}) + \hat{n} \text{Per}_{\mathbf{F}}(\hat{n}, \hat{m}) + (\hat{n} + 1) \text{Per}_{\mathbf{F}}(\hat{n} + 1, \hat{m})}{\text{Per}_{\mathbf{F}}(\hat{n} - 1, \hat{m}) + \text{Per}_{\mathbf{F}}(\hat{n}, \hat{m}) + \text{Per}_{\mathbf{F}}(\hat{n} + 1, \hat{m})}, \quad (3.82)$$

$$\tilde{m} = \frac{(\hat{m} - 1) \text{Per}_{\mathbf{F}}(\hat{n}, \hat{m} - 1) + \hat{m} \text{Per}_{\mathbf{F}}(\hat{n}, \hat{m}) + (\hat{m} + 1) \text{Per}_{\mathbf{F}}(\hat{n}, \hat{m} + 1)}{\text{Per}_{\mathbf{F}}(\hat{n}, \hat{m} - 1) + \text{Per}_{\mathbf{F}}(\hat{n}, \hat{m}) + \text{Per}_{\mathbf{F}}(\hat{n}, \hat{m} + 1)}. \quad (3.83)$$

The linear interpolation offers no way to interpolate the height of the periodogram at (\tilde{n}, \tilde{m}) and is therefore as susceptible to scalloping loss as the coarse estimate.

Quadratic interpolation By approximating the main lobe of the window with a two-dimensional parabola, the estimation can be further improved. Because no window's lobe is exactly shaped like a parabola, an error still remains, but the calculation of the estimate is very simple; if (\hat{n}, \hat{m}) are the coordinates of a peak in the periodogram, fractional indices are calculated by

$$\tilde{n} = \hat{n} + \frac{\text{Per}_{\mathbf{F}}(\hat{n} - 1, \hat{m}) - \text{Per}_{\mathbf{F}}(\hat{n} + 1, \hat{m})}{2(\text{Per}_{\mathbf{F}}(\hat{n} - 1, \hat{m}) + \text{Per}_{\mathbf{F}}(\hat{n} + 1, \hat{m}) - 2\text{Per}_{\mathbf{F}}(\hat{n}, \hat{m}))}, \quad (3.84)$$

$$\tilde{m} = \hat{m} + \frac{\text{Per}_{\mathbf{F}}(\hat{n}, \hat{m} - 1) - \text{Per}_{\mathbf{F}}(\hat{n}, \hat{m} + 1)}{2(\text{Per}_{\mathbf{F}}(\hat{n}, \hat{m} - 1) + \text{Per}_{\mathbf{F}}(\hat{n}, \hat{m} + 1) - 2\text{Per}_{\mathbf{F}}(\hat{n}, \hat{m}))}. \quad (3.85)$$

As before, the interpolated values for the range and Doppler estimation are then calculated by replacing the integer values with the fractional values \tilde{m} and \tilde{n} in (3.32), respectively.

Another advantage is that the interpolated value of the parabola at position (\tilde{n}, \tilde{m}) can be used for the RCS estimation, thereby reducing the scalloping loss. The periodogram amplitude at the interpolated position is

$$\begin{aligned} \text{Per}_{\mathbf{F}}(\tilde{n}, \tilde{m}) &:= \text{Per}_{\mathbf{F}}(\hat{n}, \hat{m}) - \\ &\quad \frac{1}{4}((\text{Per}_{\mathbf{F}}(\hat{n} - 1, \hat{m}) - \text{Per}_{\mathbf{F}}(\hat{n} + 1, \hat{m}))(\tilde{n} - \hat{n}) \\ &\quad + (\text{Per}_{\mathbf{F}}(\hat{n}, \hat{m} - 1) - \text{Per}_{\mathbf{F}}(\hat{n}, \hat{m} + 1))(\tilde{m} - \hat{m})) \end{aligned} \quad (3.86)$$

See Appendix B for a derivation.

To use the quadratic interpolation, the dimensions of the quantized periodogram must be at least twice as large as those of \mathbf{F} , i.e. $N_{\text{Per}} \geq 2N$ and $M_{\text{Per}} \geq 2M$. Otherwise, one of the supporting points in (3.84) or (3.85) might actually not be on the parabola, but caused by noise or other spurs, potentially causing a large error.

Interpolation by optimization A different approach to interpolation is to re-cast the ML estimate as an optimization problem. Consider (3.47): while there is no explicit solution to this maximization problem, it could be solved by defining the periodogram with continuous arguments as an

objective function

$$\text{Per}_{\mathbf{F}}(\tilde{n}, \tilde{m}) = \frac{1}{NM} \left| \sum_{k=0}^{N_{\text{Per}}-1} \left(\sum_{l=0}^{M_{\text{Per}}-1} (\mathbf{F})_{k,l} e^{-j2\pi \frac{kl\tilde{m}}{M_{\text{Per}}}} \right) e^{j2\pi \frac{k\tilde{n}}{N_{\text{Per}}}} \right|^2, \quad (3.87)$$

which is similar to the periodogram (3.30), but uses continuous values as well as a rectangular window. Without any prior knowledge of the estimates, this is not a practical optimization problem, but if a previous, coarse estimate exists, the optimization problem becomes convex and can be solved with numerical methods.

Consider Fig. 3.12, which shows both the discrete and continuous periodogram of a one-dimensional discrete-time sinusoid,

$$s(k) = e^{j2\pi \frac{\tilde{n}}{N} k}, \quad k = 0, \dots, N-1. \quad (3.88)$$

\hat{n} is the coarse estimate for \tilde{n} , which is offset from the true value by the quantization error. Because the coarse estimate is chosen as the maximum of the discrete periodogram, it must be a point on the main lobe. Consequently, \hat{n} must be the integer value that minimizes $|\hat{n} - \tilde{n}|$. Also, the double zero-padding ensures that the values $\text{Per}_{s(k)}(\hat{n}+1)$ and $\text{Per}_{s(k)}(\hat{n}-1)$ also lie on the main lobe (a rectangular window's main lobe is four samples wide for $N_{\text{Per}} = 2N$). The main lobe is convex (as $\frac{\sin(\pi x)}{\pi x}$ is convex on the interval $x \in [-1, 1]$). Therefore, estimating the true peak position of the continuous periodogram is identical to finding the maximum of a convex function on the interval $\hat{n}-1, \dots, \hat{n}+1$.

Going back to the two-dimensional periodogram, and given coarse estimates (\hat{n}, \hat{m}) , the fractional indices are obtained by solving the optimization problem

$$\begin{aligned} (\tilde{n}, \tilde{m}) &= \arg \max_{(n,m)} \text{Per}_{\mathbf{F}}(n, m) \\ &\text{subject to} \\ \hat{n}-1 &\leq n \leq \hat{n}+1 \text{ and } \hat{m}-1 \leq m \leq \hat{m}+1 \end{aligned} \quad (3.89)$$

using the continuous periodogram from (3.87). At the same time, because the continuous periodogram is used as the objective function, the result $\text{Per}_{\mathbf{F}}(\tilde{n}, \tilde{m})$ can be used to estimate the target's RCS without scalloping loss.

One algorithm able to solve this bounded, two-dimensional optimization problem is the *Nelder-Mead simplex algorithm* [75]¹⁰ (for one dimension, [87] suggests a secant method which would not work for this two-dimensional problem). This algorithm requires initial values, which can either be the coarse indices (\hat{n}, \hat{m}) or even fractional indices from a previous quadratic interpolation for faster convergence.

3.3.6 Signal detection and false alarm rate

The algorithms presented in the previous section assumed a-priori knowledge; specifically, a coarse estimate of a target's position. In order to extract targets' positions from $\text{Per}_{\mathbf{F}}(n, m)$, a *target detector* must be part of the periodogram-based OFDM radar system (as depicted in Fig. 3.6). The target detector's job is to identify the peaks in the periodogram originating from valid radar targets, discriminating them from peaks originating from spurious influences. The two major sources for errors in this case are

- peaks caused by the AWGN, and
- ambiguities caused by targets' side lobes.

The latter case was already discussed in Section 3.3.4; essentially, two types of errors can arise from this:

1. Missed target: A valid target can be missed because it is identified as a side lobe of another, previously detected, target with higher backscattered power (decreased detection probability)
2. False alarm: A side lobe of a previously detected target can be identified as the main lobe of a non-existent target.

As mentioned previously, the choice of a suitable window matrix \mathbf{W} can alleviate this problem to a great extent, at the cost of reduced resolution. This leaves the question of how to deal with peaks caused by AWGN.

¹⁰MATLAB implements this algorithm in the `fminsearch` function.

Constant False Alarm Rate

Most radar systems are configured for a *constant false alarm rate* (CFAR), and this solution is also chosen for the OFDM radar system. The precise definition of the CFAR varies in literature (compare [98] and [97], for instance), which is why the following definitions are introduced:

A *false alarm* is the event where the target detector decides that there is a target at a range and relative speed which did not contribute to the received matrix \mathbf{F}_{Rx} . The probability of a false alarm P_{FA} is the probability that, during the processing of a single frame, one or more false alarms occur when only noise was present ($\mathbf{F}_{\text{Rx}} = \mathbf{Z}$). Finally, the false alarm rate (FAR) is the expected number of detections per processing of one frame, for the case that only noise was present.

This definition differs from other definitions of false alarm probability (and FAR) in several respects:

- The time base for the false alarm rate is the duration of one frame (as a comparison, [98] suggests the number of false alarms per second for the FAR). This makes the results discussed here independent of the update rate.
- Clutter is explicitly *not* discussed in this context. The detection of an object that backscatters energy, but is not of interest for the application, thus does not count as a false alarm (an example would be the detection of a traffic sign in a vehicular context).
- Other systems, such as target tracking algorithms [138], might further process the output of the target detector (cf. Fig. 3.6), thereby possibly further reducing the false alarm rate.

In order to discriminate noise from signal power, a threshold η is introduced, and the periodogram is subjected to a hypothesis test,

$$\text{Per}_{\mathbf{F}}(n, m) \underset{H_1}{\overset{H_0}{\lesseqgtr}} \eta, \quad (3.90)$$

where H_0 is the null hypothesis (no target is present) and H_1 is the hypothesis that a target contributes to the amplitude of the given bin.

To calculate the false alarm probability, let Z denote the (random) amplitude of any bin of $\text{Per}_{\mathbf{F}}(n, m)$ when only noise is present (due to the whiteness of the noise, Z is i.i.d. for all bins).

The probability that any single bin of the periodogram exceeds the threshold is

$$p_{\text{FA,bin}} := \Pr [z > \eta] = \int_{\eta}^{\infty} f_z(z|H_0) dz = 1 - F_Z(\eta|H_0) \quad (3.91)$$

$$= e^{-\frac{\eta}{\sigma_N^2}}, \quad (3.92)$$

where $f_z(z|H_0)$ and $F_Z(\eta|H_0)$ are the PDF and CDF, respectively, of the random variable Z . The exponential term (3.92) is the result of Z being the magnitude-squared of AWGN with power σ_N^2 , and thus exponentially (χ_2^2) distributed.

To achieve a certain per-bin false alarm rate, solve (3.92) for η :

$$\eta = -\sigma_N^2 \ln p_{\text{FA,bin}}. \quad (3.93)$$

The optimality of this detection method is discussed in [98, Chap. 15]. In order to achieve a specific false alarm probability, note that, for a non-zero-padded periodogram, the false alarm probability is

$$p_{\text{FA}} = 1 - (1 - p_{\text{FA,bin}})^{NM}. \quad (3.94)$$

Solving this for $p_{\text{FA,bin}}$ and inserting into (3.93) yields

$$\eta = \sigma_N^2 \ln(1 - (1 - p_{\text{FA}})^{\frac{1}{NM}}). \quad (3.95)$$

If the requirement is a certain FAR, which is calculated by

$$\text{FAR} = NM p_{\text{FA,bin}}, \quad (3.96)$$

the threshold is set by

$$\eta = -\sigma_N^2 \ln \frac{\text{FAR}}{NM}. \quad (3.97)$$

The choice between (3.95) and (3.97) is determined by a trade-off: Fixing a $\text{FAR} \geq 1$ results in a lower threshold than using (3.95), and thus higher detection probability, but increases the burden on post-processing components downstream, as it also increases the number of false alarms.

When using the cropped periodograms as described in Section 3.3.2, the factor NM is replaced by $N_{\text{max}}(2M_{\text{max}} + 1)$ in (3.95) and (3.97). However, when zero-padding is used, these values are *not* increased by the interpolation factor. It is true that if there are more bins in the periodogram due to zero-padding there are potentially more bins to cause

false alarms. However, zero-padding does not add information to the periodogram, it merely reduces quantization error, and adjacent bins in zero-padded periodogram are correlated. A single peak in a non-zero-padded periodogram will thus cause multiple elements of a zero-padded periodogram to lie above the threshold, but as they are contiguous, the detection algorithm (see Section 3.3.7) will only detect this peak once.

Noise power estimation

Usually, the noise power σ_N^2 is not known at the receiver. To still be able to specify a threshold, the noise power may be estimated from the periodogram by averaging over those bins which do not contain a target. As this happens before the target detection, it is unclear which bins correspond to targets.

The solution is to rely on the correct parametrization of the OFDM radar system: As discussed in Section 3.3.2, there is a maximum index (N_{\max}) after which no more peaks should appear. By averaging over one or more rows beyond N_{\max} , a maximum likelihood estimate for σ_N^2 can be found by

$$\hat{\sigma}^2 = \frac{1}{M_{\text{Per}}K} \sum_{k=1}^K \sum_{m=0}^{M_{\text{Per}}} \text{Per}_{\mathbf{F}}(N_{\text{Per}}, m), \quad (3.98)$$

where K is the number of rows over which to average. Unless M_{Per} is very small, a value of 1 or 2 for K is sufficient.

3.3.7 Multi-target detection

The periodogram is a two-dimensional matrix which contains power levels for range and Doppler values. An application using a radar system as a sensor requires a precise list of targets, together with their individual range, Doppler and RCS.

To obtain such a list from the $\text{Per}_{\mathbf{F}(n,m)}$, a multi-target detection algorithm is necessary.¹¹

The previous section discussed how to separate noise from single targets. With multiple targets, additional problems arise, most importantly:

¹¹In long-range radar applications, this process is usually referred to as *automatic target recognition* (ATR).

- Sidelobes from strong peaks might be misidentified as separate targets.
- Weak targets close to strong targets might be overshadowed, even if they are further apart than the radar resolution.

These problems are not independent, and there is a trade-off when trying to minimize them. This becomes clear when taking a look at the window functions in Section 3.3.4: A window with a very high sidelobe attenuation might entirely mitigate the first problem, but will also decrease the radar resolution and thus amplify the possibility of overshadowing smaller targets (cf. also Fig. 3.10).

Also, computational complexity can be a problem. For a high update rate, the multi-target detector has to run very fast to allow real-time operation.

Two methods of detecting multiple targets are presented. Both methods use successive target cancellation, one coherent, the other binary.

One aspect of target recognition commonly discussed in long-range radar systems (e.g. air traffic surveillance radars) is the separation of clutter and targets. In short-range radar systems, such as vehicular radar, there really is no distinction between clutter and valid targets, since any scattering object might also be a relevant target, e.g. an automobile parked by the roadside might be clutter for one application, but relevant for another. More importantly, there is no distinction between potential clutter and targets in the periodogram. Clutter analysis is therefore not a part of this section, and will be left to other sub-systems in practice.

Binary Successive Target Cancellation

This algorithm is the simplest, both in terms of computational complexity as well as memory requirement. It relies on the assumption that a window function with a high sidelobe attenuation is used, such that sidelobes are always attenuated below the threshold.

It requires a binary map $\mathbf{B} \in \{0, 1\}^{N_{\text{Per}} \times M_{\text{Per}}}$ with the same dimensions as the periodogram, which is used to track the position of previously identified targets. It also requires the size of the window's main lobe in number of bins for range (N_{win}) and Doppler (M_{win}).

The algorithm works as follows:

1. Initialize all elements of the binary map to one, $(\mathbf{B})_{k,l} = 1$, and an index value $i = 0$.
2. Find the largest peak

$$(\hat{n}_i, \hat{m}_i) = \arg \max_{n,m} \text{Per}_{\mathbf{F}}(n, m) \quad \text{s.t.} \quad (\mathbf{B})_{n,m} = 1$$

3. If $\text{Per}_{\mathbf{F}}(\hat{n}_i, \hat{m}_i) < \eta$, stop searching.
4. Identify range, Doppler and RCS of the i -th target through a suitable interpolation algorithm from (\hat{n}_i, \hat{m}_i) , e.g. quadratic interpolation, and add those to the list of targets.
5. Set

$$(\mathbf{B})_{k,l} = 0 \quad \forall k, l \quad \text{s.t.} \quad \frac{(k - \hat{n}_i)^2}{(\frac{N_{\text{win}}}{2})^2} - \frac{(l - \hat{m}_i)^2}{(\frac{M_{\text{win}}}{2})^2} \leq 1$$

6. Increment i
7. Continue at 2)

Fig. 3.13 shows an example for a periodogram with three targets, the estimator result as well as \mathbf{B} for iterations $i = 0$ and $i = 2$.

The major advantage of this algorithm is its simplicity. This comes at a cost: If the assumption that all sidelobes are attenuated below η is incorrect, the sidelobes *will* cause false detections. Furthermore, the window functions employed increase the resolution of the radar system.

Another disadvantage stems from the binary nature of the cancellation algorithm: When two targets lie very close together (on the order of the resolution), the peak of the weaker target may lie inside the main lobe of the stronger one. The maximum of $\text{Per}_{\mathbf{F}}(n, m)$ for which $(\mathbf{B})_{n,m} = 1$ may thus not be the true peak of the target. This can cause a target to be incorrectly identified as further away, and with a smaller RCS (see Fig. 3.13c).

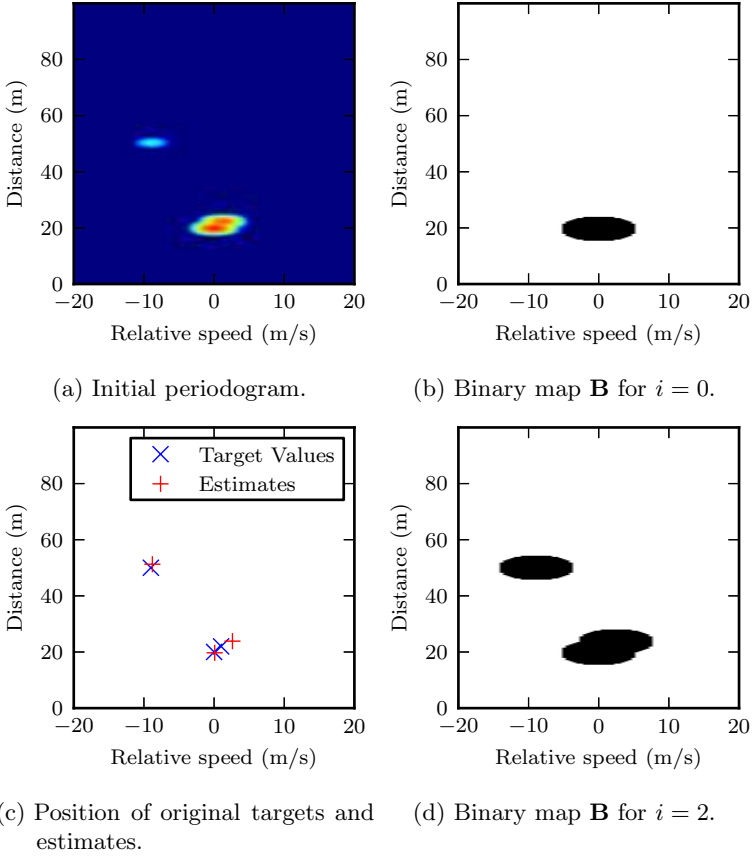


Figure 3.13: Target detection with the binary target cancellation algorithm (using a Dolph-Chebyshev window, $a_{\min} = 60$ dB)

Coherent Successive Target Cancellation

The disadvantages of the previous algorithm stem from the binary nature of the cancellation; once a bin is marked with zero in \mathbf{B} , it can't be used for other targets. This can be avoided by *coherently* cancelling out targets, as described in [9]. To achieve this, the algorithm must have access to both the periodogram and the complex periodogram. This is an iterative process, and as before, i shall be used to denote the current iteration, and $\text{Per}_{\mathbf{F},i}(n, m)$ shall denote the periodogram during the i -th iteration.

Unlike the previous algorithm, it successively removes targets from the periodogram, including their sidelobes. This makes it possible to use it even with a random sub-carrier selection. The algorithm consists of the following steps:

1. Initialize an iteration counter $i = 0$.
2. Find the largest peak

$$(\hat{n}_i, \hat{m}_i) = \arg \max_{n, m} \text{Per}_{\mathbf{F}}(n, m)$$

3. If $\text{Per}_{\mathbf{F}}(\hat{n}_i, \hat{m}_i) < \eta$, stop searching.
4. Check if the peak at $\text{Per}_{\mathbf{F}}(\hat{n}_i, \hat{m}_i)$ is caused by a *residual* or a target (see below).
5. If the peak describes a target, identify range, Doppler and RCS of the i -th target through a suitable interpolation algorithm from (\hat{n}_i, \hat{m}_i) , e.g. quadratic interpolation, and add those to the list of targets.
6. Calculate the radar processing matrix of this single target,

$$(\mathbf{F}_{\hat{n}_i, \hat{m}_i})_{k, l} = e^{j2\pi(l - \hat{m}_i) \frac{\hat{m}_i}{M_{\text{Per}}}} e^{j2\pi(k - \hat{n}_i) \frac{\hat{n}_i}{N_{\text{Per}}}}. \quad (3.99)$$

Using this, calculate the complex periodogram of $\mathbf{F}_{\hat{n}_i, \hat{m}_i}$,

$$\text{CPer}_{\mathbf{F}_{\hat{n}_i, \hat{m}_i}, i}(n, m) = \sum_{k=0}^{N_{\text{Per}}-1} \left(\sum_{l=0}^{M_{\text{Per}}-1} (\mathbf{F})_{k, l} e^{-j2\pi \frac{lm}{M_{\text{Per}}}} \right) e^{j2\pi \frac{kn}{N_{\text{Per}}}} \quad (3.100)$$

7. Subtract this from the original complex periodogram, using the complex amplitude at (\hat{n}_i, \hat{m}_i) :

$$\begin{aligned} \text{CPer}_{\mathbf{F},i+1}(n, m) &= \text{CPer}_{\mathbf{F},i+1}(n, m) - \\ &\quad \text{CPer}_{\mathbf{F},i+1}(\hat{n}_i, \hat{m}_i) \cdot \text{CPer}_{\mathbf{F}_{\hat{n}_i, \hat{m}_i, i}}(n, m). \end{aligned} \quad (3.101)$$

8. Update the real-valued periodogram,

$$\text{Per}_{\mathbf{F},i+1}(n, m) = \frac{1}{NM} |\text{CPer}_{\mathbf{F},i+1}(n, m)|^2. \quad (3.102)$$

9. Increment i

10. Continue at 2)

In every step, a single target is identified and its influence is removed from the periodogram, until only noise components remain.

One critical element is the identification of residuals, as mentioned in step 4). A residual may occur when the estimated position, phase or amplitude of the target's peak is incorrectly estimated, which is usually the case in a noisy environment.

Fig. 3.14 illustrates this effect for real, one-dimensional signals. The true periodogram is incorrectly estimated, with a slight offset in both amplitude as well as position. When subtracting the incorrect estimate from the true periodogram, the difference is still significant, with two significant peaks. If these peaks lie above η , they are a residual and will be detected eventually in step 2).

Even with an estimation error, the residual will always lie within the main lobe of the estimated periodogram, as the maximum-search always returns a point on the main lobe (see Section 3.3.5). A residual can therefore be identified as lying within a main lobe of a previously detected target.

To mitigate residuals, the estimation error must be minimized. For targets with a high SNR, this can be achieved by using the interpolated values $(\hat{\hat{n}}, \hat{\hat{m}})$ to calculate $\mathbf{F}_{\hat{\hat{n}}, \hat{\hat{m}}}$ and, consequently, $\text{CPer}_{\mathbf{F}_{\hat{\hat{n}}, \hat{\hat{m}}}, i}$. To calculate the latter, the interpolation algorithm must be extended to calculate an interpolated value for the amplitude and phase as well as the position, which cannot be achieved by the linear and quadratic interpolation

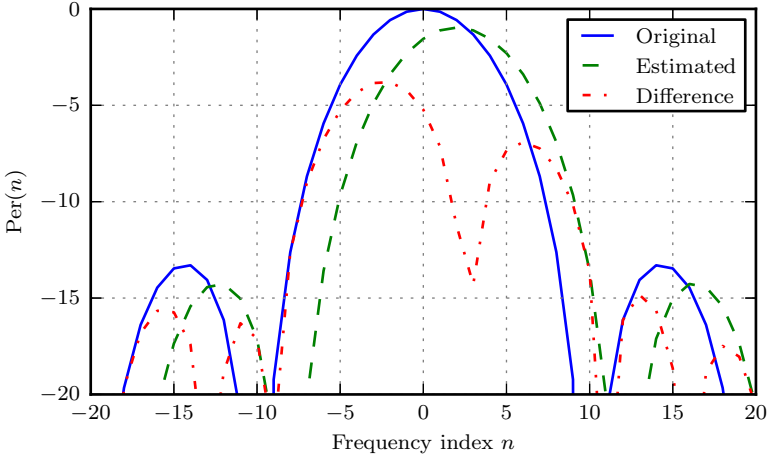


Figure 3.14: Real valued periodogram of a single target, an incorrect estimate thereof, and their difference

algorithms from Section 3.3.5 (the quadratic algorithm can interpolate the amplitude, but not the phase, whereas in the optimization algorithm, $CPer_{\hat{n}, \hat{m}, i}$ is calculated as an intermediate step in (3.89)).

The simplest way to reduce the effect of residuals is to increase the size of the periodogram $N_{Per} \times M_{Per}$ with additional zero-padding, although this increases the memory consumption and computational complexity. None of these efforts can completely remove the need to identify residuals, however, as noise will always cause an estimation error.

Because of the coherent subtraction from the periodogram between iterations, less information is destroyed per iteration when compared to the binary target cancellation. This makes the algorithm more suitable for a higher number of targets, with the increased computational effort being the only downside.

Also, as sidelobes are removed in every step, there is no requirement to use any other window than rectangular windows. In practice, a use of a window has sometimes proven beneficial as the reduced sidelobe levels prove to be more forgiving when incorrectly estimating a target in step

2).

Fig. 3.15 shows the result of the coherent cancellation algorithm for a scenario with four targets, showing some intermediary periodograms. In this simulation, the dimension of the periodogram was four times that of \mathbf{F} , $M_{\text{Per}} = 4M$, $N_{\text{Per}} = 4N$, and no interpolation was applied, which leads to slightly exaggerated residuals. They are correctly detected, however, and do not appear in the final list of estimated targets.

Coherent successive target cancellation is very similar to the CLEAN algorithm [59] which is often applied in radar. CLEAN factors in more problems, such as antenna positioning error, which is not relevant for the case of OFDM radar.

3.3.8 Non-contiguous sub-carrier allocations

Up until now, it was assumed that a contiguous range of N sub-carriers had been allocated. As already hinted in Section 3.1, this is only one possible way to configure an OFDM frame. This section will highlight three variants of sub-carrier allocations and discuss how they affect the radar processing.

Influence of the DC carrier

Most OFDM standards allocate a contiguous set of sub-carriers, leaving out the DC carrier, i.e. the carrier which is at 0 Hz in baseband. This avoids DC offset-related problems which typically occur in direct-conversion architectures.

This “missing” carrier causes problems for the radar component. To identify these, assume the window function for the columns \mathbf{w}_d is modified such that the centre tap is set to zero (see Fig. 3.16). Since the rows of \mathbf{F} are unaffected by this, it is possible to only analyze the effect in one dimension. How the DC carrier influences the OFDM radar can thus be expressed as the effect of this modified window on a sinusoid function in the periodogram.

To simplify the analysis and increase the readability, this following notation applies during this Section:

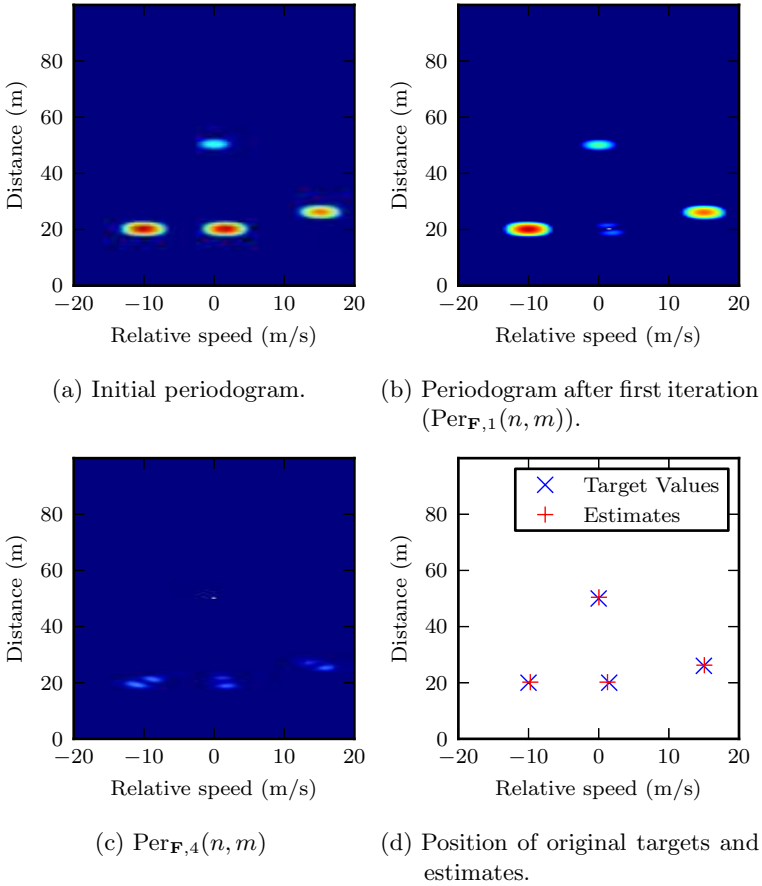


Figure 3.15: Target detection with the coherent target cancellation algorithm (using a Hamming window)

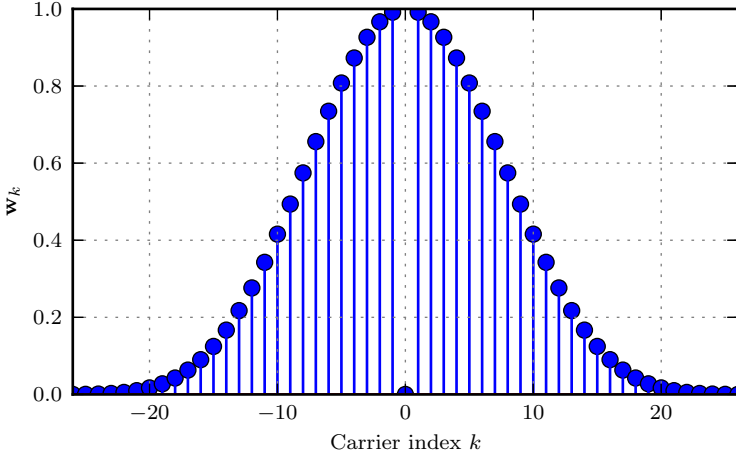


Figure 3.16: Modified Blackman-Harris window for an OFDM symbol with 52 active carriers. The centre carrier is nulled out.

- The carrier indices are rearranged such that the DC carrier has the index 0. The carrier indices therefore lie in the range $k = -\lfloor \frac{N}{2} \rfloor \dots \lfloor \frac{N}{2} \rfloor - 1$.
- The modified window is expressed as a discrete function $\tilde{w}(k)$.
- For sums, the following shorthand is defined:

$$\sum_k := \sum_{k=-\lfloor \frac{N}{2} \rfloor}^{\lfloor \frac{N}{2} \rfloor - 1} . \quad (3.103)$$

First, define the modified window function. If $w(k)$ is an unmodified window function (e.g. a Blackman-Harris window as shown in Fig. 3.16), then the modified function is given by

$$\tilde{w}(k) = w(k) - \delta(k)w(0). \quad (3.104)$$

The approximation $w(0) \approx 1$ is applied here (this is in fact an equality if N is odd for the window functions used here), which further simplifies

the modified window to

$$\tilde{w}(k) = w(k) - \delta(k). \quad (3.105)$$

The periodogram of a sinusoid with a normalised frequency $-0.5 \leq f < 0.5$ and phase φ

$$x(k) = e^{j2\pi f k} e^{j\varphi} \quad (3.106)$$

using (3.105) is thus

$$\begin{aligned} \tilde{\text{Per}}_{x(k)}(n) &= \frac{1}{N} \left| \sum_k \tilde{w}(k) x(k) e^{-j2\pi \frac{kn}{N_{\text{Per}}}} \right|^2 \\ &= \frac{1}{N} \left| \sum_k w(k) x(k) e^{-j2\pi \frac{kn}{N_{\text{Per}}}} - x(0) \right|^2. \end{aligned} \quad (3.107)$$

By using the identity $|a + b|^2 = |a|^2 + |b|^2 + 2 \text{Re}[ab^*]$, this is further modified to

$$\begin{aligned} \tilde{\text{Per}}_{x(k)}(n) &= \frac{1}{N} \left| \sum_k w(k) x(k) e^{-j2\pi \frac{kn}{N_{\text{Per}}}} \right|^2 + \frac{1}{N} |x(0)|^2 \\ &\quad - \frac{2}{N} \Re \left[x^*(0) \sum_k w(k) x(k) e^{-j2\pi \frac{kn}{N_{\text{Per}}}} \right]. \end{aligned} \quad (3.108)$$

The first summand is identical to the periodogram using the unmodified window; and $|x(0)|^2 = w(0)^2 = 1$. The third summand requires some closer scrutiny. By inserting (3.106), the term inside the real operator becomes

$$\begin{aligned} x^*(0) \sum_k w(k) x(k) e^{-j2\pi \frac{kn}{N_{\text{Per}}}} &= e^{-j\varphi} \sum_k w(k) e^{j2\pi k f} e^{j\varphi} e^{-j2\pi \frac{kn}{N_{\text{Per}}}} \\ &= \sum_k w(k) e^{-j2\pi k (\frac{kn}{N_{\text{Per}}} - f)}. \end{aligned} \quad (3.109)$$

It is identical to the discrete Fourier transform of the unmodified window, but shifted by the frequency of the sinusoid.

Finally, by taking the real part, this becomes

$$\Re \left[x^*(0) \sum_k w(k) x(k) e^{-j2\pi \frac{kn}{N_{\text{Per}}}} \right] = \sum_k w(k) \cos\left(2\pi k \left(f - \frac{kn}{N_{\text{Per}}}\right)\right), \quad (3.110)$$

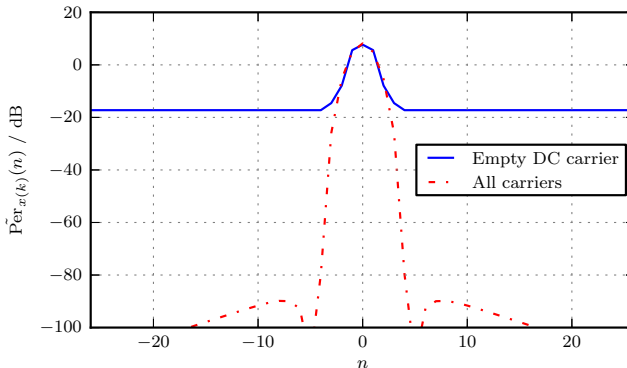


Figure 3.17: Periodogram with full set of carriers and an empty DC carrier.

and therefore the modified periodogram is

$$\begin{aligned} \tilde{\text{Per}}_{x(k)}(n) &= \frac{1}{N} \left| \underbrace{\sum_k w(k)x(k)e^{-j2\pi\frac{kn}{N_{\text{Per}}}}}_{\text{Unmodified periodogram}} \right|^2 \\ &+ \underbrace{\frac{1}{N} - \left(\frac{2}{N} \sum_k w(k) \cos\left(2\pi k\left(f - \frac{n}{N_{\text{Per}}}\right)\right) \right)}_{\text{Spur term}}. \end{aligned} \quad (3.111)$$

Two effects are noteworthy, depending on the position in the periodogram. Near the frequency of the sinusoid, the $\cos(\cdot)$ function in the spur term is of unit value, and the spur term itself is negative:

$$\frac{1}{N} \left(1 - \sum_k w(k)\right) < 0. \quad (3.112)$$

In Fig. 3.17 it can be seen that shape of the periodogram is largely unaffected in this region, only the maximum value is reduced by a small amount. This is to be expected, since the modified window removes energy from the sinusoid. However, a far worse effect is visible for frequencies far from the sinusoid's, where a constant spur floor is evident.

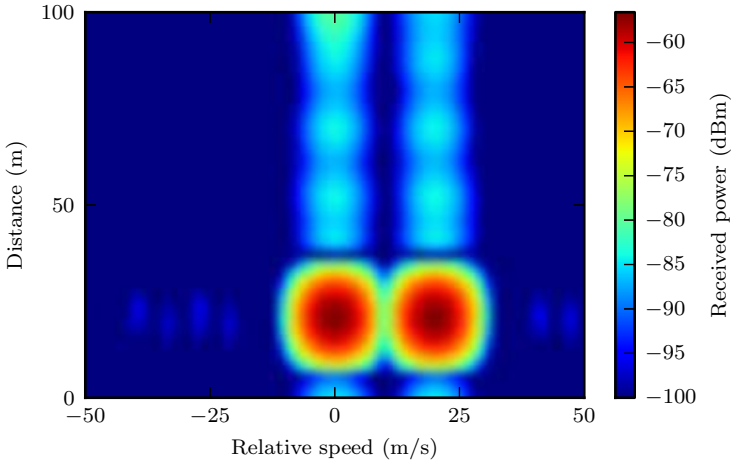


Figure 3.18: Two targets at 10 m are clearly visible; a third target at 100 m and zero Doppler can be barely distinguished from the spur floor from the closer target.

The sum in the spur term is a sum over one period of a cosine, and thus approximately zero, leaving the constant term $1/N$. As the unmodified periodogram drops to its sidelobe attenuation, the modified periodogram is kept at a minimum value of $1/N$. The peak-to-spur ratio¹² (PSR) is exactly the peak periodogram value of the modified window,

$$\text{PSR} = \left| \sum_k \tilde{w}(k) \right|^2. \quad (3.113)$$

For the radar, this means a loss of dynamic range. If two targets with the same Doppler shift are present, the difference of their respective backscattered energies cannot be larger than the PSR if both are to be detected. Fig. 3.18 illustrates this problem in the 2D periodogram. Also, the detection threshold must be adapted once a target was detected such that it is always higher than the spur floor.

¹²For a Hamming window and the carrier setup of IEEE 802.11a, PSR is approx. 27 dB. This was first observed (but not explained) by Falcone et al. [38].

To solve this problem, one solution is to simply use every second sub-carrier as in Section 3.3.8 and configure the system such that the centre carrier is left unused. If the signal parametrization is fixed (e.g. because a IEEE 802.11a system is used as a transmitter), this means ignoring half of the transmitted energy. However, losing 3 dB of dynamic range due to half the transmit power is still superior to fixing the dynamic range to the PSR.

Regular sub-carrier spacing at larger intervals

In section 3.1, it was discussed that the sub-carrier distance must be the reciprocal value of the OFDM symbol time to ensure orthogonality between carriers. Of course, this is also the case if the sub-carrier distance is an integer multiple of the inverse OFDM symbol duration, $\Delta f = U/T, U \in \mathbb{N}$.

Using a larger sub-carrier distance is equivalent to only allocating every U -th sub-carrier, leaving the others idle. Note that this does not affect the bandwidth (and hence the range resolution), but increasing Δf by a factor U will decrease the unambiguous range in (3.25) by the same factor,

$$d_{\text{unamb}} = \frac{c_0}{2U\Delta f}. \quad (3.114)$$

Also, the number of active sub-carriers is decreased which results in a higher transmit power per sub-carrier. While this does increase the signal-to-noise ratio at the receiver on each sub-carrier, the processing gain is reduced in the same manner, thereby resulting in the same SNR in the periodogram.

To summarize, a regular sub-carrier spacing only modifies the unambiguous range, the total received energy stays the same, as well as the resulting periodogram.

One reason to choose a higher sub-carrier spacing is the possibility to create multiple, orthogonal channels. If only every U -th sub-carrier is allocated, this results in U orthogonal sets of sub-carriers, which can be used by different sub-carriers. This method was first described in [18] and more elaborately in [21].

On a side note, this method can be used to avoid the problem of allocating the DC carrier by simply not using that particular set of sub-carriers.

Random sub-carrier allocations

The previous method states that up to U users can access the medium at the same time, but does not elaborate on how the users decide which sub-carrier set to transmit on. In an ad-hoc scenario, there is no guarantee that two users will not use the same channel, thereby causing mutual interference. Of course, if more than U transmissions are active, interference is guaranteed – but it is not distributed fairly among the users, as would be desirable.

A method to achieve a fair distribution of interference is to randomly select $K = N/U$ carriers for transmission, leaving the rest of them idle [11, 139]. On the radar side, such a system is simple to implement: Prior to transmission, an active carrier list \mathbf{N} is generated by randomly selecting K values from the range of total carriers, $\mathbf{N} \in \{0, \dots, N - 1\}^K$. The transmit matrix then has the following form:

$$(\mathbf{F}_{\text{Tx}})_{k,l} = \begin{cases} \sqrt{U}c_{k,l} & \text{if } k \in \mathbf{N} \\ 0 & \text{otherwise.} \end{cases} \quad (3.115)$$

Only the randomly selected sub-carriers are utilized, the rest are initialized with zeros (as in the previous section, the amplitude of the carriers utilized is increased by \sqrt{U} to achieve the same total transmit power).

The radar processing as described in Section 3.3 is unaffected by the fact that some sub-carriers are idle, only the division (3.19) needs to be adapted to avoid a division by zero,

$$(\mathbf{F})_{k,l} = \begin{cases} \frac{(\mathbf{F}_{\text{Rx}})_{k,l}}{(\mathbf{F}_{\text{Tx}})_{k,l}} & \text{if } k \in \mathbf{N} \\ 0 & \text{otherwise.} \end{cases} \quad (3.116)$$

This affects the estimation of the number of sinusoids and their frequencies: They now have to be estimated from a set of *non-regularly sampled* data.

Spectral analysis of irregularly sampled data is a topic of its own, but a number of solutions have been found for this problem, such as the linear and non-linear least squares algorithms [91, 92, 139]. Unfortunately, these require knowledge on the number of targets, which is usually unknown in radar processing.

A method which does not have this problem and is also efficiently calculable is the periodogram. For one-dimensional signals $x(t)$ sampled at times t_k it is defined as

$$\text{Per}_{x(t_k)}(\omega_n) = \frac{1}{K} \left| \sum_{k=0}^{K-1} x(t_k) e^{-j\omega_n t_k} \right|^2. \quad (3.117)$$

If the sampling times are chosen from a regular grid, and the signal is set to zero at all other times,

$$x(k) = \begin{cases} x(t_k = kT_S) & \text{if } k \in \mathbf{N} \\ 0 & \text{otherwise,} \end{cases} \quad (3.118)$$

the discrete periodogram has nearly the same form as for the regular sampled case:

$$\text{Per}_{x(k)}(n) = \frac{1}{K} \left| \sum_{k=0}^{N-1} x(k) e^{-j2\pi \frac{kn}{N}} \right|^2, \quad (3.119)$$

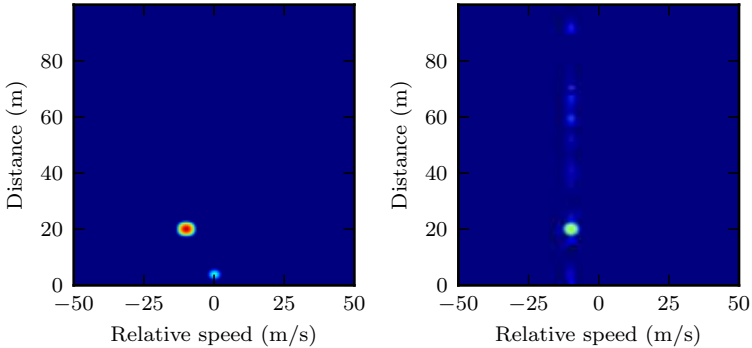
the only difference being the normalization factor.

As the radar processing matrix (3.21) represents a regular grid (the sub-carrier spacing) with the idle sub-carriers set to zero, this means that extending the periodogram to an irregular sub-carrier selection is done in the same manner as for the regular sub-carrier case,

$$\text{Per}_{\mathbf{F}}(n, m) = \frac{1}{KM} \left| \sum_{k=0}^{N_{\text{Per}}-1} \left(\sum_{l=0}^{M_{\text{Per}}-1} (\mathbf{F})_{k,l} e^{-j2\pi \frac{lm}{M_{\text{Per}}}} \right) e^{j2\pi \frac{kn}{N_{\text{Per}}}} \right|^2. \quad (3.120)$$

Most importantly, the efficient FFT-based processing is still valid.

Fig. 3.19 shows two periodograms from a simulated radar measurement using regular and irregular sub-carrier selection, respectively. One can see while the latter does not suffer from a reduction of unambiguous



(a) Regular sub-carrier spacing. An alias target can be seen at 4 m.
 (b) Random sub-carrier spacing. Spurs appear at the same Doppler throughout the detection range.

Figure 3.19: Scenario with a close target at 20 m and a far target with large RCS at 210 m.

range (there are no alias targets), it does exhibit elevated spur levels next to existing targets, similar to those in Fig. 3.18. Unlike with the missing DC carrier, the exact shape of the spur floors is random as it depends on the choice of \mathbf{N} . Such spurs prohibit the use of the binary target cancellation algorithm for multi-target scenarios.

Using a random sub-carrier allocation has one major advantage over the regular sub-carrier variant: If a specific sub-carrier is overlaid with strong interference, it may be discarded a-posteriori. This does decrease the total received power, but might increase the signal-to-interference ratio after the radar processing.

The disadvantages go beyond the increased spur level. On the communication side, the receiver has to detect the allocated sub-carriers, which puts additional burden on the synchronisation, equalization and demodulation.

Also, as will be discussed in Chapter 4, the interference caused by simultaneous access to the medium is not necessarily a problem for the radar system, as long as the density of the interfering transmitters is not too high.

These considerations make the random carrier allocation an interesting academic problem, but of little practical use.

3.4 Parametric target estimation

The periodogram is the most common non-parametric tool in spectral estimation, which also makes it a versatile tool for OFDM radar processing. However, the radar estimation problem is a very specific subset of spectral estimation, and can therefore also be solved by parametric methods.

Consider of the radar processing matrix (3.21):

$$(\mathbf{F})_{k,l} = \sum_{h=0}^{H-1} b_h e^{j2\pi l T_O f_{D,h}} e^{-j2\pi k \tau_h \Delta f} e^{j\varphi_h} + (\mathbf{Z})_{k,l}. \quad (3.121)$$

Since this matrix is known in its entirety (albeit with a random noise component), the question arises if there is a way to directly estimate the parameters $f_{D,h}$, τ_h , b_h and H . The solution is to adapt parametric estimators for one-dimensional sinusoid estimation.

Out of the existing estimators, the ESPRIT algorithm was deemed the most suitable for OFDM radar [123]. Other estimators were also considered for further analysis, but later discarded for different reasons: The Burg algorithm [102] and the High-Order Yule-Walker method [86] are not optimized for line spectra, as they estimate rational spectra, and the non-linear least-squares algorithm was deemed computationally too complex.

3.4.1 ESPRIT

The ESPRIT¹³ algorithm, first presented 1986 by Roy and Kailath [95] is a subspace-based method for the estimation of line spectra, and therefore a valid choice for the application in OFDM radar. A very similar method, MUSIC,¹⁴ was first applied to OFDM radar in [6]. ESPRIT

¹³ *Estimation of Signal Parameters via Rotational Invariance Techniques*

¹⁴ *Multiple Signal Classification*

often outperforms MUSIC both in accuracy [86, Chap. 4.7] and computational cost [134] and is therefore the preferred choice.

A comprehensive description of ESPRIT can be found in [86]. Only the most relevant steps are recapitulated here.

Let $x(k) = \sum_{h=0}^{H-1} b_h e^{j(\omega_h k + \varphi_h)} + z(k)$ be a superposition of H sinusoids with unknown phase, frequency, and amplitude as well as a white Gaussian noise process $z(k)$. If $\mathbf{x} \in \mathbb{C}^{1 \times N}$ is a vector representing the time-domain signal, $\mathbf{R}_{\mathbf{xx}} \in \mathbb{C}^{N \times N}$ is the auto-covariance matrix of $x(k)$, which can be decomposed into its eigenvalues and -vectors,

$$\mathbf{R}_{\mathbf{xx}} = \mathbf{U} \mathbf{\Lambda} \mathbf{U}^* \quad , \quad \mathbf{\Lambda} = \text{diag}(\lambda_0, \lambda_1, \dots, \lambda_{N-1}). \quad (3.122)$$

If the eigenvalues are sorted by size ($\lambda_i < \lambda_{i+1}, i = 0, \dots, N-1$), the first H columns of \mathbf{U} (i.e. the eigenvectors corresponding to the largest eigenvalues) span the *signal subspace* of $x(k)$, and the remaining $N-H$ eigenvectors span the noise subspace,

$$\mathbf{U} = [\mathbf{S} \quad \mathbf{G}] \quad , \quad \mathbf{S} \in \mathbb{C}^{N \times H}, \mathbf{G} \in \mathbb{C}^{N \times (N-H)} \quad (3.123)$$

The noise subspace is of no interest for this estimator. The signal subspace is used to create two new matrices,

$$\mathbf{S}_1 = [I_{N-1} \quad \mathbf{0}] \mathbf{S} \quad (3.124)$$

$$\mathbf{S}_2 = [\mathbf{0} \quad I_{N-1}] \mathbf{S} \quad (3.125)$$

These are in turn used to create

$$\mathbf{\Phi} = (\mathbf{S}_2^* \mathbf{S}_2)^{-1} \mathbf{S}_2^* \mathbf{S}_1. \quad (3.126)$$

It can be shown that $\mathbf{\Phi} = \mathbf{C}^{-1} \mathbf{D} \mathbf{C}$, where \mathbf{C} is a nonsingular matrix and $\mathbf{D} = \text{diag}(e^{-j\omega_0}, \dots, e^{-j\omega_{N-1}})$. The eigenvalues of $\mathbf{\Phi}$ can therefore be used to estimate the frequencies in $x(k)$, $\hat{\omega}_k = -\arg[\lambda_k]$.

Estimation of the auto-covariance matrix

ESPRIT requires the auto-covariance matrix $\mathbf{R}_{\mathbf{x}\mathbf{x}}$ as input, whereas a digital receiver only provides the time-domain signal \mathbf{x} . The definition of the auto-covariance matrix is

$$\mathbf{R}_{\mathbf{x}\mathbf{x}} = \mathbb{E}[\mathbf{x}^* \mathbf{x}]. \quad (3.127)$$

To estimate the auto-covariance matrix, L independent representations of \mathbf{x} are required. Because the noise component in \mathbf{x} is white Gaussian noise (WGN), the maximum likelihood estimate for the auto-covariance matrix is [86]

$$\hat{\mathbf{R}}_{\mathbf{x}\mathbf{x}} = \frac{1}{M} \sum_{i=0}^{L-1} \mathbf{x}_i^* \mathbf{x}_i. \quad (3.128)$$

Application to OFDM radar

As discussed, there will be two one-dimensional estimation problems to solve. For ESPRIT, this requires two auto-covariance matrices, for range and Doppler, respectively.

Given the radar processing matrix \mathbf{F} , this is achieved quite simply. Since the column-wise oscillations correspond to the range of the individual targets, and every row is a representation of the same process, the auto-covariance matrix is estimated by

$$\hat{\mathbf{R}}_{\mathbf{F}\mathbf{F},d} = \frac{1}{N} \mathbf{F}\mathbf{F}^* \in \mathbb{C}^{N \times N}. \quad (3.129)$$

In an analog fashion, the auto-covariance matrix for the row-wise oscillations (corresponding to the Doppler, or relative velocity) are calculated:

$$\hat{\mathbf{R}}_{\mathbf{F}\mathbf{F},v_{\text{rel}}} = \frac{1}{M} \mathbf{F}^* \mathbf{F} \in \mathbb{C}^{M \times M}. \quad (3.130)$$

The algorithm to determine Doppler and range of targets from \mathbf{F} using the ESPRIT algorithm is thus straightforward:

1. Calculate $\hat{\mathbf{R}}_{\mathbf{F}\mathbf{F},d}$ from \mathbf{F} as shown in (3.129).
2. Using (3.122) through (3.126), calculate the matrix Φ_d .

3. For every one of the P (this value is discussed in Section 3.4.2) largest eigenvalues of Φ_d , the range of the object is calculated by

$$\hat{d}_i = -\arg\left[\hat{\lambda}_i\right] \cdot \frac{c_0}{2\pi \cdot 2U\Delta f}, \quad i = 0, \dots, P-1 \quad (3.131)$$

similarly to the way d is estimated from the periodogram in (3.32). U is the optional sub-carrier spacing explained in Section 3.3.8.

4. Analogously, calculate $\hat{\mathbf{R}}_{\mathbf{FF},v_{\text{rel}}}$ from (3.130).
5. Compute a new matrix $\Phi_{v_{\text{rel}}}$ from $\hat{\mathbf{R}}_{\mathbf{FF},v_{\text{rel}}}$.
6. The eigenvalues $\hat{\lambda}_i$ of $\Phi_{v_{\text{rel}}}$ can then be used to calculate the relative velocities of the objects,

$$\hat{v}_{\text{rel},i} = -\arg\left[\hat{\lambda}_i\right] \cdot \frac{c_0}{2\pi \cdot 2U\Delta f}. \quad (3.132)$$

Dimensionality reduction of the auto-covariance matrices

The computational bottleneck in the ESPRIT is the eigenvalue decomposition of the auto-covariance matrices. Decreasing the dimension of the auto-covariance matrices will also decrease the computational complexity [3]. For the range estimation, this is easily achieved by splitting \mathbf{F} vertically into K sub-matrices,

$$\mathbf{F} = \begin{bmatrix} \mathbf{F}_0 \\ \mathbf{F}_1 \\ \vdots \\ \mathbf{F}_{K-1} \end{bmatrix}, \quad (3.133)$$

where each sub-matrix has the dimension $\mathbf{F}_i \in \mathbb{C}^{\frac{N}{K} \times M}$. The auto-covariance for the range estimation is then the average of the auto-covariance matrices of the sub-matrices,

$$\hat{\mathbf{R}}_{\mathbf{FF},d} = \frac{1}{N} \sum_{i=0}^{K-1} \mathbf{F}_i^* \mathbf{F}_i \in \mathbb{C}^{\frac{N}{K} \times \frac{N}{K}}. \quad (3.134)$$

Analogously, the auto-covariance matrix for the Doppler estimation is obtained by splitting \mathbf{F} *horizontally* into sub-matrices, and averaging

their auto-covariance matrices

$$\hat{\mathbf{R}}_{\mathbf{F}\mathbf{F},d} = \frac{1}{N} \sum_{i=0}^{K-1} \mathbf{F}_i^* \mathbf{F}_i \in \mathbb{C}^{\frac{N}{K} \times \frac{N}{K}}. \quad (3.135)$$

These auto-covariance matrices with reduced dimension can be used in exactly the same fashion as before.

3.4.2 Comparison to periodogram-based processing

The advantage of the ESPRIT algorithm is its simplicity: To acquire the estimates from the matrix \mathbf{F} , only a few algebraic operations are required. No target detection algorithms are necessary. Also, ESPRIT does not suffer from quantization issues and therefore does not need the interpolation algorithms described in Section 3.3.5.

However, it has three major disadvantages over the periodogram: First, the estimation order P is required as an input to the estimator, although the number of targets might not be known a-priori. It is possible to over-estimate P , but that results in additional estimates, which do not correspond to existing targets.¹⁵ Second, the list of values for the range and Doppler estimates are not linked—it is not clear which range estimate corresponds to which Doppler estimate.

Gansman et al. [96] have described a method to perform a coupled estimation using two-dimensional ESPRIT algorithm, but that makes assumptions towards the matrix \mathbf{F} which are not generally fulfilled for radar, e.g. that no two objects have the same distance or velocity.

If there are only a few targets with large difference in backscattered power, there is a high probability that the order of the target's eigenvalues is most likely the same for both estimates, and sorting the eigenvalues by amplitude can solve this problem (i.e. the estimate for range corresponding to the largest eigenvalue of $\hat{\mathbf{R}}_{\mathbf{F}\mathbf{F},d}$ and the estimate for velocity corresponding to the largest eigenvalue of $\hat{\mathbf{R}}_{\mathbf{F}\mathbf{F},\mathbf{v}_{\text{rel}}}$ belong to the same target). However, this is not a reliable method. If ESPRIT is to be used

¹⁵Preliminary research was done to combine the periodogram and ESPRIT algorithms [136], but very little benefit was found of adding the ESPRIT algorithm after the periodogram, see also 5.2.

for two-dimensional estimation in the same way as the periodogram, additional heuristics must be implemented to create a useful radar estimate. In any case, this method only works for a very small number of targets.

The third disadvantage is the required SNR. ESPRIT-based estimators require a better SNR than the periodogram (cf. [6] and the results in Section 5.2.1). This can be explained with the matched filter analogy of the periodogram (Section 3.3.3), which suggests that the periodogram is the optimal estimator with regard to SNR.

For practical use, the disadvantages outweigh the advantages. Unless the application is very specific, such as the tracking of a single object in an otherwise uncluttered environment, the robustness and versatility of the periodogram make it the better choice for OFDM radar signal processing.

3.5 Non-spectral estimation based algorithms

All estimation techniques presented make use of the sinusoidal form of \mathbf{F} , i.e. the fact that target detection is turned into a sinusoidal detection problem.

Other possible methods of performing radar estimation have also been suggested. One way to obtain a radar image is to cross-correlate the received signal with the transmitted signal both in time and frequency, such as discussed in [37]. The resulting two-dimensional cross-correlation function is then further subjected to a peak detector in the same way as the periodogram to determine the number of peaks as well as their corresponding range and Doppler.

A detailed comparison of this method with the periodogram method is given in [18, Chap. 3]. The two biggest disadvantages of the cross-correlation are the increased computational complexity and the lower peak-to-spur ratio. The former is due to the fact that the efficient FFT-based algorithm for the periodogram presented in Section 3.3 cannot be as effectively applied to the two-dimensional cross-correlation. The increased spur levels are caused by the structure of the transmitted data, which cause additional peaks in the auto-correlation function of the time-domain OFDM signal. These are not a problem if the transmit symbols are removed a-priori, as in (3.19). Algorithms have been developed

to remove these spurs [38], but this only increases the computational cost. To summarize, the correlation method does not make efficient use of the OFDM signal structure and is thus inferior to the periodogram method.

A different approach to perform OFDM radar was described in [36], one of the earliest publications suggesting to use OFDM for a combination of radar and communications. The paper describes a MIMO radar system which uses a very specific encoding of the OFDM frames. This encoding severely reduces the maximum achievable data rate and makes such a system incompatible with existing OFDM communication standards. Also, not all OFDM sub-carriers are used for radar processing, thereby reducing the total SNR. As with the correlation method, this type of radar processing was therefore not further considered for this work.

3.6 Signal Parametrization

An open question is that of the signal parametrization. For the most part of this work, the actual parameter values were irrelevant, but for an implementation, choices for the signal parameters (listed in Table 3.1) must be made.

OFDM signal specifications for joint communications and radar are constrained by a large number of factors, as first discussed in [1] and later in [5] ([18] also discusses the parameter requirements for a specific radar system, without the communication requirements). Both subsystems have their own requirements towards the signal parameters, which suggests that signals optimized only for communications (as most OFDM signals used in current systems are) might not also be suitable for radar.

As will be shown in the following, there is not *one* optimal parametrization. Instead, a comprehensive list of constraints for the individual parameters is presented in Section 3.6.1. Within those constraints, any parametrization can then be chosen. This degree of freedom allows the developer to choose a set of parameters which can be implemented efficiently.

Section 3.6.2 then gives examples of how a specific parametrization is chosen. Also, OFDM signals used by current standards are analysed for their radar performance.

Where relevant, the assumption is that the periodogram-based estimator is used.

3.6.1 Constraints and Requirements

Radar Requirements

The first and foremost requirement a short- or medium range radar system has is that of *resolution*, i.e. the capability of distinguishing close targets. The periodogram method can separate objects both in range and Doppler, which means the resolution needs to be established in both dimensions.

Let Δd be the range resolution, i.e. the minimum distance two objects with the same relative velocity may have that can still be distinguished. It is inversely proportional to the bandwidth [98],

$$\Delta d = \frac{c_0}{2N\Delta f}. \quad (3.136)$$

Given a maximum tolerable resolution Δd_{\max} , this constrains the bandwidth to

$$N\Delta f \geq \frac{c_0}{2\Delta d_{\max}}. \quad (3.137)$$

In an analog fashion, the velocity resolution Δv_{rel} is inversely proportional to the frame duration,

$$\Delta v_{\text{rel}} = \frac{c_0}{2MT_O f_C}. \quad (3.138)$$

Given a maximum tolerable velocity resolution $\Delta v_{\text{rel},\max}$, the minimum frame duration is given by

$$MT_O \geq \frac{c_0}{2\Delta v_{\text{rel},\max} f_C}. \quad (3.139)$$

Note that because the Doppler shift is proportional to the target's relative velocity *and* the signal's centre frequency, the minimum frame duration can be decreased by increasing either f_C or MT_O .

Another requirement (as already mentioned in Section 3.2.1) is to preserve orthogonality of the modulation symbols. To preserve orthogonality in time, the guard time T_G must be larger than the time delay caused

by the furthest target to be detected. If the maximum detection range is d_{\max} , the guard interval is bounded by

$$T_G \geq \frac{2d_{\max}}{c_0}. \quad (3.140)$$

In frequency, exact orthogonality is impossible for non-zero Doppler shifts. However, a large sub-carrier distance heavily alleviates the de-orthogonalizing effect of a frequency offset. Therefore, it must be ensured that Δf is larger than the Doppler shift caused by the object with the maximum relative velocity $v_{\text{rel,max}}$,

$$\Delta f \gg \frac{2v_{\text{rel,max}}}{c_0} f_C. \quad (3.141)$$

The maximum distance and relative velocity, d_{\max} and $v_{\text{rel,max}}$, of the targets also limits the unambiguous ranges as described in Section 3.2.2. For reliable radar operation, $d_{\max} \leq d_{\text{unamb}}$ and $v_{\text{rel,max}} \leq v_{\text{rel,unamb}}$ must be met and therefore

$$\Delta f \leq \frac{c_0}{2U d_{\max}} \quad (3.142)$$

$$T_O \leq \frac{c_0}{2f_C v_{\text{max,rel}}} \quad (3.143)$$

Typically, these are the weakest constraints and are usually met implicitly when the other requirements are fulfilled.

Communication Requirements

On the communications side, the main restrictions are imposed by the characteristics of the wave propagation channel.¹⁶

When one node is transmitting to another, the transmit signal $s(t)$ is convolved with a time-variant fading channel impulse response function $h(t, \tau)$.

Within a given multipath propagation channel, the signal parametrization must be chosen such that there is neither interference between consecutive OFDM symbols (Inter-Symbol Interference (ISI)) nor between

¹⁶Multipath propagation can also affect the radar sub-component, albeit the target detection rather than the signal parametrization.

adjacent sub-carriers (Inter-Carrier Interference (ICI)). Another aspect is the complexity of demodulation. OFDM typically uses single-tap equalizers, where the modulation symbols received are multiplied with complex scalars. For this to work, the channel must be approximately flat within several OFDM symbols and sub-carriers, respectively [103, Chap. 5].

The theory of mobile propagation channels is a complex topic, and will not be discussed in detail here. A thorough description of channels is found in [109] and [110]; [103] also discusses the effects of channels on OFDM in particular. Here, the following characteristics of propagation channels are sufficient:

- The maximum excess delay τ_e . Radio waves usually reach the receiver on a variety of paths, and arrive at different times. The time difference between the first and the last arrival of the same wave is described by τ_e .
- The Doppler spread B_D . This describes the widening of the spectrum, caused by different Doppler shifts on each multipath. It is inversely proportional to the coherence time T_C , which is the time over which the channel may be assumed constant.
- A similar metric to τ_e is the delay spread τ_{DS} , which is an *average* value for the time difference of multipath propagation times. Paths are weighted by their attenuation, meaning that paths carrying more energy contribute more to τ_{DS} than paths with large fading. The delay spread is inversely proportional to the *coherence bandwidth* B_C , which is the bandwidth over which a channel may be considered flat.

It must be emphasized that channels are not deterministic, and rarely static. The characteristics listed above are therefore *expected* values, derived from random channels.

ISI can simply be avoided by choosing the guard interval larger than the maximum excess delay of the channel,

$$T_G > \tau_e, \quad (3.144)$$

i.e. the time difference between the arrival of the first and the last multipath signal.

The sub-carrier spacing is restricted by several factors. To avoid ICI, it is important that the sub-carrier spacing is chosen larger than the Doppler spread. However, to make sure that adjacent carriers from one OFDM symbol experience similar fading coefficients, Δf must also be smaller than the coherence bandwidth of the channel,

$$B_D \ll \Delta f \ll B_C. \quad (3.145)$$

Similarly, the symbol duration T must be smaller than the coherence time T_C of the channel. Because $T = 1/\Delta f$, this can be formed into another constraint for Δf :

$$\Delta f > \frac{1}{T_C}. \quad (3.146)$$

Note that as $B_D \propto 1/T_C$, this is already implicitly stated in (3.145).

Technical and Regulatory Constraints

When implementing a system designed for commercial application, there are limits given by the law and the available technical capabilities. In particular, the available bandwidth B , the choice of centre frequency f_C and the maximum transmit power P_{\max} are restricted.

In general, the regulator is more restrictive than the available technical possibilities. However, if cost also becomes a factor, this might be different. After all, OFDM radar systems perform all signal processing in the digital, discrete-time domain and therefore need to be able to down-convert and digitize high-bandwidth signals with sufficient precision.

One figure of merit entirely dependant on the available hardware is the noise figure NF. Together with the bandwidth, it defines the noise power (see also Section 3.3.1)

$$P_N = \text{NF} \cdot k_B \vartheta N \Delta f. \quad (3.147)$$

When P_{\max} , P_N , f_C , and B are given, this already limits both the radar and communication subsystems (ϑ is the noise temperature). Section 3.3.6 showed that the minimum SNR required to detect a target is $\text{SNR}_{\min} = P_{\text{Rx}}/P_N = \ln(1 - \sqrt[N]{1 - p_{\text{FA}}})$. The radar range equation

relates this value to the maximum distance for which targets can be detected [98],

$$\text{SNR}_{\min} = \frac{P_{\text{Rx}}}{P_N} \quad (3.148)$$

$$= \frac{P_{\max} G_{\text{Rxc}} c_0^2 \sigma_{\text{RCS}} N M}{(4\pi)^3 f_C^2 P_N d_{\max}^4}. \quad (3.149)$$

This can be solved for d_{\max} ,

$$d_{\max, \text{detect}} = \sqrt[4]{\frac{P_{\max} G_{\text{Rxc}} c_0^2 \sigma_{\text{RCS}} \cdot N M}{(4\pi)^3 f_C^2 P_N \cdot \text{SNR}_{\min}}} \quad (3.150)$$

In practice, d_{\max} can be even smaller due to effects not covered by the radar range equation, such as close targets overshadowing the desired target.

Transmit power and bandwidth also concern the data transmission. Using the free space path loss equation, a receiver with distance d_{comm} from the transmitter will receive a total power of

$$P_{\text{comm}} = \frac{P_{\max} c_0^2 G_{\text{Rx}}}{(4\pi)^2 f_C^2 d_{\text{comm}}^2}. \quad (3.151)$$

On each sub-carrier, the modulation symbol energy per noise power density $\frac{E_S}{N_0}$ is thus

$$\frac{E_S}{N_0} = \frac{\frac{P_{\text{comm}} T}{N}}{k_B \vartheta \cdot \text{NF}} = \frac{P_{\max} c_0^2 T}{(4\pi)^3 k_B \vartheta \cdot \text{NF} \cdot f_C^2 d_{\text{comm}}^2} \quad (3.152)$$

When choosing a modulation alphabet, it must be ensured that the E_b/N_0 is large enough. As an example, assume that every modulation symbol shall represent one bit using BPSK modulation. In this case, both $E_b/N_0 = E_S/N_0$ and (3.152) are used to assess whether the E_b/N_0 is large enough for a target bit error rate.

3.6.2 Examples for parameter sets

To illuminate the thought process behind the parametrization, two examples of OFDM radar parametrizations are discussed: One optimized for OFDM radar, and one common OFDM standard not optimized for radar.

Radar Specifications	
Range resolution Δd_{\max}	2 m
Velocity resolution $\Delta v_{\text{rel},\max}$	2 m/s
Maximum detection range d_{\max}	200 m
Maximum relative velocity $v_{\text{rel},\max}$	200 km/h = 55.6 m/s
False alarm rate p_{FA}	0.1
Receive gain G_{R_x}	15.6 dBi
Communication Specifications	
Minimum bit rate R	100 kbps
Communication range d_{comm}	400 m
Hardware Specifications	
Transmit power P_{\max}	0.1 W = 20 dBm
Noise figure NF	5 dB
Suggested Parameters	
Sub-carrier spacing Δf	90.9 kHz
Symbol duration $T = 1/\Delta f$	11 μ s
Number of carriers N	1024
Number of OFDM symbols M	256
Guard time T_G	$1/8T = 1.375 \mu$ s

Table 3.4: Possible specifications for an OFDM radar

24 GHz ISM-band radar

In [18], a parametrization was suggested for the 24 GHz ISM band, with the intended application of inter-vehicular radar and communication, and its suitability for OFDM radar was discussed. To show that the parameters are also suitable for communication, the derivation of parameters from [18, Chap. 3] is reproduced, albeit with additional constraints.

Radar Requirements Table 3.4 shows the specifications of the radar system. Where relevant, these were chosen to be congruous to [18]. Beginning with the radar requirements, the minimum bandwidth is

$$c_0/(2\Delta d_{\max}) = 75 \text{ MHz}$$

and the minimum frame duration is

$$c_0/(2\Delta v_{rel,max}f_C) = 3.125 \text{ ms.}$$

To satisfy (3.141), the sub-carrier spacing must exceed $2v_{rel,max}f_C/c_0 = 8.9 \text{ kHz}$ by at least one order of magnitude. The value chosen in [18] is $\Delta f = 90.9 \text{ kHz}$, resulting in an OFDM symbol duration of $T = 11 \mu\text{s}$.

The length of the cyclic prefix is at least $T_G \geq 2d_{max}/c_0 = 1.33 \mu\text{s}$. In practice, the CP length is chosen as an integer fraction of T , making $T_G = 1/8T = 1.375 \mu\text{s}$ a suitable choice.

Using these parameters, the constraints (3.142) and (3.143) for the range and Doppler ambiguity are satisfied by a large margin.

With Δf fixed, the minimum values for the number of carriers and OFDM symbols are $N \geq 825$ and $M \geq 253$ in order to achieve the minimum required bandwidth and frame duration, respectively. The values $N = 1024$ and $M = 256$ are therefore valid.

Communication Requirements To prove that the communication requirements are fulfilled, knowledge of the inter-vehicle channels at 24 GHz is required, which can only be reliably obtained by elaborate measurement campaigns. Because this was outside the technical means of this work, two sources of information were used: The characteristics of the inter-vehicular channel at 5.9 GHz, which has been researched in detail as part of the IEEE 802.11p standardization process [22] as well as a preliminary study of the 24 GHz channel obtained by raytracing models [1].

At 24 GHz, the free space path loss is larger than at 5.9 GHz, as are the absolute Doppler shifts, resulting in shorter excess delays, but larger Doppler spreads.

In both studies, different types of channels (urban, rural and highway) were analyzed. Table 3.5 shows the worst case results from [22] and [1],¹⁷ respectively. With the exception of $\tau_e = 1.5 \mu\text{s}$, these values are those obtained for the highway scenarios (in [1], the scenario is called

¹⁷[1] actually lists a smaller value for the coherence time, which was caused by an error in the raytracing setup. The value shown here is repeated with a correct setup.

Frequency	5.9 GHz	24 GHz
τ_e	1.5 μ s	0.86 μ s
B_D	1.11 kHz	2.72 kHz
B_C	410 kHz	293 kHz
T_C	0.3 ms	0.3 ms

Table 3.5: Channel characteristics for the 5.9 and 24 GHz bands

autobahn), where the velocities are the highest and the waves have more space to propagate.

If the values for 24 GHz are used, $T_G < \tau_e$, $B_D \ll \Delta f$ and $\Delta f > 1/T_C$ are satisfied. However, the coherence bandwidth of 195 kHz is only a factor of 2.14 larger than Δf . Of course, the values in Table 3.5 are worst-case; but to make data transmission reliable, a large percentage of the OFDM frame must be reserved for pilot symbols.

Regulation Regulation differs from region to region. In Germany, a bandwidth of 250 MHz is available for this kind of application [111], which is much larger than the OFDM radar bandwidth of 93.09 MHz, with a maximum EIRP of 20 dBm (100 milliwatts), which shall be used for P_{\max} .

Radar and Communication Ranges With the given noise figure and bandwidth, the noise power is $P_N = k_B \vartheta \cdot \text{NF} \cdot N \Delta f = 1.17 \times 10^{-12}$ W (or -89.3 dBm). For the given false alarm rate of $p_{\text{FA}} = 0.1$, the detection threshold is computed using (3.95),

$$\eta = P_N \ln(1 - \sqrt[N_M]{1 - p_{\text{FA}}}) = P_N \cdot 14.73 \quad (3.153)$$

With this value for η , the maximum detection range for a target with radar cross section $\sigma_{\text{RCS}} = 10 \text{ m}^2$ can be calculated from (3.150) and is $d_{\max} \approx 456 \text{ m}$. This is larger than the specified minimum detection range by a significant margin.

For the communication range however, the situation is different. On

each sub-carrier, E_S/N_0 is

$$\frac{E_S}{N_0} = \frac{P_{max} c_0^2 T}{(4\pi)^2 f_C^2 d_{comm}^2 k_B \vartheta N} \cdot \frac{T}{T + T_G} \quad (3.154)$$

$$= \frac{P_{max}}{P_N} \frac{c_0^2}{f_C^2 d_{comm}^2} \frac{T}{T_O} = 2.3 \text{ dB}. \quad (3.155)$$

If BPSK was used (every sub-carrier transports one bit), the gross bit rate (not considering pilot symbols) would be $1024/(T+T_G) = 82.7$ Mbps, exceeding the specified rate by a large margin. The bit error rate can be calculated by [112]

$$\text{BER} = Q \left(\sqrt{\frac{2E_b}{N_0}} \right) \approx 3 \cdot 10^{-2}. \quad (3.156)$$

Such a BER makes the system unusable, especially in an environment where the communication can be crucial for safety. In order to decrease the BER, multiple symbols must be used to encode a single bit (channel coding), thereby reducing the bit rate in favour of the bit error rate. Section 3.6.3 discusses this in greater detail.¹⁸

To summarize, it could be confirmed that the waveform suggested in [18] is suitable for OFDM radar. The parametrization also allows for communication, but reliable data transmission is only possible if additional mechanisms, such as encoding, are in place.

IEEE 802.11a/p waveforms

The previous waveform was a result of first having a specification, and then deriving suitable parameters. One advantage of OFDM radar is that it can make use of existing OFDM signals. For this reason two popular IEEE standards, 802.11a and 802.11p, are analysed with respect to their radar capabilities. Since these waveforms are explicitly designed for communication, their capabilities regarding data transmission do not require additional scrutiny.

¹⁸In Section 3.2 and Appendix A, the problem of increased noise is discussed when higher modulation alphabets, such as 16-QAM, are used. Because E_b/N_0 is so small on each carrier, this would never be used in 24 GHz OFDM radar, which is why the potential noise increase is not considered a problem in practice.

Standard	802.11a	802.11p
f_C	5.5 GHz	5.9 GHz
P_{\max}	20-30 dBm (depending on region)	33 dBm
Δf	20 MHz/64 = 312.5 kHz	5 MHz/64 = 78.125 kHz
T_G	$1/4T$	$1/4T$
N	52	52
M	≤ 1365	≤ 1365

Table 3.6: OFDM parameters for the 802.11a and 802.11p standards

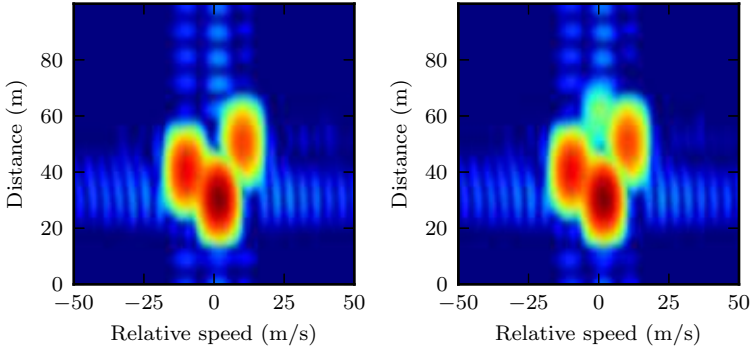
	802.11a	802.11p
Δd	9.23 m	36.92 m
Δv_{rel}	5 m/s	1.25 m/s
d_{\max}	≤ 120 m	≤ 480 m
$v_{\text{rel,max}}$	≤ 120 m	≤ 480 m
d_{unamb}	240 m	960 m
$v_{\text{rel,unamb}}$	6818.18 m/s	1588.98 m
$d_{\text{max,detect}}$	450 m	1588.98 m

Table 3.7: Radar figures of merit for 802.11a/p standards

Table 3.6 shows the signal specifications for the two standards. In both cases, the 52 carriers are arranged above and below the DC carrier, which is left free. This causes the DC carrier-related spurs discussed in Section 3.3.8, which is why only the carriers with an odd index are used for radar, implying $U = 2$. While this also means that half of the transmitted power is not used for radar, this is not a problem since the allowed transmit power is already higher than in the 24 GHz band, and the lower centre frequency causes less free space loss.

The number of OFDM symbols M depends on the amount of data transmitted. The value shown in Table 3.6 is the maximum value. In reality, a 802.11a/p transmitter could be configured to pad bursts to the maximum length without violating the standard, so this value shall be used in the following calculations.

Table 3.7 shows the figures of merit for radar operation using these signals. When compared with the signal specification from the previous section, the range resolution stands out as much worse. The 802.11p



(a) Three targets, with different Doppler. (b) A fourth, large target at a distance appears as an aliased image.

Figure 3.20: Periodogram using an 802.11a signal parametrization, using a Hamming window. All three main targets have a RCS of $\sigma_{\text{RCS}} = 10 \text{ m}^2$.

standard in particular has a range resolution which makes its usage in traffic scenarios unlikely, which is unfortunate since this standard was designed for inter-vehicle communication, and an additional usage for radar would have been highly beneficial.

For this reason, the focus shall lie on the 802.11a standard. While its range resolution is still fairly coarse, it is small enough to distinguish vehicles in moving traffic, assuming they keep a safe distance.

A noteworthy effect of the 802.11a is the high detection range. It is notably higher than the unambiguous range. In practice, this can cause artefacts in the periodogram when a large target, e.g. a building, is within the maximum detection ranges, but outside the unambiguous range. Fig. 3.20b shows such a case, where a large target ($\sigma_{\text{RCS}} = 300 \text{ m}^2$) is located 300 m from the radar; it appears as a target at 60 m.

While the overall performance of IEEE 802.11a OFDM signals is worse for radar than the wideband signal previously described in this section, the great advantage is that these signals are ubiquitous. Anywhere a transmitter for these signals is active (e.g. a wifi base station), radar

imaging can be performed without additional access to the EM spectrum.

A possible use case for this technique is equipping roadside base stations (or roadside units, RSUs) with radar processing. Such base stations can be used to provide vehicles with traffic or other information, while at the same time performing radar measurements (e.g. for speed limit enforcement), as suggested in [9]. The usage of OFDM-based RSUs is discussed, among others, in [29, 31].

3.6.3 Frame Design and Channel Coding

In order to encode an OFDM signal from the data bits to be transmitted, the physical signal parametrization is only one aspect. What is also relevant is how the data bits are encoded, and how they are mapped to sub-carriers.

As discussed in Section 3.2, the data encoding is not directly relevant for the radar algorithm, as the complex modulation symbols are removed from the received signal before processing. However, there is an indirect effect of the encoding, as it can affect the PAPR of the OFDM signal. A high PAPR can reduce the ability to detect targets, as it requires the amplifier to back off in order not to saturate with the receiver chain.¹⁹

To summarize, an OFDM frame has to be constructed so that it accounts for three things:

1. Pilot symbols have to be arranged so that an equalizer can reverse the effects of the fading channels.
2. Bits must be encoded in a way which enables decoding with a low bit error rate.
3. Symbol allocation should ensure a low PAPR.

As indicated above, there is no single optimal solution for the frame design. In the following, one configuration is presented for the wideband signal at 24 GHz as well as the frame encoding used by IEEE 802.11a.

¹⁹Usually, the limiting factor is the direct coupling between receive and transmit antennas, which will saturate the ADC.

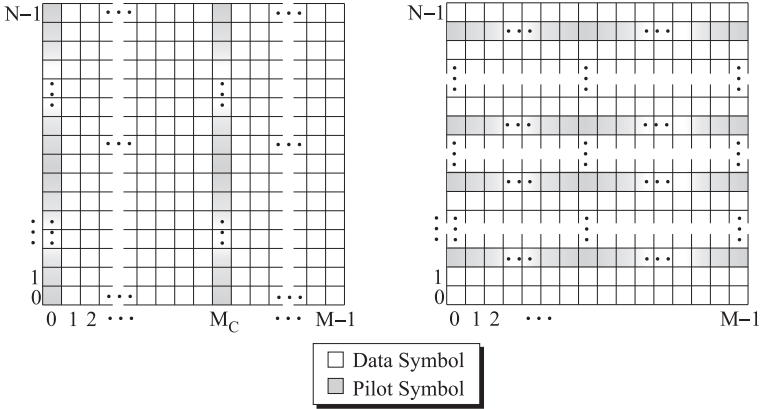


Figure 3.21: Frame structures for the wideband and 802.11a signals

N	M	U	M_C
1024	> 256	8	24

Table 3.8: Frame parameters for wideband OFDM radar

Wideband Frame Design

With this signal parametrization, the number of active carriers increases to $N = 1024$ (for $U = 1$), which can cause considerable PAPR (see Section 3.1.1).

Given that a higher value for U has several advantages (cf. Sections 3.3.8 and 4.5.3), the only disadvantage being a lower unambiguous range, U shall be fixed at 8, leaving 128 active sub-carriers on 8 orthogonal sub-carrier sets.

To occupy these 128 carriers, a frame design is suggested with highly reduced PAPR [5, 2, 128]. The basic frame structure is as shown in Fig. 3.21: Every OFDM symbol is the BPSK representation of a code word from a block code. Every M_C OFDM symbols, one pilot OFDM symbol is inserted for channel estimation and equalization purposes. M_C is chosen such that the time between pilot symbols is less than the co-

herence time,

$$M_C \leq \frac{T_C}{T_O}. \quad (3.157)$$

Using the value $T_C = 0.3\text{ms}$ from Table 3.5, this leads to a value of $M_C = 24$.

The reason this solution has low PAPR is the choice of using Reed-Muller Codes (RM-Codes) as the block code. In [82], Popovic shows that the PAPR of any Golay-sequence is bounded by a value of two (or 3 dB). In [81] the connection between Golay-sequences and the second order Reed-Muller-code, which provides efficient encoding and decoding methods, was recognized. The application of these codes in an OFDM radar context was also discussed in [37].

The r -th order binary RM-code $RM_2(r, m)$ comprises 2^k codewords of length 2^m , where k is given by

$$k = \sum_{i=0}^r \binom{m}{i}. \quad (3.158)$$

Of particular importance is the code $RM_2(2, m)$ comprising $2^{\frac{m(m-1)}{2}}$ cosets of the code $RM_2(1, m)$, each containing 2^{m+1} codewords. By partitioning the codewords of $RM_2(2, m)$ into cosets of $RM_2(1, m)$, the codewords with large values of PAPR can be isolated. If the transmitted codewords are restricted to those belonging to the Golay-cosets, the PAPR is bounded by 3 dB. For convenience of implementation, only one of the $m!/2$ Golay-cosets is used, which results in a code rate of

$$R_c = \frac{m+1}{2^m}.$$

As the length of the codewords increases, the code rate reduces to a very low value.

If only one Golay-coset is used, the minimum Hamming distance of the resulting code is given by $d_{\min} = 2^{m-1}$, whereas the minimum distance is $d_{\min} = 2^{m-2}$ if two or more Golay-cosets are used, thereby decreasing the ability of the code to detect and correct bit errors. Another advantage of using one single Golay-coset is that it reduces the complexity of the decoder. After subtracting the Golay-coset representative of a received codeword, the result can be decoded with a basic $RM_2(1, m)$ decoder. If a large number of cosets is used, this operation has to be done for

every coset representative, which increases the complexity. The binary Reed-Muller code of first order $RM_2(1, m)$ can be maximum-likelihood decoded using the fast Hadamard transform (FHT), which can be implemented efficiently in hardware [83]. Furthermore, the decoder can be realised as hard- or soft-decision decoder without extra complexity.²⁰

As only every U -th sub-carrier is used, the RM-code with $m = 7$ can be used, resulting in one code word of length $N = 128$ per OFDM symbol, thereby guaranteeing the PAPR of 3 dB.

Every error of weight less than half the Hamming distance $wt(e) < 2^{m-2} = 32$ can be corrected if one Golay-coset is used. If the BER before the decoder is given by p , the frame error rate is thus

$$P_{\text{frameerr}} = 1 - (F_{p,n}(32))^M \quad (3.159)$$

where $F_{p,n}(x)$ is the CDF of a binomial distribution with parameters p being the aforementioned code bit error rate and $n = N/U$. As an example, consider the requirements for communication as specified in Table 3.4, where communication should still be possible at $d_{\text{comm}} = 400$ m distance. Judging by free space attenuation, E_S/N_0 for $U = 8$ and therefore 128 active carriers is

$$\frac{E_S}{N_0} = \frac{P_{\text{max}} c_0^2 T U}{(4\pi)^2 f_C^2 d_{\text{comm}}^2 k_B \vartheta N} \cdot \frac{T}{T + T_G} \quad (3.160)$$

$$= \frac{P_{\text{max}}}{P_N} \frac{c_0^2}{f_C^2 d_{\text{comm}}^2} \frac{U T}{T_O} = 11.3 \text{ dB}. \quad (3.161)$$

Using (3.156), the probability for incorrectly decoding one code bit with $E_S/N_0 = 11.3$ dB is 10^{-7} . From (3.159), this corresponds to a near-zero frame error rate.²¹ This seems like a very large safety margin, but first, it should be remembered that the function of the code is also to reduce PAPR and second, as was shown in [5], E_S/N_0 can drop down to -5 dB in heavy fading situations even at 100 m distance, which are often those scenarios where reliable data transmission is crucial.

The achievable data rate of the system using the parameters of Table 3.8 is

$$r = \frac{N}{U} \cdot R_c \cdot \frac{1}{T_O} \frac{M_C - 1}{M_C} \approx 596.7 \text{ kbps}. \quad (3.162)$$

²⁰This algorithm is often referred to as the ‘‘Green Machine’’ [84, p. 33].

²¹With double precision (64 bits) floating point calculation, the precise frame error rate is not calculable.

While this is far below the possible throughput of a system with a bandwidth of nearly 100 MHz, it guarantees low PAPR, and it is robust even in extreme fading scenarios while still being well above the specifications from Tab 3.4.

IEEE 802.11a

In the previous section the frame structure was open for discussion and could be configured to serve both the radar and communication components. When using 802.11a as the signal source, the frame structure is dictated by the standard (cf. Fig. 3.21). This has some disadvantages, as 802.11a was only optimized for short range stationary communication links. In [22], measurements were taken which show that 802.11a is not ideally suited for inter-vehicular operations in rural and highway scenarios. It is possible that increase of T_G and a different pattern for the pilot symbols would solve this problem, but this is not an option with this standard, and was therefore not further researched.

PAPR was not considered in 802.11a, either. According to [33], the effective PAPR in a random OFDM signal is $2 \ln N$, which, for $N = 52$, results in a PAPR of approx. 9 dB – a 6 dB increase over the RM-encoded OFDM signal, despite using fewer carriers.

The encoding used in 802.11a is the industry-standard convolutional encoder of length 7 and rate $R_c = 1/2$, followed by an interleaver and optional puncturing to increase the code rate to $R_c = 2/3$ or even $R_c = 3/4$. What is relevant for the radar is that the transmitter may adaptively select a modulation alphabet (one of BPSK, QPSK, 16-QAM or 64-QAM), which may cause additional noise as described in Section 3.2 and Appendix A.

The pilot symbols are transmitted on four dedicated sub-carriers (unlike the proposed wideband configuration, where pilot symbols are fixed to OFDM symbols), as shown in Fig 3.21. This is possible as the encoding does not enforce any particular sub-carrier allocation of the code bits, whereas the RM code words have to be mapped to one OFDM symbol each.

Further details on the 802.11a frame structure can be found in the according standard [58].

4

Multi-user OFDM Radar networks

Implementing OFDM radar instead of a more established radar technology, such as FMCW radar, is only really useful if multiple devices are using it to communicate amongst each other, thereby forming an *OFDM radar network*.

The example of using OFDM radar in a vehicular context is such a case, where vehicles and possibly elements of the traffic infrastructure can use the OFDM signals to simultaneously sense their surroundings and exchange information. It is evident that both of these components are critical to traffic safety.

This presents another technical challenge, as the individual OFDM radar nodes now have to be coordinated. As discussed in Chapter 2, vehicular communication networks are ad-hoc in nature and have a random and time-variant topology, which makes it difficult to access the medium without collision.¹ The inclusion of a radar component exacerbates this

¹In this context, a *collision* describes the case when two or more transmitters are active at the same time, thereby interfering with each other.

problem: Radar sensors have to access the medium on a regular basis with frames of a certain minimum length in order to reliably perform, making collisions even more likely.

This chapter shall discuss the influence of interference from other OFDM radar nodes (also referred to as *co-channel interference*) on the radar performance. First, some basic rules for OFDM radar networks are discussed which are necessary when operating as a network. Next, a stochastic model for the co-channel interference is derived. This allows for an analytical description of the joint performance of a radar network by introducing the *radar network outage* as a figure of merit.²

4.1 Multi-user access

The question on how well radar networks perform is closely related to how the individual nodes access the medium. OFDM radar networks need at least some kind of coordination between nodes when accessing the medium; however, this multiple access scheme must be flexible enough to allow for an ad-hoc operation.

In the following, it is assumed that the frequency is subdivided as described in Section 3.3.8. This allows multiple users to access the channel at the same time on separate frequencies (a method known as orthogonal frequency division multiple access, OFDMA), but also requires time-synchronous access to the channel. To understand this, consider the example shown in Fig. 4.1. The sub-carriers are divided into three subsets, and three users are accessing it at the same time. User 1 and user 2 are transmitting simultaneously, whereas the third user is asynchronous with regard to the others. When a receiving node tries to demodulate this symbol by performing the FFT operation (see Section 3.3), it only demodulates a part of the third user's symbol, making it appear to have a shorter OFDM symbol duration. After the FFT operation, the signals from user 1 and 2 are correctly mapped to orthogonal carriers. The energy from third user's OFDM is leaked across all sub-carriers, interfering with the symbols from the first two users.

Therefore, the following type of multi-user access is postulated:

²The majority of the results in this chapter were previously published in [10].

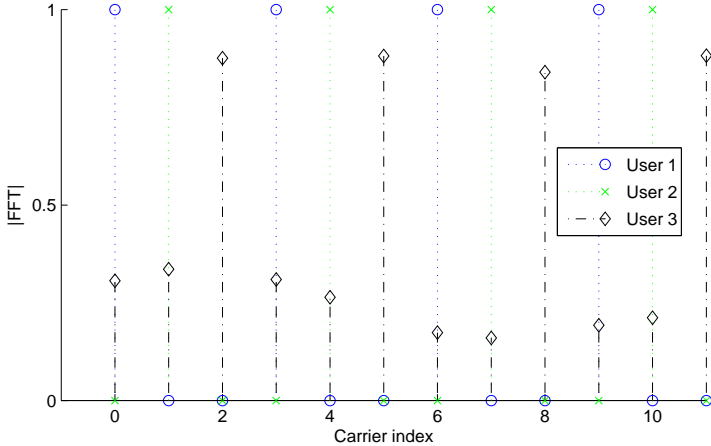


Figure 4.1: Three users accessing the medium on three different channels, but with a timing offset

- Access to the medium can only happen at the beginning of a timeslot, which is known by all nodes.
- Medium access is allowed on one of U logical channels. Every channel may only utilize a subset of the OFDM sub-carriers which consist of every U -th sub-carrier, starting at sub-carrier u , where u denotes the channel number.
- Medium access is random and independent among nodes, i.e. every node may randomly access any channel starting at the beginning of any time slot with probability p_{Tx} . While this does not consider any kind of medium access protocol, such as back-off mechanisms or similar collision avoidance techniques, it allows a radar system to access the medium at regular intervals, as required for the radar system.

In such a system, the only time a collision occurs is when two or more nodes select the same timeslot and sub-carrier set for transmission. However, even when different channels are used, transmission in the same timeslot can cause interference because the Doppler spread on the channels will cause a lack of orthogonality between signals from different

receivers, thus leaking interference power into other channels. The local oscillators of the individual nodes might not be exactly aligned, which would additionally cause a non-orthogonality between nodes.

4.1.1 Practical considerations

Stipulating simultaneous access by time slots requires a global clock. This could be provided by GPS – in the context of vehicular technology, GPS receivers are very common. The guard interval T_G must then be chosen large enough to allow for clock inaccuracies *and* different signal arrival times due to variation in distance to the other radar transmitters.

A positive side-effect is the simplified detection and timing synchronisation, as it is only necessary to search for a burst at the beginning of every time slot. Also, the GPS clock can be used to control the local oscillator, thereby increasing its accuracy.

4.2 Radar network outage

In communication networks, *outage* is a common concept to describe the case where a point-to-point link within the network is unable to achieve a given minimum rate. Goldsmith [100] defines outage as the case where SINR (the ratio of received signal energy to the sum of noise and interference energy) drops below a certain value due to slowly varying, random channel conditions. This notion can directly be transferred to a radar network by defining outage as the case when the reflected power at the receiver is so low that a given object can no longer be distinguished from noise and interference, caused by collisions with other nodes.

For a meaningful analysis, a *reference target* is introduced as a fixed object at range r_{Ref} and with a radar cross section $\sigma_{\text{RCS,Ref}}$. The performance of the radar network is then completely characterized by the detection of the reference target. The values $\sigma_{\text{RCS,Ref}}$ and r_{Ref} are chosen depending on the application at hand (see Section 3.6). Whether an object is detected or not depends on the received backscattered power

$$P_{\text{Rx,Ref}} = \frac{P_{\text{Tx}} G c_0^2 \sigma_{\text{RCS,Ref}}}{(4\pi)^3 f_c^2 r_{\text{Ref}}^4}. \quad (4.1)$$

The outage definition is therefore the same for any object with the same backscattered power $P_{\text{Rx,Ref}}$. Here, G is the total gain of both transmit and receive paths.

As discussed in Section 3.3.6, detection is only possible if the peak in the periodogram corresponding to the target has a maximum value higher than the threshold η , which is a random variable if the interference power is assumed random as well.

Assume the periodogram has a peak at indices n_0, m_0 , then the peak value of the periodogram is (cf. Section 3.3.1):

$$\text{Per}(n_0, m_0) = \|P_{\text{Rx}} \cdot NM + Z\|^2. \quad (4.2)$$

The *outage probability* is therefore the probability that this peak is smaller than η ,

$$p_{\text{out}} = \Pr[\text{Per}(n_0, m_0) < \eta] \quad (4.3)$$

The actual value of $\text{Per}(n_0, m_0)$ depends on the received power, the processing gain and the random value of the noise at that bin (Section 3.3.6 explains this in greater detail). An approximation which simplifies the following analyses is found by replacing (4.2) with its expected value

$$P_{\text{peak}} := \mathbb{E}[\text{Per}(n_0, m_0)] \quad (4.4)$$

$$= P_{\text{Rx}} \cdot NM + \mathbb{E}[|Z|^2] \quad (4.5)$$

$$\approx \text{Per}(n_0, m_0). \quad (4.6)$$

This changes the outage definition, which then becomes

$$p_{\text{out}} = \Pr[P_{\text{peak}} < \eta] \quad (4.7)$$

$$\approx 1 - p_D. \quad (4.8)$$

By applying this approximation, outage is the complementary event to a detection; p_D is the detection probability. This simplification is discussed in the following sections in greater detail.

As for the threshold η , the definition from (3.95) can still be used:

$$\eta = \sigma_N^2 \underbrace{\ln \frac{NM}{c} \sqrt{1 - p_{\text{FA}}}}_c. \quad (4.9)$$

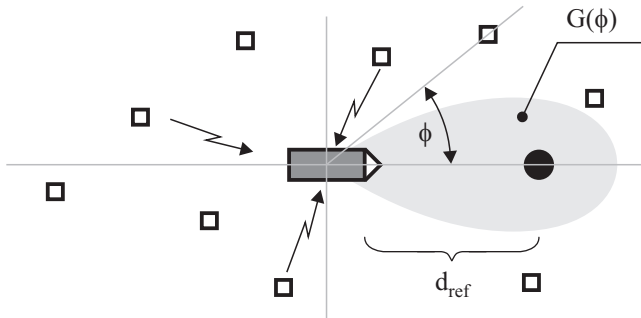


Figure 4.2: An example of the network topology: the reference node (centre) is trying to detect a reference target (circle). Other systems (squares) are randomly distributed and can interfere.

The threshold is the product of the noise power and a constant safety coefficient, which is abbreviated c in the following. In a multi-user scenario, this threshold depends on both thermal noise as well as interference.

On a side note, multi-path propagation of the radar signal does not affect the outage probability, and is therefore not considered here. A multi-path backscattering might produce peaks in the periodogram which do not correspond to true targets, but this is a common problem of all radar systems and must be treated downstream in the processing chain.

4.3 Interference model

The difference between operating a single radar node and an entire network is the increased interference caused by collisions, or *co-channel interference*.

To model this interference, a stochastic model is applied for the interferer geometry.³ The reference node is located at the origin of a plane. The position of the other, interfering, nodes are randomly determined by a

³Stochastic geometry as a tool for research on vehicular networks has previously been proposed in [62], which suggests its suitability in this context.

two-dimensional Poisson Point Process (PPP) with density λ . Fig. 4.2 illustrates such a scenario.

Choosing a PPP to model the geometry allows the application of results of stochastic geometry to analyze the interference. The main reason PPPs are used, however, is the application OFDM radar networks is intended for, where the nodes are not stationary. This mobility causes a high amount of “spatial randomness”. Such a spatial model has been shown to capture properly these random spatial dynamics affecting the interference [118].

It is important to realise that all nodes represented by this PPP are OFDM transmitters of the same type as the reference node. Because of the homogeneous setup, the results for the reference node are representative for all other nodes as well.

Unlike in the previous chapter, it is no longer possible to neglect the azimuth dependency. As this is a radar system, the azimuth ϕ of the targets must be estimated as well as the range and Doppler. How the radar system implementation solves this problem is irrelevant for this study; what matters is that the angular resolution results in a receiver directivity which can be expressed as azimuth-dependant antenna gain $G(\phi)$. The transmitters are assumed to be omnidirectional so they can communicate with all other nodes. Section 4.3.1 discusses this in greater detail.

For the radar processing methods from Section 3.3 to still be applicable, the total interference must be WGN. Conditioning on a certain spatial configuration, assume I interferers, with $\mathbf{F}_{\text{Ix},i}$ being the transmit frame of the i -th interferer. The noise matrix \mathbf{Z} now does not only contain the receiver noise, but also energy from the interfering transmit symbols. By assuming synchronous interference (see Section 4.3), the total noise matrix can be analyzed element-wise:

$$(\mathbf{Z}_{\text{total}})_{k,l} = \mathbf{Z}_{k,l} + \sum_{i=0}^{I-1} \sqrt{b_i} \frac{(\mathbf{F}_{\text{Ix},i})_{k,l}}{(\mathbf{F}_{\text{Tx}})_{k,l}} e^{j\varphi_i}. \quad (4.10)$$

Note that the $(\mathbf{F}_{\text{Ix}})_{k,l}$ are zero for interferers which use a different channel from the reference node, assuming perfect orthogonality.

On top of the receiver noise, $\mathbf{Z}_{\text{total}}$ now contains a sum of complex values with random amplitude b_i and phase φ_i ; the latter can be modelled

as uniformly distributed within $[0, 2\pi)$. The former is modelled by an exponential path loss,

$$b_i = \mathbf{g}_i \frac{\beta}{r_i^\alpha} G(\phi_i), \quad (4.11)$$

where r_i is the distance to the origin, ϕ_i the azimuth and α the path loss exponent. β is a constant attenuation factor which is assumed to fulfill

$$\beta = P_{\text{Tx}} \frac{c_0^2}{(4\pi)^2 f_C^2} \quad (4.12)$$

in correspondence with free space path loss. \mathbf{g}_i is an optional random small-scale power attenuation parameter with distribution function $F_{\mathbf{g}}(g)$ (as the fading of the nodes is identically distributed, the distribution itself does not depend on i). Section 4.4 discusses the cases where $\mathbf{g}_i = 1$ (i.e. no fading), or i.i.d. exponentially distributed with unit mean (Rayleigh fading), but if $F_{\mathbf{g}}(g)$ is known, other types of fading can be analyzed in the same fashion. This fading parameter covers multi-path propagation of the interference signals.

In the special case where the modulation has constant amplitude (e.g. as in PSK) and the amplitude is Rayleigh distributed, $\mathbf{Z}_{\text{total}}$ is a sum of i.i.d. random variables, and therefore is normal distributed. For the more general case where the b_i follow any distribution (the definition of the path loss (4.11) states that the b_i depend on the distance of the interferers to the reference node and are thus *not* identically distributed), the central limit theorem is considered, which suggests that a small number of summands (ten to twelve) suffice for $\mathbf{Z}_{\text{total}}$ to be approximately Gaussian [106, Chap. 2].

For the rest of this chapter, the index “total” shall be omitted and \mathbf{Z} is used to describe the compound noise and interference with total two-sided noise power $\sigma_N^2 + \tilde{Y}$, where \tilde{Y} denotes the random variable⁴ representing the total interference power.

4.3.1 Influence of directivity

As stated above, the nodes transmit omnidirectionally, in order to allow broadcasting. The radar processing unit however must have a way to de-

⁴In the following, all the random variables related to the PPP are typeset without serifs.

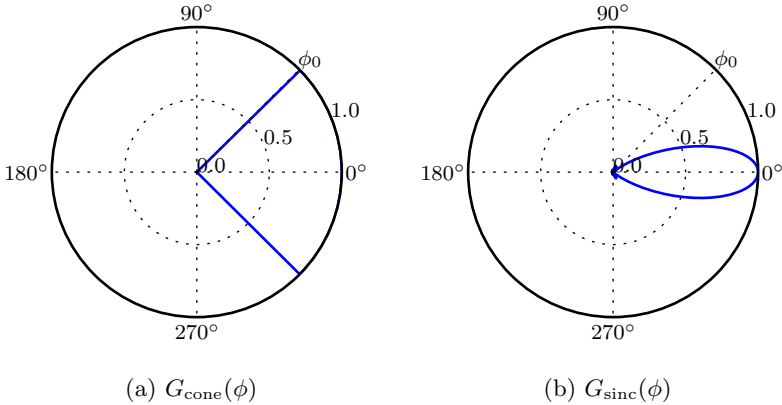


Figure 4.3: Gain functions $G_{\text{cone}}(\phi)$ and $G_{\text{sinc}}(\phi)$

fect the azimuth of an object, and therefore have an azimuth-dependant receiver gain. As a consequence, an interferer causes less interference when its transmission originates from a different angle than the reference target (see also Fig. 4.2).

This must be factored in when calculating the total interference power, note that $G(\phi)$ is already part of (4.11).

The actual shape of $G(\phi)$ is highly dependent on the specific implementation. If applicable, an approximation of $G(\phi)$ by a simple representation can help to obtain manageable analytic results.

Two directivity functions used in the following are the cone shape,

$$G_{\text{cone}}(\phi) = \mathbf{1}_{|\phi| < \phi_0}, \quad -\frac{\pi}{2} \leq \phi < \frac{\pi}{2} \quad (4.13)$$

and a sinc shape,

$$G_{\text{sinc}}(\phi) = \text{sinc}^2\left(\frac{\phi}{\phi_0}\right), \quad -\frac{\pi}{2} \leq \phi < \frac{\pi}{2}. \quad (4.14)$$

Both are defined by a beam width ϕ_0 and are depicted in Fig. 4.3. It must be emphasized that these directivity functions are crude approximations of realistic beam shapes, but are useful for analytical derivations.

4.4 Analytical bounds

Having derived a model for the interference, everything is in place to calculate the target metric, i.e. the outage probability. Because these derivations depend on results from both Chapters 3 and 4, this section begins with a full list of assumptions and approximations relevant to the outage probability.

Assumptions

- The total interference \mathbf{Z} can be modelled by AWGN.

This implies a clock synchronisation as discussed in Section 4.1, and that the data sent by the individual interferers is uncorrelated. Note that this is accurate for an OFDM radar system as described in Chapter 3; it merely requires the individual elements of \mathbf{Z} to be i.i.d. Gaussian distributed (cf. Section 4.3).

- The medium access can be described by a slot access probability p_{Tx} , and a transmitting node will randomly choose one of U logical channels, each with equal probability (cf. Section 4.1).
- The attenuation between interfering transmitters and the reference system is modelled by path loss and a (random) fading coefficient, see (4.11).

These two assumptions might be oversimplified for a specific scenario, but are the most sensible assumptions if the OFDM radar system is not specified more closely (e.g. if the MAC protocol is unknown).

- Nodes are distributed uniformly and independently.

This assumption allows the use of existing results from stochastic geometry to derive analytical results. It is motivated by the fact that due to the mobility of the nodes, their relative position changes all the time and is thus different between timeslots.

Approximations

- Sub-carriers are always orthogonal, thus, interference on a different channel does not affect the radar system.
- An ideal radar system can always detect the reference target if $P_{\text{peak}} > \eta$, i.e. (4.6) is an equality.

These are the only approximations in this model which are designed to facilitate the derivation of analytical bounds. Their influence is discussed in Sections 4.5.2 and 5.3.

4.4.1 Stochastic modeling

Given the synchronized slotted medium access of the nodes, the network is considered in an arbitrarily chosen slot, or *snapshot*. In this snapshot, the potentially interfering nodes are assumed to follow a stationary PPP of density λ . From Slyvniak's theorem [113, 114] it follows that the law of the PPP is not changed by adding a node. Due to the stationarity property, this node can be placed in the origin without loss of generality. This node shall be known as the *reference node* as it will be used to measure the typical performance in a given configuration.

Since the medium access is uncoordinated among the nodes, i.e., each node accesses the medium independently of each other with probability p_{T_x} , the set of interfering nodes can be obtained by independent thinning of the original PPP [116]. The resulting point process is again Poisson distributed with density $p_{\text{T}_x}\lambda$.

To describe the random sub-carrier selection, a mark is attached to every node. Formally, the sub-carrier chosen by node i is designated by the mark \mathbf{u}_i . Since the sub-carriers chosen by the nodes appear random to the reference node, and all channels are equally likely, \mathbf{u}_i has a discrete distribution function $F_{\mathbf{u}}(u) = 1/U$, which is the same for all i . In the same fashion, the small-scale fading between the i -th interferer and the reference node is denoted by another mark, \mathbf{g}_i . A third mark, \mathbf{x}_i , describes the position of the i -th node on the two-dimensional plane. The coordinates of the interferers are uniformly distributed.

Having introduced all relevant system parameters, the set of interferers can now be formally defined by the *stationary independently marked PPP*

$$\Phi := \{(\mathbf{x}_i, \mathbf{u}_i, \mathbf{g}_i)\}_{i=1}^{\infty} \quad (4.15)$$

of (spatial) density $p_{\text{Tx}}\lambda$, where the \mathbf{x}_i denote the random interferer locations, and \mathbf{u}_i and \mathbf{g}_i are the previously discussed marks associated with interferer i . Note that $(\mathbf{x}_i, \mathbf{u}_i, \mathbf{g}_i) \in \mathbb{R}^2 \times \mathbb{U} \times \mathbb{R}_+$, where $\mathbb{U} = \{1, \dots, U\}$.

As the probability for the choice for \mathbf{u} is uniformly distributed, it is assumed without loss of generality that the reference node is using the first channel, $u_{\text{ref}} = 1$. In this case, the sum interference power measured at the reference node (in the origin) is given by

$$\Upsilon = \sum_{(\mathbf{x}_i, \mathbf{u}_i, \mathbf{g}_i) \in \Phi} \mathbb{1}_{(\mathbf{u}_i=1)} G(\angle \mathbf{x}_i) \mathbf{g}_i \|\mathbf{x}_i\|^{-\alpha}, \quad (4.16)$$

where $\|\mathbf{x}_i\|^{-\alpha}$ describes the large-scale path loss between interferer location $\mathbf{x}_i \in \mathbb{R}^2$ and the origin, and $\angle \mathbf{x}_i = \phi_i$ the interferer's azimuth.

At the receiver, the sum interference is superimposed by thermal noise of power σ_N^2 . As shown previously, the interference noise can be assumed to be conditionally AWGN. Consequently, the total noise is conditionally AWGN as well with a (random) power equal to $\tilde{\Upsilon} + \sigma_N^2$.

Υ is a normalized, unit-less interference power term, which is introduced for its mathematical utility. On the other hand, $\tilde{\Upsilon}$ includes the physical effects, such as frequency-dependence of the free space path loss. Converting one value into another is done by

$$\tilde{\Upsilon} = \Upsilon \cdot U\beta. \quad (4.17)$$

The factor β plays the same role as in (4.10). U is necessary because the power on the individual sub-carriers is scaled by the same factor to retain a constant transmit power.

4.4.2 Outage probability analysis

In Section 4.2, the outage probability was defined as

$$p_{\text{out}} = \Pr [P_{\text{peak}} < \eta]. \quad (4.18)$$

In order to make use of the stochastic geometry, this must be expressed in terms of (4.16). First, the normalized interference power is converted into a physical quantity by scaling with $U\beta$. The threshold can then be replaced by a function of the interference power by inserting 4.5 and 4.9. This results in

$$p_{\text{out}} = \Pr \left[P_{\text{Rx}}NM + \underbrace{U\beta\Upsilon + \sigma_N^2}_{\Upsilon} < (U\beta\Upsilon + \sigma_N^2)c \right] \quad (4.19)$$

$$= \Pr \left[\Upsilon \geq \underbrace{\frac{1}{U\beta} \left((c-1)^{-1} P_{\text{Rx}}NM - \sigma_N^2 \right)}_{:=\omega} \right]. \quad (4.20)$$

Note that solving for Υ assumes that $c-1$ is positive; however, unless p_F is close to 1, this is always the case. ω is now a normalized power level consisting of all relevant system parameters.

Calculating p_{out} requires the evaluation of the tail probability of Υ . Although solving (4.20) directly is an analytically intractable problem, an upper and lower bound can be derived.

Lower bound

For communication networks, Weber et al. introduced the dominant interferer phenomenon [115] for obtaining lower bounds, which can be adapted for the case of radar network outage. The idea is to divide the set of total interferers into the sets of dominant and non-dominant interferers. Formally, these sets are defined as

$$\Phi_{\text{d}} := \left\{ (\mathbf{x}_i, \mathbf{u}_i, \mathbf{g}_i) \in \Phi \mid \mathbf{1}_{(u_i=1)} G(\angle \mathbf{x}_i) \mathbf{g}_i \|\mathbf{x}_i\|^{-\alpha} \geq \omega \right\} \quad (4.21)$$

and

$$\Phi_{\text{nd}} := \left\{ (\mathbf{x}_i, \mathbf{u}_i, \mathbf{g}_i) \in \Phi \mid \mathbf{1}_{(u_i=1)} G(\angle \mathbf{x}_i) \mathbf{g}_i \|\mathbf{x}_i\|^{-\alpha} < \omega \right\}. \quad (4.22)$$

An interferer is termed dominant if it is individually capable of creating outage at the reference node. All other nodes are called non-dominant. Note that $\Phi_{\text{d}} \cap \Phi_{\text{nd}} = \emptyset$, and $\Phi_{\text{d}} \cup \Phi_{\text{nd}} = \Phi$.

Each set of interferers creates a corresponding interference power

$$Y_d := \sum_{(x_i, u_i, \mathbf{g}_i) \in \Phi_d} \mathbf{1}_{(u_i=1)} G(\angle x_i) \mathbf{g}_i \|x_i\|^{-\alpha} \quad (4.23)$$

and

$$Y_{nd} := \sum_{(x_i, u_i, \mathbf{g}_i) \in \Phi_{nd}} \mathbf{1}_{(u_i=1)} G(\angle x_i) \mathbf{g}_i \|x_i\|^{-\alpha}, \quad (4.24)$$

such that $Y = Y_d + Y_{nd}$. Another way to write the outage probability is thus

$$p_{\text{out}} = \Pr [Y_d + Y_{nd} > \omega]. \quad (4.25)$$

The lower bound is constructed by neglecting the non-dominant term:

$$p_{\text{out}} \geq p_{\text{out},d} := \Pr [Y_d > \omega] \quad (4.26)$$

$$= \Pr [\Phi_d \neq \emptyset], \quad (4.27)$$

where the equality stems from the fact that the presence of one dominant interferer already suffices to make the event $Y > \omega$ true. The complementary probability of outage is therefore the probability that Φ_d is an empty set. As $|\Phi_d|$ is a Poisson distributed variable, this yields

$$p_{\text{out},d} = 1 - \exp(-\mu), \quad (4.28)$$

where the mean μ can be calculated as (cf. [116])

$$\mu = p_{\text{Tx}} \lambda \int_{\mathbb{R}^2} \mathbb{E} [\mathbf{1}_{(u=1)} \mathbf{1}_{(G(\angle x) \mathbf{g} \|x\|^{-\alpha} \geq \omega)}] dx \quad (4.29)$$

$$= p_{\text{Tx}} \lambda \int_{\mathbb{R}^2} \Pr [u = 1] \Pr [G(\angle x) \mathbf{g} \|x\|^{-\alpha} \geq \omega] dx \quad (4.30)$$

$$= \frac{p_{\text{Tx}} \lambda}{U} \int_{\mathbb{R}^2} \Pr \left[\mathbf{g} \geq \frac{\omega \|x\|^\alpha}{G(\angle x)} \right] dx. \quad (4.31)$$

At this point, the bound only depends on the probability distribution of the fading and the gain function.

Pure path loss If no small-scale fading occurs ($\mathbf{g} \equiv 1$), the probability term (4.31) simply becomes a deterministic function of x ,

$$\Pr \left[\mathbf{g} \geq \frac{\omega \|x\|^\alpha}{G(\angle x)} \right] \rightarrow \mathbf{1}_{(\|x\| \leq (\frac{G(\angle x)}{\omega})^{1/\alpha})}, \quad (4.32)$$

and therefore

$$\mu = \frac{2p_{\text{Tx}}\lambda}{U} \int_0^\pi \int_0^{\left(\frac{G(\phi)}{\omega}\right)^{\frac{1}{\alpha}}} r \, dr \, d\phi \quad (4.33)$$

$$= \frac{p_{\text{Tx}}\lambda}{U} \int_0^\pi \left(\frac{G(\phi)}{\omega}\right)^{\frac{2}{\alpha}} d\phi. \quad (4.34)$$

Inserting this result into (4.28) yields

$$p_{\text{out}} \geq p_{\text{out,d}} = 1 - \exp\left(-\frac{p_{\text{Tx}}\lambda}{U} \omega^{-\frac{2}{\alpha}} \int_0^\pi G(\phi)^{\frac{2}{\alpha}} d\phi\right) \quad (4.35)$$

Rayleigh fading If the amplitude of the interferer's signal is subject to Rayleigh fading, the interference power is exponentially distributed and therefore

$$\Pr\left[\mathbf{g} \geq \frac{\omega\|x\|^\alpha}{G(\angle x)}\right] = \exp\left(-\frac{\omega\|x\|^\alpha}{G(\angle x)}\right), \quad (4.36)$$

which allows solving for μ :

$$\mu = \frac{2p_{\text{Tx}}\lambda}{U} \int_0^\pi \int_0^\infty r \exp\left(-\frac{\omega r^\alpha}{G(\phi)}\right) dr \, d\phi \quad (4.37)$$

$$= \frac{2p_{\text{Tx}}\lambda}{\alpha U} \int_0^\pi \int_0^\infty t^{\frac{2}{\alpha}-1} \exp\left(-\frac{\omega t}{G(\phi)}\right) dt \, d\phi \quad (4.38)$$

$$= \frac{p_{\text{Tx}}\lambda}{U} \Gamma\left(1 + \frac{2}{\alpha}\right) \int_0^\pi \left(\frac{G(\phi)}{\omega}\right)^{\frac{2}{\alpha}} d\phi. \quad (4.39)$$

In this case, the lower bound becomes:

$$p_{\text{out}} \geq p_{\text{out,d}} = 1 - \exp\left(-\frac{p_{\text{Tx}}\lambda}{U} \omega^{-\frac{2}{\alpha}} \Gamma\left(1 + \frac{2}{\alpha}\right) \int_0^\pi G(\phi)^{\frac{2}{\alpha}} d\phi\right). \quad (4.40)$$

The only difference between the Rayleigh fading and the path loss-only scenario is the $\Gamma\left(1 + \frac{2}{\alpha}\right)$ in the exponential function.

If the gain function $G(\phi)$ is simple enough, this integral can be solved analytically. Otherwise (e.g. if the antenna gains are only given in tabular format), numerical solutions must be applied.

For the very simple case of a cone-shaped antenna function $G_{\text{cone}}(\phi)$, the lower bound becomes

$$p_{\text{out}} \geq p_{\text{out,d}} = 1 - \exp\left(-\frac{p_{\text{Tx}}\lambda\phi_0}{U}\omega^{-\frac{2}{\alpha}}\Gamma\left(1 + \frac{2}{\alpha}\right)\right). \quad (4.41)$$

Upper bound

If there are no dominant interferers ($Y_{\text{d}} < \omega$), the total interference from the non-dominant interferers can still be enough to cause outage. The outage probability can therefore be expressed as a function of the outage probability due to dominant interferers and the probability that the non-dominant interferers cause the outage,

$$p_{\text{out}} = \Pr[Y_{\text{d}} \geq \omega] + \Pr[Y_{\text{d}} < \omega] \Pr[Y_{\text{nd}} \geq \omega] \quad (4.42)$$

$$= p_{\text{out,d}} + (1 - p_{\text{out,d}}) \Pr[Y_{\text{nd}} \geq \omega], \quad (4.43)$$

where the second equation stems from the fact that dominant interferers always cause outage when present.

An upper bound of the right-hand term can be found by applying Markov's inequality [117],

$$\Pr[Y_{\text{nd}} \geq \omega] \leq \frac{1}{\omega} \mathbb{E}[Y_{\text{nd}}]. \quad (4.44)$$

$\mathbb{E}[Y_{\text{nd}}]$ can be computed using Campbell's Theorem [113]:

$$\mathbb{E}[Y_{\text{nd}}] = \mathbb{E}\left[\sum_{(x_i, u_i, \mathbf{g}_i) \in \Phi_{\text{nd}}} \mathbf{1}_{(u_i=1)} \mathbf{1}_{(G(\angle x) \|\mathbf{g}\| |x|^{-\alpha} < \omega)} G(\angle x_i) \mathbf{g}_i \|x_i\|^{-\alpha}\right] \quad (4.45)$$

$$= p_{\text{Tx}}\lambda \int_{\mathbb{R}^2} \mathbb{E}\left[\mathbf{1}_{(u=1)} \mathbf{1}_{(\mathbf{g} < \frac{\omega \|x\|^\alpha}{G(\angle x)})} G(\angle x) \|\mathbf{g}\| |x|^{-\alpha}\right] dx. \quad (4.46)$$

This is further simplified by making use of the fact that the marks are independent and splitting up the mean,

$$\mathbb{E}[Y_{\text{nd}}] = p_{\text{Tx}}\lambda \int_{\mathbb{R}^2} \Pr[u = 1] \mathbb{E}\left[\mathbf{1}_{(\mathbf{g} < \frac{\omega \|x\|^\alpha}{G(\angle x)})} \mathbf{g}\right] G(\angle x) \|x\|^{-\alpha} dx \quad (4.47)$$

If small-scale fading is neglected, the expected value inside the integral becomes

$$\mathbb{E} \left[\mathbf{1}_{\left(\mathbf{g} < \frac{\omega \|x\|^\alpha}{G(\zeta x)} \right) \mathbf{g}} \right] = \mathbf{1}_{\left(\|x\| \geq \left(\frac{G(\zeta x)}{\omega} \right)^{\frac{1}{\alpha}} \right)} \quad (4.48)$$

and thus

$$\mathbb{E} [Y_{\text{nd}}] = \frac{2p_{\text{Tx}}\lambda}{U} \int_0^\pi G(\phi) \int_0^\infty r^{-\alpha+1} \mathbf{1}_{\left(r \geq \left(\frac{G(\phi)}{\omega} \right)^{\frac{1}{\alpha}} \right)} dr d\phi \quad (4.49)$$

$$= \frac{2p_{\text{Tx}}\lambda}{U} \int_0^\pi G(\phi) \int_{\left(\frac{G(\phi)}{\omega} \right)^{\frac{1}{\alpha}}}^\infty r^{-\alpha+1} dr d\phi \quad (4.50)$$

$$= \frac{2p_{\text{Tx}}\lambda}{U(\alpha-2)} \int_0^\pi G(\phi) \left(\frac{G(\phi)}{\omega} \right)^{\frac{2}{\alpha}-1} d\phi. \quad (4.51)$$

In this case, the tail probability $\Pr [Y_{\text{nd}} \geq \omega]$ is bounded as

$$\Pr [Y_{\text{nd}} \geq \omega] \leq \frac{2p_{\text{Tx}}\lambda\omega^{-\frac{2}{\alpha}}}{U(\alpha-2)} \int_0^\pi G(\phi)^{\frac{2}{\alpha}} d\phi. \quad (4.52)$$

Note that (4.52) has a singularity at $\alpha = 2$. This is in accordance with the fact that in theory, an infinitely large area filled with interfering nodes would cause infinite interference at the reference node for $\alpha = 2$.

The upper bound for the outage probability is then obtained by inserting (4.52) into (4.43),

$$p_{\text{out}} \leq p_{\text{out,d}} + (1 - p_{\text{out,d}}) \frac{2p_{\text{Tx}}\lambda\omega^{-\frac{2}{\alpha}}}{U(\alpha-2)} \int_0^\pi G(\phi)^{\frac{2}{\alpha}} d\phi. \quad (4.53)$$

4.4.3 Empirical verification

To create simulation results, specific values for the parameters must be chosen. In the following, the parameters for the wideband signal at 24 GHz are used, unless stated otherwise (see Section 3.6.2). An empirical verification of these bounds is obtained through the following Monte-Carlo experiment:

1. For every density λ , a radius R is chosen such that the average number of nodes satisfies $\frac{\lambda}{\pi} R^2 \geq 1000$, but the radius is not less than $R \geq 200$ m. For all simulations, the value λ is interpreted as average number of nodes per square meter.

2. A number \tilde{I} of interferers is randomly chosen from a Poisson distribution with mean parameter $\lambda\pi R^2$. Every interferer is assigned a random position x uniformly on the disc with radius R .
3. Out of these interferers, I are chosen randomly with probability p_{Tx} to act as active interferers.
4. The total interference power for this realization is thus

$$P_{\text{Ix}} = \sum_{i=0}^{I-1} \frac{\beta G(\angle x_i)}{\|x\|_i^\alpha}, \quad (4.54)$$

using β from (4.12).

5. If $P_{\text{peak}} < P_{\text{Ix}}$, this counts towards outage, otherwise, this is a detection. For every set of parameters, 10000 realizations are run to estimate the outage and detection probability.

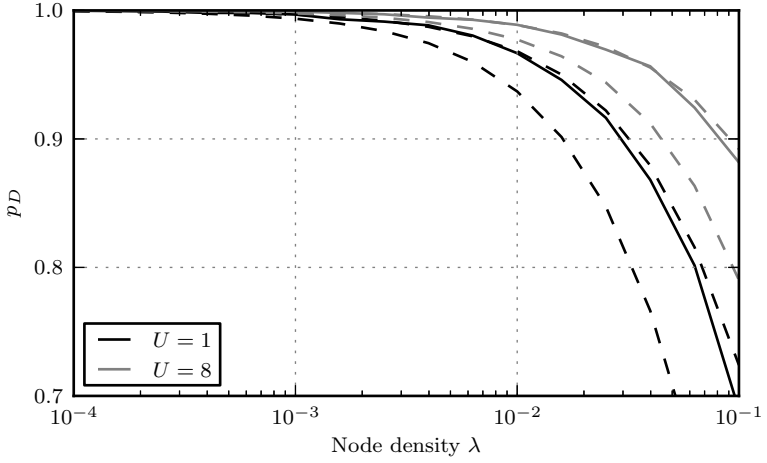
Fig. 4.4 shows some simulation results, together with the upper and lower bounds. Note that both p_D and p_{out} are displayed, as the detection rate is the more intuitive metric. Of course, the lower bound for p_{out} becomes an upper bound for p_D , and vice versa.

Two observations can be made: First, the bounds are correct. More importantly, the upper bound is very tight and can be used as a good approximation of the actual detection probability. This concurs with other research using stochastic geometry [115].

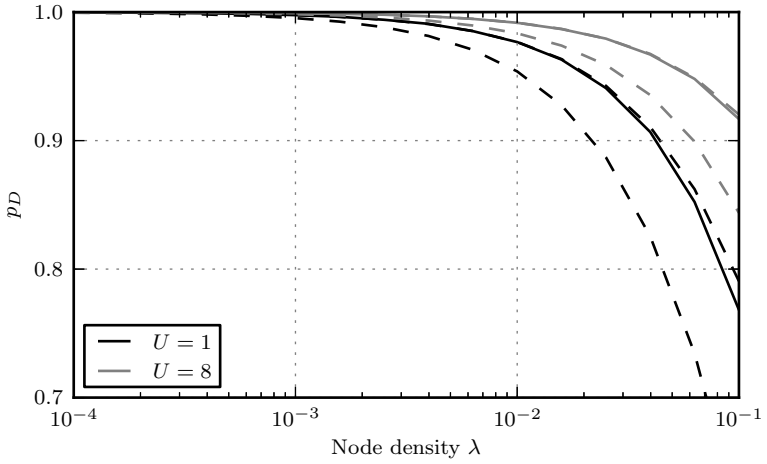
Fig. 4.6 shows the same simulation, but with a variation of α instead of λ . When α approaches 2, the overall interference increases, as nodes from further away become more and more influential. As before, the bound becomes less tight for higher interference levels.

4.5 Consequences for the system parametrization

Once useful bounds for the outage (or detection) probability are obtained, these can be used to evaluate an OFDM radar network. Two elements of the radar system are highlighted, which both gain significantly from the insights of the previous section: the target detection algorithm and the choice of the sub-carrier spacing.



(a) Cone-shaped antenna function



(b) Sinc-shaped antenna function

Figure 4.4: Empirical results for the detection probability (solid lines) and bounds (dashed lines) for $\alpha = 4$, $\phi_0 = \pi/2$ and varying node densities.

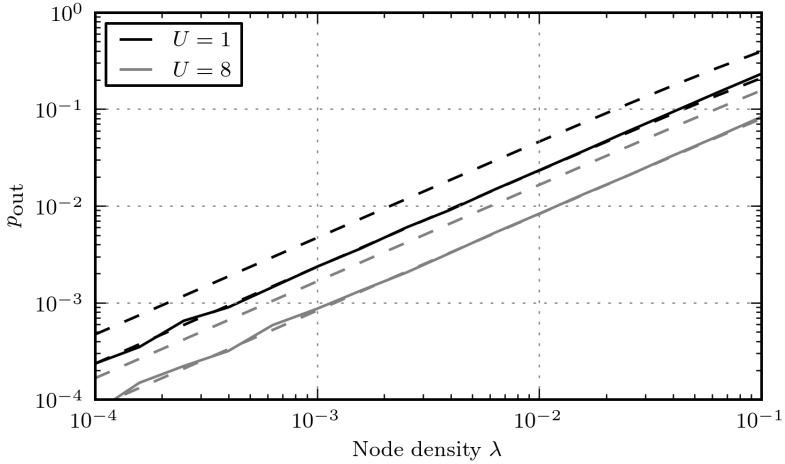


Figure 4.5: Empirical results for the outage probability (solid lines) and bounds (dashed lines) for $\alpha = 4$, $\phi_0 = \pi/2$, sinc-shaped antenna function and varying node densities.

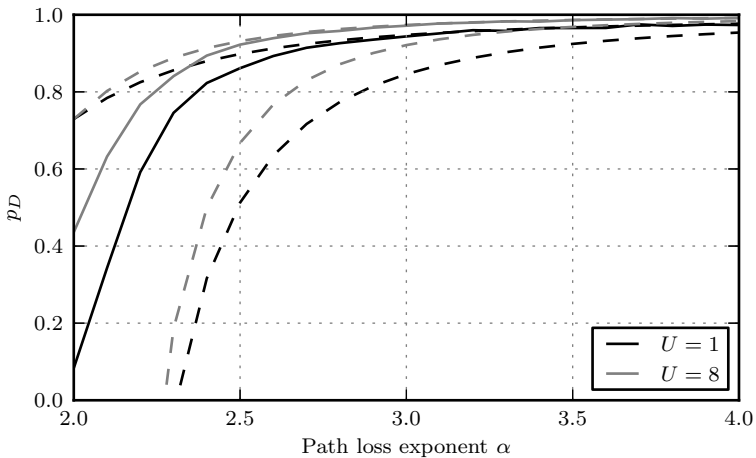


Figure 4.6: Simulated results (solid lines) and bounds (dashed lines) for $\lambda = 10^{-2}$, $\phi_0 = \pi/2$, sinc-shaped antenna gain.

4.5.1 Network feasibility study

The most obvious use for these new metrics is a feasibility check of a given radar network to determine whether or not a network would fulfill certain QoS requirements. Given a set of system parameters and a maximum expected node density, the bounds can be used for a quick check of the system's reliability.

As an example, consider the results from Fig. 4.4 and say that a detection probability of 99% is required for safety reasons. This means that the node density must not exceed $\lambda = 10^{2.2}$, which corresponds to one node per 158.5 m^2 on average. In a vehicular scenario, this corresponds to an average of one vehicle equipped with an OFDM radar system every 53 m for a lane width of 3 m, which seems realistic given that most likely, not all vehicles would be equipped with such a radar system. For other node densities, the corresponding detection probability can be read from Fig. 4.4. If the radar system must work with a specific detection probability at a higher node density, the parametrization can be changed in several ways: Either the number of channels U is increased, or ϕ_0 is reduced.

Of course, this also works conversely: given a node density λ , what kind of target can the radar detect with a given probability? To answer this question, the detection probability for different values of P_{peak} must be calculated. Fig. 4.7 shows p_D as a function of r_{Ref} (P_{peak} is recalculated for every value of r_{Ref} using (4.5), (4.1) and the values from Section 3.6). This time, the $P_{\text{Rx,Ref}}$ is reduced instead of increasing the average interference power.

Again, the bounds become less accurate for higher interference levels.

It is worth pointing out that this is analogous to the *outage capacity* of communication networks, which is a data rate that can be achieved with a given probability. Here, a target with peak amplitude P_{peak} can be detected with probability p_D .

So far, this could be achieved by simulations instead of using the bounds—although time-consuming, the results would be very similar. To show the benefits of using the lower bound for p_{out} as an approximation, (4.53)

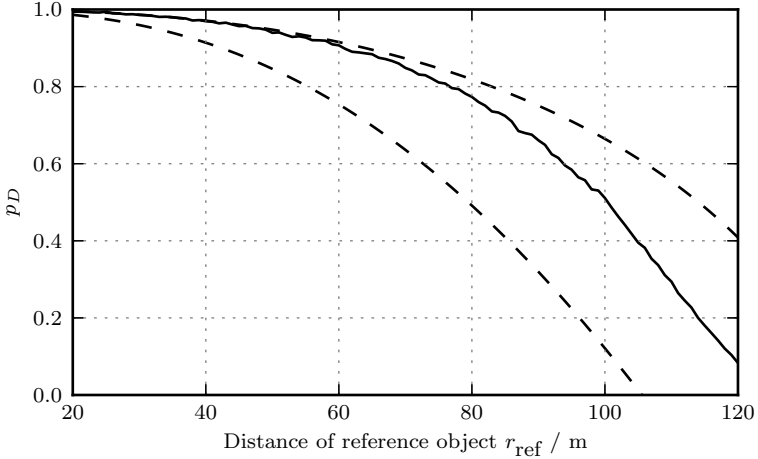


Figure 4.7: Detection probability over distance of the reference object. $\alpha = 3$, $\lambda = 10^{-2}$, sinc-shaped antenna gain with $\phi_0 = \pi/2$.

(cone-shaped antenna function, Rayleigh fading) is solved for λ :

$$\lambda(p_D) = \frac{-\log(p_D)U}{p_{\text{T}\times}\phi_0\omega^{-\frac{2}{\alpha}}\Gamma(1 + \frac{2}{\alpha})}. \quad (4.55)$$

This way, a maximum node density can be obtained from a given minimum tolerable detection probability. Using (4.55), the expected density of successfully detecting nodes ($p_D \cdot \lambda(p_D)$) can be plotted as a function of the required detection probability. Fig. 4.8 shows this value for different values of p_F .

This demonstrates how these simple bounds provide a powerful tool for benchmarking the network performance of an OFDM radar system, creating a powerful alternative to computationally expensive simulations.

4.5.2 Evaluation of the detection performance

The results from Section 4.4 assume perfect detection; i.e., the reference target is guaranteed to be detected when $P_{\text{peak}} > \eta$. In reality, a multi-

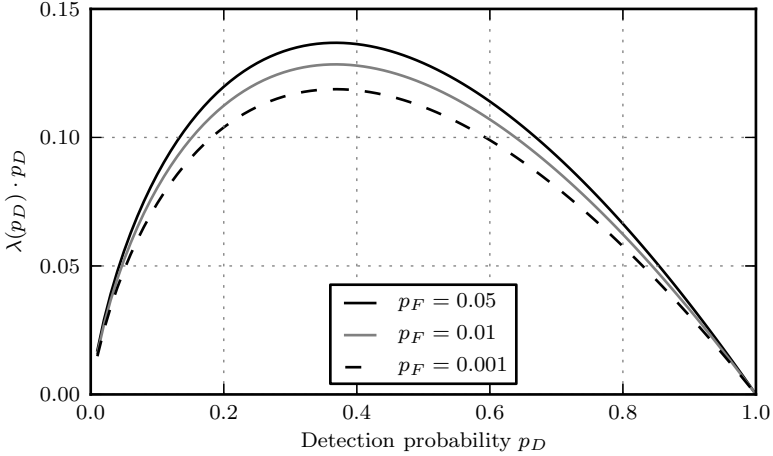


Figure 4.8: Using the lower bound for the outage probability to calculate (4.55). $\alpha = 4$, cone-shaped antenna function, Rayleigh fading.

target detection algorithm has to deal with more problems than just gauging the amplitude and position of peaks; it has to distinguish sidelobes from targets, handle the case where targets are very close and have overlapping main lobes, etc. Additionally, such algorithms often come with constraints regarding computational complexity. Multi-target detectors will therefore perform sub-optimally in most practical cases, and the bounds presented in this paper are a way of quantifying how much worse such an algorithm is compared to a perfect detector.

A *hypothetical* perfect detector could consist of the following steps:

1. Detect any peak larger than η in the periodogram.
2. Exactly (without *any* error) determine Doppler and range of the corresponding target.
3. Using these values, calculate the target's corresponding summand of (3.21) and subtract it from \mathbf{F} .
4. Re-calculate the periodogram with the updated value of \mathbf{F} .

5. Repeat from the beginning until no element of the periodogram exceeds η .

The second step makes it obvious that no such algorithm can be implemented. Fortunately, it is still possible to *simulate*: By creating a scenario where everything except the reference target has zero RCS, the reference target is therefore the only object reflecting the reference node's transmit signal. The interferers only produce interference noise, no radar backscatter.

The simulation works as follows: for every iteration, a number of interferers (and their positions) is modelled the same way as in Section 4.4.3. The reference node, as well as every active interferer node, transmits an OFDM frame. The signal of the reference node is attenuated according to (4.1) and delayed by $\tau = 2\frac{r_{\text{Ref}}}{c_0}$. The interference signals are attenuated according to their azimuth and antenna function as well as the path loss (with $\alpha = 4$). No small-scale fading was applied here, as this would introduce too many random effects for a meaningful simulation.

All signals (reflected reference signal and all interferer signals) and the thermal noise are added up and passed to an estimator that works as described in Section 3.3. A detection is considered successful if the periodogram bin corresponding to the reference target's distance and Doppler is larger than the threshold,

$$\text{Per} \left(\underbrace{\frac{r_{\text{Ref}}}{c_0} 2\Delta f N_{\text{Per}}}_{\text{Rounded to nearest integer}}, 0 \right) \underset{H_1}{\overset{H_0}{\gtrless}} \eta. \quad (4.56)$$

At every iteration point, 1000 iterations were run. Fig. 4.9 shows the simulation results. Note that at some points, the simulated curve actually exceeds the upper bound; this is because the method to estimate the detection probability by simulation has some variance, and the mean of the curve is supposed to be very close to the upper bound. This confirms that the approximation (4.5) is justified, as the simulated curves from Figs. 4.9 and 4.4 are very close to each other.

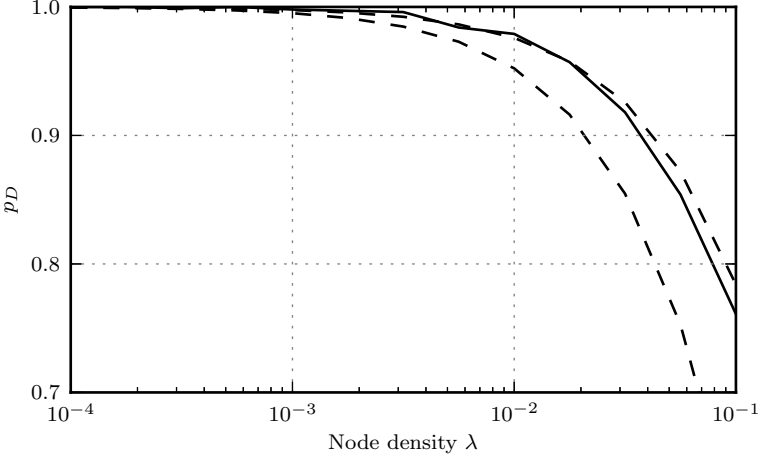


Figure 4.9: Simulation of the ideal detector ($\alpha = 4$, cone-shaped antenna function, $\phi_0 = \pi/2$, $U = 1$, no fading). The solid line shows the simulation results, the dashed lines the analytical upper and lower bounds.

Detector loss

In a realistic scenario, a practical multi-target detector algorithm will never achieve the performance of the hypothetical ideal estimator. Using the lower bound approximation, the loss incurred hereby can be qualified for a specific scenario: Given a density λ , assume a multi-target detector achieves a detection rate of p_D .

By solving the lower bound for $P_{\text{Rx,Ref}}$, an equivalent power can be calculated which would cause the ideal detector to yield the same detection rate:

$$P_{\text{Rx,ideal}}(\lambda) = \frac{c-1}{NM} \left(\left(\frac{-p_{\text{Tx}}\lambda\phi_0}{U \log(1-p_{\text{out}}(\lambda))} \right)^{\frac{\alpha}{2}} U\beta + \sigma_N^2 \right) \quad (4.57)$$

By comparing the received power with the reflected power of the refer-

ence object, a *detector loss* is defined as

$$L(\lambda) = \frac{P_{\text{Rx,ideal}}(\lambda)}{P_{\text{Rx,ref}}}. \quad (4.58)$$

4.5.3 Choice of sub-carrier spacing

In Section 4.1, the possibility of using a carrier spacing method ($U > 1$) to allow multiple user access to the medium was discussed. This has two effects: first, it decreases the chance of a collision, as different users may access the medium on different logical channels. On the other hand, whenever a collision occurs, the influence of the interfering signal is in fact worse than it were for $U = 1$, because the signal power per active carrier is increased by a factor U . Another way to understand this is by noticing that the processing gain is reduced by U . Intuitively, it is therefore not clear how the choice of U affects the multi-user performance.

These results provide a simple answer for this: consider the lower bound,

$$p_{\text{out}} \geq p_{\text{out,d}} = 1 - \exp\left(-\frac{p_{\text{Tx}}\lambda}{U}\omega^{-\frac{2}{\alpha}} \int_0^\pi G(\phi)^{\frac{2}{\alpha}} d\phi\right), \quad (4.59)$$

where U appears twice: once in the PPP density ($p_{\text{Tx}}\lambda/U$), and once in $\omega^{\frac{2}{\alpha}}$. The argument of the exponential function therefore depends on $U^{-(\frac{2}{\alpha}-1)}$. Because $\frac{2}{\alpha}-1 > 0$, the outage probability will always decrease for higher U , and this can thus be chosen as large as external constraints permit.

5

Radar performance verification

Chapters 3 and 4 consisted of a theoretical analysis of OFDM radar. To fully judge the performance of such a system, comprehensive simulations and measurements are also necessary to complement and confirm the theoretical results.

In order to perform these tests a suite of tools was developed which is presented in the next section. The results are presented in the rest of this chapter.

5.1 Simulation and Measurement Tools

To obtain the results in this chapter, a tool was developed in Matlab to perform both measurements and simulations. A modular design allows to switch easily between configurations, and all radar-related simulations and measurements in this chapter were performed with this tool.

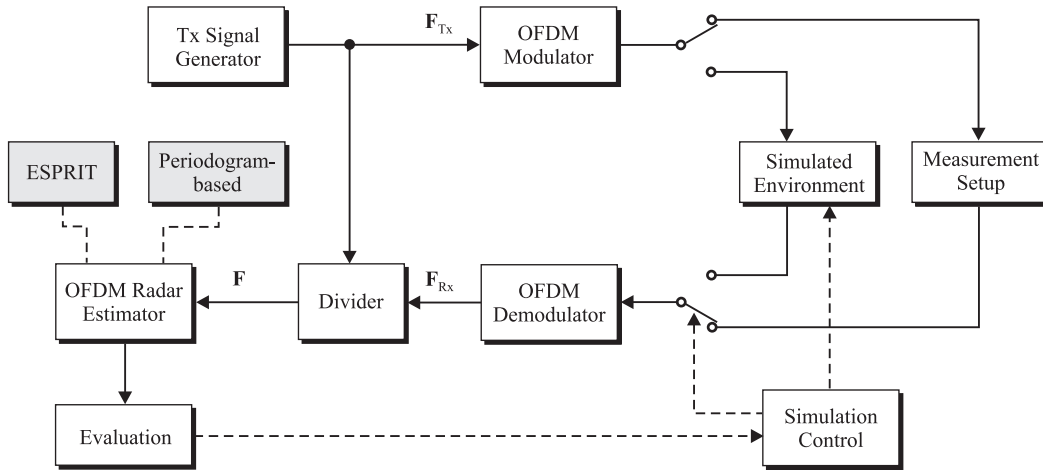


Figure 5.1: Schematic of the simulation and measurement system

Fig. 5.1 shows a schematic of the components. These shall be presented in the following.

5.1.1 Simulation Control

This component governs the execution of simulations. In order to run a simulation, a configuration file must be written which stores all the relevant parameters. A simulation is then launched by then executing this configuration file, which guarantees reproducibility of the tests.

Any parameter of the simulation can be changed, including

- Number of iterations per simulation
- Choice of the estimation algorithm
- OFDM signal parametrization
- Switching between live measurements and simulated environments
- Controlling the simulated environment (if applicable)

A feature worth pointing out is the ease of switching between measurements and simulations. When the computer running the tests is connected to the appropriate hardware (see Section 5.1.3), it takes a simple software switch to either run the measurements through a simulated environment or a real one.

Another responsibility of this component is to collate data during the simulations. As an example, the simulation control can repeatedly run a test with varying distances of a reference target. At every simulation point, the measurement can be repeated several times to obtain an average result, as was done in Section 5.2.1.

5.1.2 Simulated Environment

A central part of the simulation is a virtual environment. The simulation creates the transmit signal and then needs to calculate a received signal according to (3.12) (here including signals from interfering nodes),

$$r(t) = \sum_{h=0}^{H-1} b_h s(t - \tau_h) e^{j2\pi f_D \cdot h t} e^{j\tilde{\varphi}_h} + \sum_{k=0}^{I-1} i_k(t) + \tilde{z}(t). \quad (5.1)$$

In order to calculate $r(t)$, the simulation needs to know about the number of targets, their distance from and velocity relative to the radar, and RCS. Also, the OFDM signal parameters and hardware specifications need to be known to calculate the absolute Doppler shift, the attenuation b_h , and the noise power of $\tilde{z}(t)$. A full list of configurable parameters is given in the following.

Target List This component features two ways to generate targets: Either through a pre-determined list of targets, or random generation.

When generating targets randomly, upper and lower limits for range, velocity and RCS must be specified. Targets are then distributed uniformly within these limits.

Hardware settings The hardware is simulated by two parameters: the noise figure and the amount of direct coupling. Using the OFDM signal parameters, the actual noise power is calculated from the noise figure and signal bandwidth, an appropriate noise signal is then added to the received signal.

Direct coupling is generated by adding an additional target to (5.1) with $\tau = 0$ s, $f_D = 0$ Hz and b_h being equal to a user-defined value of isolation between receive and transmit antennas.

Clutter As discussed in Section 3.3.6, clutter and targets are indistinguishable for a medium-range OFDM radar system. In simulations, it still can be beneficial to introduce clutter to a simulation as an additional source of interference.

There are three differences between targets and clutter in this context: Firstly, clutter is always static (i.e. all clutter objects have the same relative velocity). Secondly, it is always generated randomly, with the range being uniformly chosen with a given maximum and minimum distance, and the RCS following an exponential distribution with a given mean. Thirdly, clutter is stored in a different memory from that of the targets. As an example, this can be used to simulate the detection probability p_D discussed in Chapter 4: The reference target is defined as the single relevant target, all other scatterers are defined as clutter. If clutter is detected by the radar system, the simulation controller can discard this

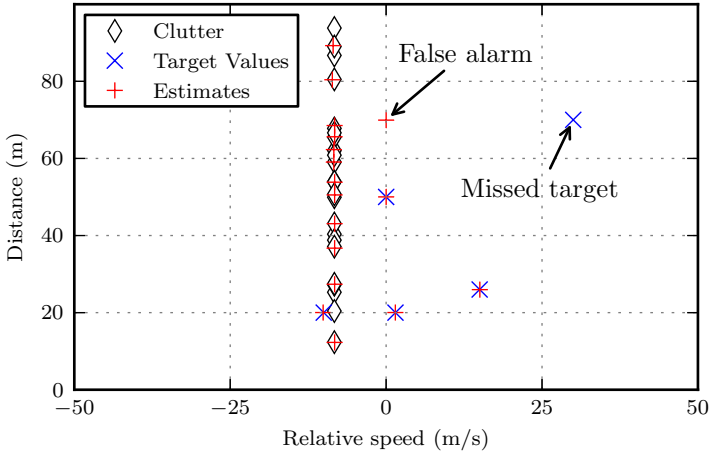


Figure 5.2: Example of auto-generated targets, clutter and estimator results

result, only focussing on the detection and estimation accuracy of the reference target.

Fig. 5.2 shows an example of what this can look like in a simulation. Multiple targets and clutter are created randomly (the radar system is defined to have a non-zero velocity, which is why the clutter all appears at a relative velocity of -8.3 m/s).

Interferers For network performance simulations, it is necessary to also simulate the signals from other, interfering nodes. This can be done by adding a list of interferer parameters, which include the attenuation between the individual interferer and its carrier offset. Oscillator inaccuracies can be included in the simulation, which results in a uniformly distributed, random frequency offset within a given limit.

5.1.3 Software Radio-based Measurement Setup

To perform live measurements, the simulated environment can be replaced by a measurement setup, which is presented in [8] and [7]. It uses a custom-built executable which connects to two Ettus Research N210 transceivers, one each for transmitting and receiving. Clocks are synchronized using a MIMO extension cable, which exports the clock from one device to the other and also allows to control both devices from one Ethernet connection.

The N210 is a programmable transceiver developed for software radio purposes, it can therefore transmit any waveform which can be synthesized digitally, as long as it does not exceed the maximum available bandwidth. USRP devices use interchangeable *daughterboards* for mixing and amplification; in order to transmit in the 5.9 GHz range, a XCVR2450 daughterboard was used, which uses a MAX2829ETN IC for mixing and filtering. The disadvantage of using this board is the limited bandwidth of 36 MHz, which is restricted by the available analog filters.¹

In software radio applications, the typical bottleneck for the bandwidth is the connection between host PC and USRP, in this case a gigabit Ethernet connection. For the radar measurement setup, this is not a problem, since the OFDM frames are uploaded to the N210's memory prior to transmission. The length of the OFDM radar bursts is then only limited by the size of the onboard RAM, which can hold 262144 complex samples at 16 bits of precision [7]. For an OFDM symbol size of $N_{\text{total}} = 64$, this corresponds to 4096 OFDM symbols, which is more than any of the parametrizations in Section 3.6 requires.

To reduce direct coupling, two highly directive horn antennas were used with an antenna gain of 15.6 dBi, identical to those in [18].

Compared to the measurement setup described in [14], the software radio-based setup has many advantages. The power consumption is much less, and both host PC as well as the USRPs can be battery-powered for several hours. The smaller form factor allows for higher mobility and more flexibility when choosing the locations for the measurement. Also, as the measurement setup is tied into the OFDM radar testing suite, any

¹The MAX2829 IC has integrated filters [74], which means the filters cannot be easily modified.

modifications to the radar estimation code can directly be tested in both measurements and simulations.

The clear disadvantages are the available bandwidth and frequency range. Without designing a custom daughterboard, the 24 GHz parametrization cannot be tested with this setup, although the 802.11a parametrization can.

Fig. 5.3 shows the measurement setup. At the top, all the components for a measurement setup are shown. The bottom picture shows an example of how this measurement setup can be deployed in the field.

Several proof-of-concept measurements were performed to verify the general applicability of both the 802.11a waveform for radar as well as the functionality of this setup.

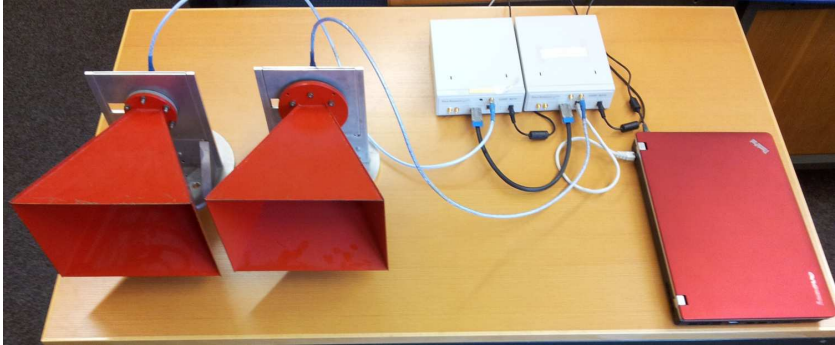
To test the usability of roadside base stations using 802.11a signals as radar sensors, the testing rig was set up above a motorway.² The antenna beam was wide enough to cover all four lanes in both directions.

Fig. 5.4 shows a photograph of a typical traffic situation on this road, as well as the corresponding periodogram and detection list. The results are promising: On every lane, there is one vehicle which is detected. The velocity of the oncoming truck (vehicle 4 in Fig. 5.4a) was estimated at approx. 82 km/h, which is consistent with the legal driving speed of such trucks. The size of both trucks causes artefacts in the periodogram, however, which are translated into detections. Given the small amount of power associated with these artefacts, it is a reasonable assumption that additional post-processing and target tracking will eliminate them.

5.1.4 Radar Estimator

The estimator is designed to be an interchangeable component. An API is provided to implement various estimators using the radar processing matrix \mathbf{F} and the OFDM signal parameters. For the experiments in this chapter, two estimators were used, the periodogram-based and the ESPRIT-based estimators. However, it is a simple task to implement other estimators.

²On top of a bridge across the B9 near Kuhardt.



(a) The components of the measurement setup: Two USRP N210, connected via MIMO cable, horn antennas, host PC.

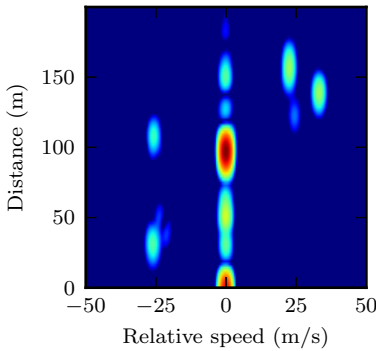


(b) Performing measurements in the field: The USRPs' power supply is a 12 V battery; DC/DC converters provide the required 6 V supply voltage.

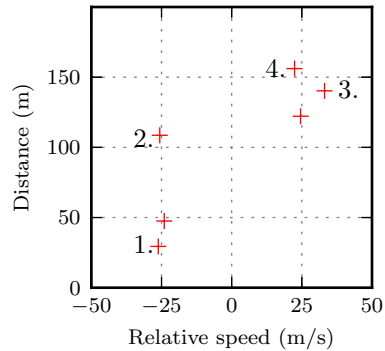
Figure 5.3: Measurement hardware for the OFDM radar testing suite.



(a) Traffic scenario on the B9 motorway.



(b) Corresponding periodogram.



(c) Detection results.

Figure 5.4: Measurement and results using the SDR-based measurement rig. The target detector was configured to ignore stationary targets. All four vehicles are detected.

Estimator-specific settings are also parametrized from the configuration file. For the periodogram-based estimator, the following settings are available:

- Window function
- Interpolation algorithm (see Section 3.3.5)
- Multi-target detection algorithm (see Section 3.3.7)
- False alarm rate
- Noise power value (either per estimation or by using the known, correct value)

For the ESPRIT-based estimator, the following settings are available:

- Estimation order (it is possible to pass the estimator the actual number of targets automatically)
- Size of auto-correlation matrix

5.1.5 Evaluation

The simulation tools include algorithms to evaluate the estimation results. Using the output of the estimator, the following metrics are automatically calculated:

- Range and velocity error for every target detected
- Relative range and velocity error for every target detected
- Average RMS error for range and velocity
- Number of non-detected targets
- Number of false alarms

As discussed in Section 5.1.2, the evaluation system has a way to distinguish targets from clutter. This is done by passing a list of targets and clutter objects to the evaluation function. For every target detected, the following steps are performed:

1. For the i -th estimate, find the object with the smallest Euclidean distance in the range/Doppler plane from the list of targets and clutter objects.

2. If the distance between estimate and object lies within a pre-defined tolerance,

$$\frac{\hat{v}_{\text{rel},i}}{v_{\text{rel,tol}}} + \frac{\hat{d}_i}{d_{\text{tol}}} \leq 1. \quad (5.2)$$

If yes, this counts as a detection. Remove that object from the list to avoid finding it again. If no, this counts as a false alarm; continue at 1).

3. Calculate the absolute and relative errors for this target,

$$\Delta_{\text{abs}}d_i = \hat{d}_i - d_i \quad (5.3)$$

$$\Delta_{\text{rel}}d_i = \frac{\hat{d}_i - d_i}{d_i} \quad (5.4)$$

$$\Delta_{\text{abs}}v_{\text{rel},i} = \hat{v}_{\text{rel},i} - v_{\text{rel},i} \quad (5.5)$$

$$\Delta_{\text{rel}}v_{\text{rel},i} = \frac{\hat{v}_{\text{rel},i} - v_{\text{rel},i}}{v_{\text{rel},i}} \quad (5.6)$$

Fig. 5.2 has an example for this: The top right target is too far from any estimate, so it is considered a missed target. An estimate at the same distance, but with different relative velocity, is outside the tolerance range, of any existing target or clutter, and is thus considered a false alarm. For further evaluation, only the four estimates are considered which were matched to actual, existing targets. Any estimate coinciding with a clutter object is discarded.

5.2 Single-node radar performance

This section is dedicated to analyzing the performance of a single radar system in the absence of any interferers.

Parametrization

A note on the chosen parameters: Unlike the previous chapters, where the parametrization was only relevant in very few cases, a choice must be made for the parameters to run the simulations and measurements.

Transmit power	$P_{\text{T}_x} = 20 \text{ dBm}$
Antenna gain	$G = 0 \text{ dB}$
Noise figure	$\text{NF} = 5 \text{ dB}$
Maximum distance	$d_{\text{max}} = 400 \text{ m}$
Maximum velocity	$v_{\text{rel,max}} = 150 \text{ m/s}$
Periodogram dimensions	$N_{\text{Per}} = 4N, M_{\text{Per}} = 4M$

Table 5.1: Hardware- and estimator related simulation parameters

Unless stated otherwise, the parametrizations used here are those presented in Section 3.6. For sake of brevity, they will be referenced as *wideband* and *802.11a* signals. Similar results (albeit with slightly different parameters) were first presented in [6].

For the parameters of the simulation setup, the values from Table 5.1 were chosen as default values. Most notable is the antenna gain, which is left at 0 dB. This choice was made to provide worst-case results without having to specify the antenna. In a practical setup, the antenna gain will increase the backscattered energy available at the receiver for any target in the main beam of the antenna, thus improving the results.

5.2.1 Single-target accuracy

The first results are created by simulating the case where there is only one valid target, and no clutter. The signal processing matrix thus only consists of the sinusoids corresponding to this target and AWGN, as in (3.20):

$$(\mathbf{F})_{k,l} = b_0 e^{j2\pi l T_O f_c \frac{2v_{\text{rel},0}}{c_0}} e^{-j2\pi k \frac{2d_0}{c_0} \Delta f} e^{j\varphi_0} + (\mathbf{Z})_{k,l}. \quad (5.7)$$

In all of these simulations, results were calculated for a value of $d_0 = 10 \text{ m}$ up to $d_0 = 400 \text{ m}$, increasing the distance in steps of 1 m. At every value of d_0 , 10000 iterations were run. In one iteration, the transmit matrix \mathbf{F}_{T_x} , the noise \mathbf{Z} and phase φ_0 were generated randomly. The attenuation b_0 was calculated from the current value of d_0 according to (3.13). This creates a unique value of the SNR at every distance. Note that this affects the results, as the estimation quality depends on the SNR, which is in turn a function of the distance (the quantity to be estimated).

The velocity was chosen randomly from a uniform distribution within the interval $[\frac{-c_0}{2 \cdot 2f_c T_O M_{\text{Per}}}, \frac{c_0}{2 \cdot 2f_c T_O M_{\text{Per}}}]$ for every iteration. This interval is the size of one bin in the periodogram, and ensures that quantization errors will be visible in simulation results.

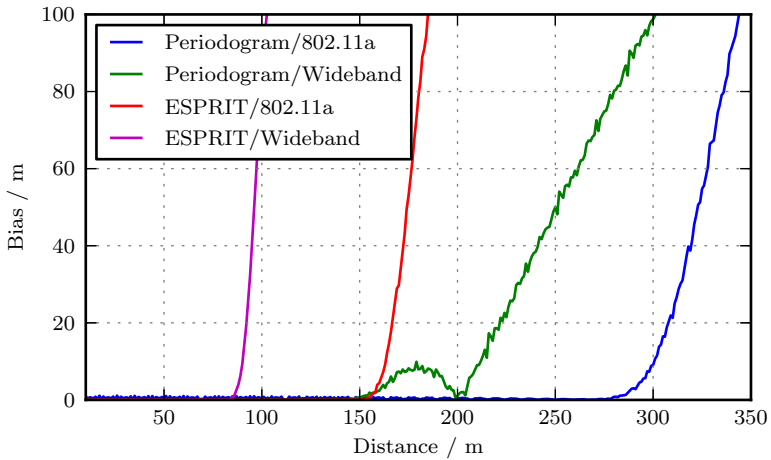
Because only one target was active, there was no need to implement a multi-target detector. Instead, the largest peak of the (cropped) periodogram was chosen as the estimate. This will highlight the need for a threshold and demonstrate the previously discussed threshold effect.

Results are shown in Figs. 5.5 and 5.6. Two observations concerning the estimation characteristics are to be made: First, the threshold effect previously discussed is clearly visible. Beyond a certain distance, SNR becomes too low for the radar system to recognize the target reliably. This motivates the choice of a threshold to discriminate noise from peaks caused by targets. Second, the bias for the range estimate is not constant for distances smaller than the threshold. This is caused by quantization errors as described in Section 3.3.5.

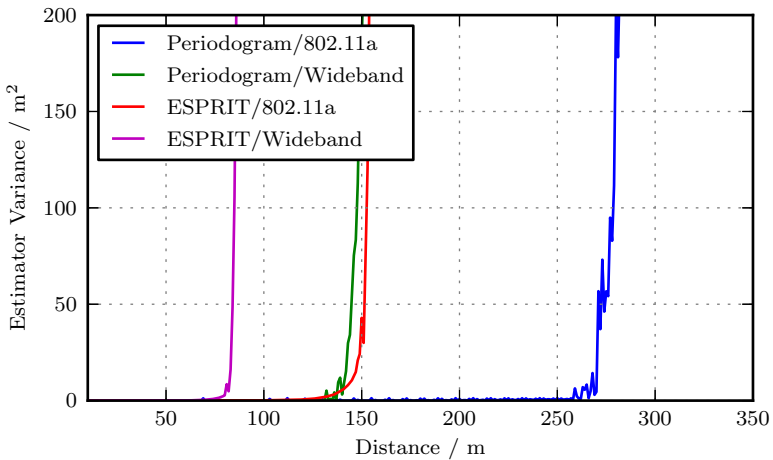
The ESPRIT-based estimator does not exhibit this quantization error. However, the threshold is lower for the parametric approach. The threshold is also lower for the wideband signal compared to the 802.11a signal. This has two causes: The higher centre frequency of the wideband parametrization causes higher free space path loss, and the higher bandwidth causes a higher total noise power.

The bias for the wideband signal exhibits a brief decrease around 200 m. This is because d_{max} was chosen as 400 m here, an estimator which randomly chooses a distance uniformly between zero and d_{max} thus has a mean estimate of 200 m. The estimation starts to deteriorate at around 150 m, which is more evident from Fig. 5.5b. Similarly, note that the bias for the velocity estimate is not shown. In these simulations, it is not a meaningful metric, because the mean value for the true velocity is zero. The worst case for the estimator is when the velocity is randomly estimated from within $[-v_{\text{max}}, v_{\text{max}}]$, which also has a mean value of zero.

The quantization errors are removed when using an interpolation algorithm. Figs. 5.7 and 5.8 show the same simulation using the periodogram, but with the quadratic interpolation and the interpolation by optimization. The y-axes are scaled in order to highlight the errors at shorter distances.



(a) Estimation bias.



(b) Estimation variance.

Figure 5.5: Estimation bias and variance as a function of the distance.

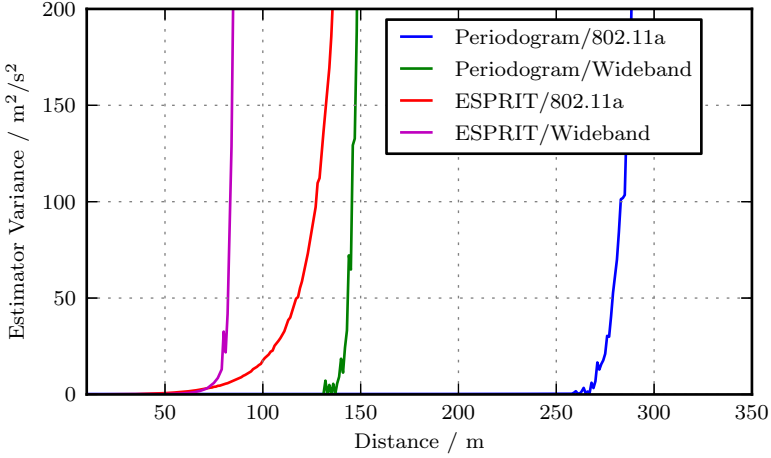
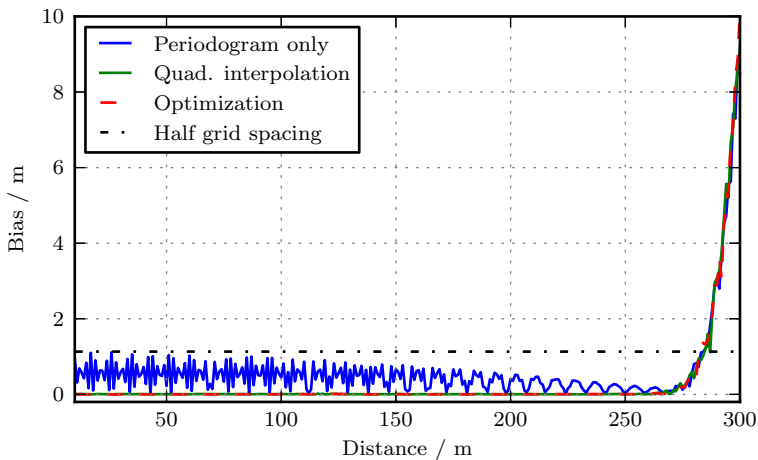


Figure 5.6: Estimation variance for the velocity estimate

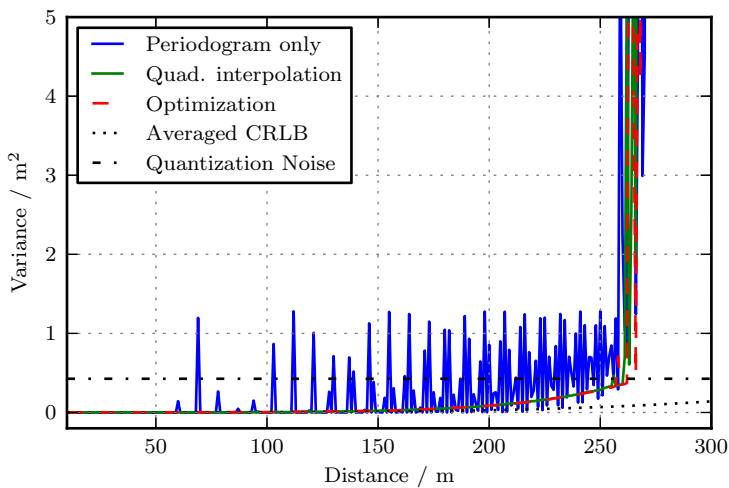
Several effects can be observed: When no interpolation is used, the quantization error is clearly visible. For the distance estimate, this can best be seen in Fig. 5.7a. Because the distance is not random, the estimation error is also deterministic and bounded by half the grid distance,

$$\max[\text{bias}[d]] = \frac{c_0}{2 \cdot 2N_{\text{Per}}}. \quad (5.8)$$

The variance of the velocity estimate also shows the quantization effect. At small distances, when detection is reliable, the variance is dominated by the quantization error (the velocity is chosen randomly and independently of the distance). The averaged CRLB (see Section 3.3.3) is also shown. It can be seen that the interpolation by optimization approaches this bound in all scenarios for smaller distances. The quadratic interpolation lies between the optimization approach and the quantized solution. Note that quadratic interpolation is a very simple method, as it consists of solving few equations with only basic mathematical operations. The optimization algorithm takes a non-deterministic number of steps to converge; the simulations for the optimization approach were between two and three times slower than those using quadratic interpolation. On hardware platforms or FPGAs, such an algorithm is therefore much more



(a) Estimation bias.



(b) Estimation variance.

Figure 5.7: Estimation bias and variance as a function of the distance with interpolation.

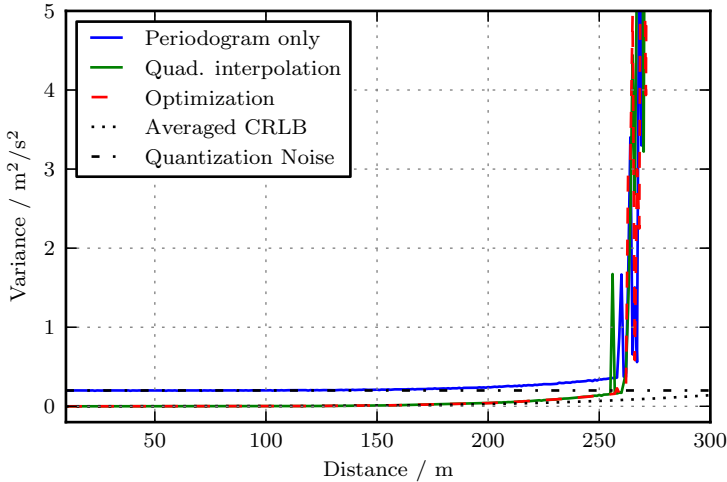


Figure 5.8: Estimation variance for the velocity estimate with interpolation.

difficult to implement.

There is another disadvantage of the optimization approach which is not quite as obvious: The interpolation algorithm may not converge correctly, introducing a new source of errors. In any case, the empirical results indicate that even though this approach is closer to the true MLE, it is not significantly better than the quadratic interpolation, which suggests the latter as the method of choice for reducing quantization errors.

As indicated above, both interpolation algorithms also cause the estimation error distribution to become Gaussian. As discussed in Section 3.3.5, this allows the use of tracking mechanisms which require the initial error to be normal distributed.

Fig. 5.9 shows the distribution of estimation errors for the velocity estimate in the range between 150 and 200 m. In this range, the estimation quality slowly starts to deteriorate. Two pdfs of normal distributions are also shown, with zero mean and the same variance as the quantized periodogram result and the quadratic interpolation result, respectively (the optimization approach is very close to the quadratic interpolation,

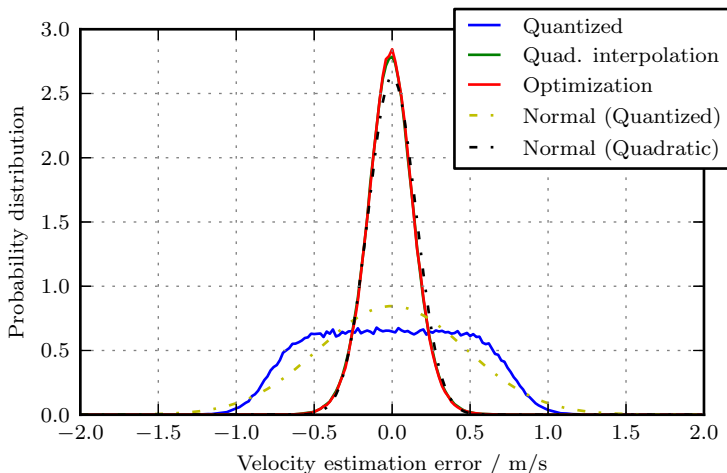


Figure 5.9: Relative frequencies of estimation errors and equivalent normal distributions

it is therefore not considered separately). It can be seen that the normal distribution is very close to the interpolated result, while the quantized periodogram produces an error distribution closer to a uniform one.

To complement the simulation results, measurements were performed using the setup described in Section 5.1.3. In this setup, the target consisted of a single vehicle placed on a sparsely occupied parking lot. The vehicle was placed at different ranges, with the driver's door facing the radar setup at the specified distance of 30, 40, 50, 70, 90 and 110 m. The results are shown in Fig. 5.10.

There are some major differences between the models chosen in the simulation and the real measurement: First, the hardware itself causes a signal delay, which will in turn cause a constant offset of the range estimate. This can be rectified by calibrating the range estimate. In the measurements presented here, the measurement at 30 m was used for calibration (and hence has zero measurement error).

Furthermore, a vehicle is not a point scatterer, especially at close distances. The true distance is therefore not necessarily a single range, as

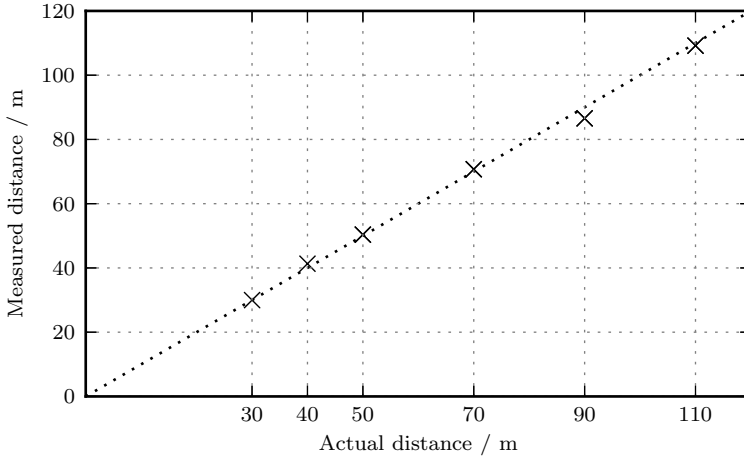


Figure 5.10: Measurement results using the 802.11a parametrization and the SDR-based setup

the scattered signal will consist of several reflections. Nevertheless, the results are promising and confirm that 802.11a based signals are usable for radar applications.

5.2.2 Multi-target accuracy

The previous results used a single target to evaluate the performance of the estimation process, but are not indicative of the performance of an OFDM radar system in a practical setup, where there are always multiple targets (including clutter). First of all, a realistic setup would use a threshold to discriminate between noise and targets, so the threshold effect is no longer an issue. Furthermore, a multi-target detector must be implemented as described in Section 3.3.7.

When simulating multiple targets, the chosen metric for the evaluation of the radar accuracy is the root mean square (RMS) error of the estimates for d and v_{rel} . To gauge the quality of the multi-target detector, the number of correctly estimated targets is compared is chosen.

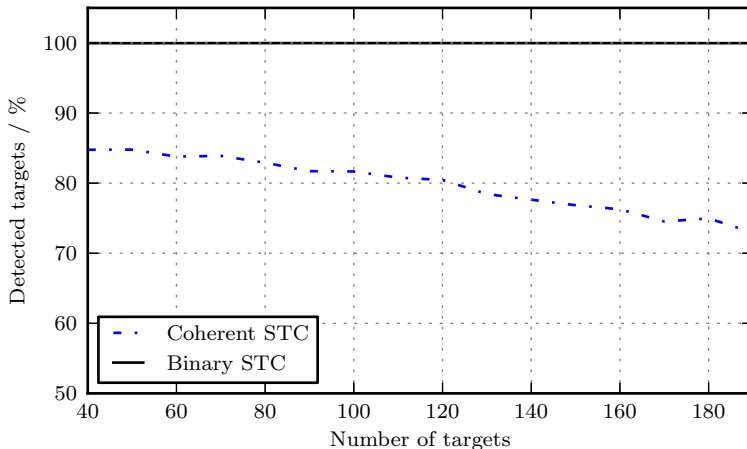


Figure 5.11: Detection rates for binary and successive target cancellation

Fig. 5.11 shows a comparison of the binary and coherent target cancellation algorithms. The wideband signal was used for simulations. In every iteration, a fixed number of targets was randomly distributed such that the minimum possible distance between two targets was 10 m in range and 10 m/s in velocity. Furthermore, the area was restricted to a maximum distance of 220 m and a maximum relative velocity of 10 m/s. These values are chosen such that no two targets are closer than the resolution allows, and no target is so far away that it cannot be detected due to the amount of backscattered energy. Shadowing effects were not considered, i.e. a target located directly behind another will still backscatter its full energy to the radar receiver.

The results are promising: In both cases, the percentage of targets detected remains above 70%. The binary target cancellation algorithm clearly outperforms the coherent algorithm, staying close to 100% for all numbers of targets. The reasons are twofold: First, the experiment was geared towards the binary algorithm, since it assumes that no two targets are within the radar resolution. This is not something that can be expected in reality (although the large number of targets may also be considered unrealistic). The second reason the binary algorithm is

better is its increased robustness. The weak spot of the coherent target cancellation algorithm is the assumption that the estimation is without errors. Any error in the estimation process will therefore lead to residuals, which need to be handled separately as discussed in Section 3.3.7. In some cases, a large number of residuals can be created for a single target and since every detection (residual or true target) modifies $\text{CPer}_{\mathbf{F}}(n, m)$, the subsequent iterations are also affected. This can cause situations where the algorithm will simply fail to estimate more than a certain number of possible targets due to algorithmic instability.

The binary successive target cancellation algorithm does not have this problem: It is always stable since a detection will only occur once within the main lobe area. This also makes the binary variant more predictable in terms of processing time.

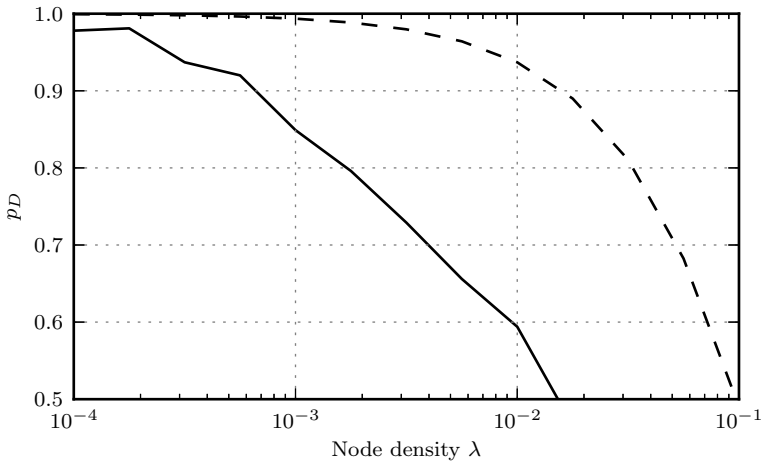
5.3 Multi-node performance

When operating in a network, interference signals from other nodes affect the performance of the radar system. As discussed in Chapter 4, this is perceptible as an increase of noise.

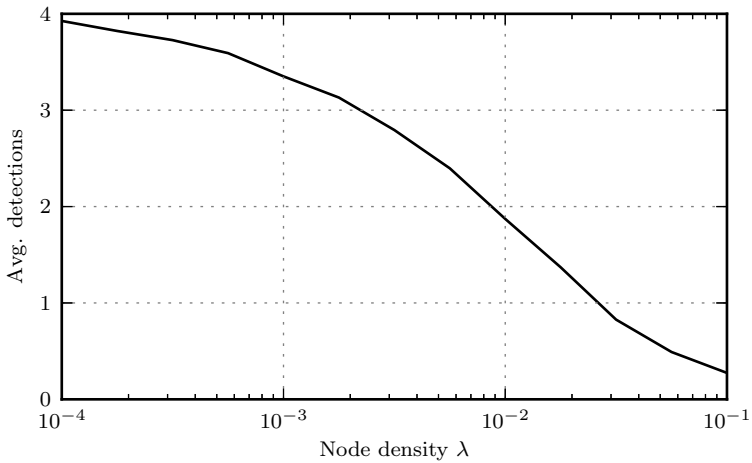
The metric to evaluate the degradation of the radar is the previously introduced outage probability. Section 4.5.2 already gave preliminary results for the case of ideal detection, which are shown in Fig. 4.9. As discussed, this result suggests the suitability of the derived bounds, but the simulation does not encompass all effects encountered in live experiments.

To create more realistic results, the simulation is modified as follows: Every interferer is assigned a random RCS which obeys an exponential distribution with pdf $p(\sigma_{\text{RCS}}) = \frac{1}{\sigma_{\text{RCS},m}} e^{-\frac{\sigma_{\text{RCS}}}{\sigma_{\text{RCS},m}}}$, $\sigma_{\text{RCS}} > 0$. The mean RCS was chosen as $\sigma_{\text{RCS},m} = 10 \text{ m}^2$. Instead of an ideal detector, the coherent STC method is used to detect and distinguish targets.

Furthermore, three additional static objects were included close to the first: Two at the same distance of 50 m, but with relative velocities of 10 m/s. Another object is placed at a 70 m distance, with the same relative velocity of 0 m/s as the first reference target. This resembles a typical traffic scenario, with opposite lanes and overtaking vehicles.



(a) Detection probability of main reference target and upper bound (dashed line).



(b) Average number of detected targets (out of four).

Figure 5.12: Simulation using the cancellation algorithm ($\alpha = 4$, cone-shaped antenna, $\phi_0 = \pi/2$, $U = 1$, no fading).

The results for the detection probability of the main reference target in this scenario are shown in Fig. 5.12a. A *significant* reduction of the detection probability compared to the ideal detector can be observed, although it must be noted that for higher node densities, the detector is forced to handle several hundred clutter objects (the interferers), which is a difficult task for radar systems in general. The root mean square (RMS) error of the estimation was also measured during the simulations, but as a successful detection is a prerequisite of calculating an error, the RMS error constantly stayed below 0.6 m for the range and below 0.6 m/s for the Doppler estimation.

The number of correctly detected targets out of the four static targets is shown in Fig. 5.12b.

From these results, the detector loss for this scenario can be determined. For a value of $\lambda = 10^{-3}$, the detection rate is $p_D = 0.85$ in the cancellation scenario. Using (4.57), the equivalent power for an ideal detector can be calculated as -127 dBm, or 18 dB lower than the reference power.

It is emphasized that while this quantification of detector loss can be useful for testing detection algorithms, it is only valid for a fixed scenario.

6

Conclusion

To conclude this work, the major contributions shall be recapitulated. A brief discussion of possible applications will then wrap up this thesis.

6.1 Contributions

While the basic principle of OFDM radar and the processing methods had been presented in the past (mainly by Garmatyuk and Sturm), a comprehensive theoretical analysis of the radar processing methods was lacking. In Chapter 3, the algorithm presented by Sturm is given a sound theoretical foundation and the estimation process for range and velocity of targets is analyzed.

By drawing the connection to spectral estimation, methods for the estimation of line spectra can be modified to be applicable here. Using from spectral estimation theory, an alternative radar imaging algorithm was derived, based on the ESPRIT method for line spectra estimation, although it is shown that this does not scale well with the number of targets, and is considered impractical for live implementations.

The focus was therefore on the periodogram method. Besides the aforementioned estimation theoretic analyses, implementation aspects were discussed as well as methods to combat quantization-related effects.

The choice of a suitable signal parametrization was also discussed. Unlike previous efforts to derive criteria for the suitability of parameters (such as the sub-carrier spacing or the frame structure), *both* communication and radar requirements were considered. It is evident that every subsystem has different requirements towards the waveform, in some cases even competing ones. Using these new insights, two parametrizations were evaluated: a custom, wideband waveform, and the commonly available IEEE 802.11a waveform.

Chapter 4 extends the theoretical analyses to radar networks. Here, the *radar network outage probability* is suggested as a novel metric for their performance, which is a new angle of approach to a field of research otherwise dominated by empirical methods. Using insights from stochastic geometry, it is possible to derive tight bounds for the outage probability, which can be used as a good approximation. Obtaining such metrics through empirical methods is cumbersome, and can now be avoided.

To validate these results, Chapter 5 provides simulation and measurement results to corroborate the theoretical results from the previous chapters. The implementation of an OFDM radar system on a software defined radio platform is also discussed.

6.2 Future Applications

Despite several suggestions since the early 2000s, OFDM radar has never been commercialized until very recently [47]. However, the results obtained in this thesis and other works do suggest that OFDM is a viable option, and can compete with other types of radar.

The dual usability for both communication and radar without having to sacrifice the functionality of one system in order to improve the other is a new aspect and an advantage of OFDM as a radar waveform. Since spectrum is considered more and more to be a scarce resource, the idea of re-using it for more than one application is attractive. Using the signal processing methods described in Chapter 3, *any* OFDM transmitter can be considered a radar beacon. The example of IEEE 802.11a signals was

covered in this thesis, although other examples such as OFDM-based broadcasting signals have been suggested as passive radar beacons [37, 48].

Automotive networks can also benefit from this technique, since they combine the fields of VANETs and radar. Researching mobile networks of combined radar and communications asks for new theoretical insights such as the radar network outage. The results here might therefore be one of many steps towards a theory of radar networks.

A

Influence of modulation schemes with variable amplitude

In the calculation of the radar processing matrix \mathbf{F} , the noise component is affected by the division by the transmitted data,

$$(\mathbf{Z})_{k,l} = \frac{(\tilde{\mathbf{Z}})_{k,l}}{(\tilde{\mathbf{F}}_{\text{Tx}})_{k,l}}. \quad (\text{A.1})$$

To understand the effect of this division on the noise, consider how phase and amplitude of a single element of \mathbf{Z} ($z = (\mathbf{Z})$), is affected by division with a single complex modulation symbol c . Both are split into amplitude and phase components,

$$z = b_z e^{j\varphi_z} = \frac{b_z e^{j\varphi_z}}{b_c e^{j\varphi_c}}. \quad (\text{A.2})$$

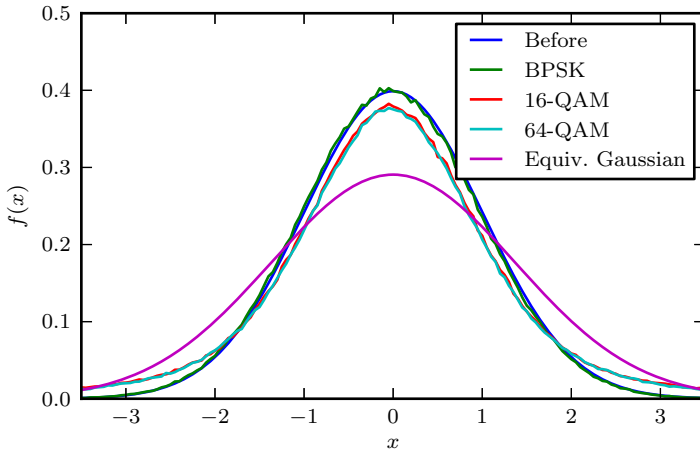


Figure A.1: Estimated PDFs of noise after division with different modulation schemes

First, the phase is considered. As $\tilde{\mathbf{Z}}$ was complex, circular Gaussian noise, φ_z is uniformly distributed within $[0, 2\pi)$. Adding or subtracting a random phase will not change the statistics of the noise's phase.

For the amplitude, things are different. Only if c is a symbol from a PSK alphabet, then $b_c = 1$, and the amplitude is unchanged. For phase-amplitude modulation alphabets this can be problematic, as the symbol's amplitude varies within several, discrete steps, and therefore the PDF if z is non-Gaussian.

Fig. A.1 shows the PDF of the amplitude of $(\mathbf{Z})_{k,l}$ obtained through simulation. It is generated by plotting the histograms of amplitudes of $\tilde{\mathbf{Z}}$ after dividing it by random symbols from diverse modulation alphabets.

Two effects can be observed: First, BPSK indeed does not affect the noise's statistics, and second, the PDF of b_z is clearly not Gaussian for higher modulation alphabets. Also shown is a Gaussian distribution which has the same variance as the noise after the division with the 16-QAM symbols. This is the noise distribution a radar system will assume

is correct (e.g. for the threshold calculation in 3.93). For the radar system, this means that effectively, a 16-QAM modulation will increase the noise when compared to BPSK/QPSK (by approx. 2.7 dB).

Since the Gaussian distribution has the highest entropy for a given variance, it can be seen as a worst-case assumption. For the radar system, this means that the simplest solution is to ignore the problem and always work with the Gaussian assumption. Any other solution would require the radar system to know which modulation scheme was used, which was never a requirement.

For higher modulations, this means that the noise power estimation will slightly overestimate the noise power, and consequently will place the threshold higher than necessary, which in turn can decrease the detection rate.

In practice, this is not a big problem. The signal parametrizations suggested in Section 3.6 always use BPSK for the wideband signal, and only uses 16-QAM or higher for IEEE 802.11a if the SNR is high enough to warrant this kind of modulation (besides, the transmitter decides the modulation scheme and does not have to choose anything higher than 8-PSK in any case). In the rare cases where higher modulations are used, the slightly reduced detection rate is a smaller price to pay than the increased complexity due to having to re-calculate the threshold for different modulations.

B

Quadratic Interpolation

To interpolate the true peak position of a target in a quantized periodogram with quadratic interpolation,¹ the peak of the window function is approximated by a two-dimensional parabola, which touches five supporting points: The point $\text{Per}_{\mathbf{F}}(\hat{n}, \hat{m})$, which is a local maximum corresponding to a target's peak (\hat{n}, \hat{m} are the integer indices of the peak in the periodogram), and the four adjacent points, $\text{Per}_{\mathbf{F}}(\hat{n} \pm 1, \hat{m})$ and $\text{Per}_{\mathbf{F}}(\hat{n}, \hat{m} \pm 1)$.

Without loss of generality, a coordinate-shifted periodogram is created from $\text{Per}_{\mathbf{F}}(n, m)$ which has the peak value at its origin,

$$\check{\text{Per}}_{\mathbf{F}}(\check{n}, \check{m}) = \text{Per}_{\mathbf{F}}(\check{n} + \hat{n}, \check{m} + \hat{m}). \quad (\text{B.1})$$

The parabola is denoted as $g(\check{n}, \check{m})$ and takes the form

$$g(\check{n}, \check{m}) = a_n(\check{n} - \check{\check{n}})^2 + a_m(\check{m} - \check{\check{m}})^2 + \check{\text{Per}}_{\mathbf{F}}(\check{\check{n}}, \check{\check{m}}), \quad (\text{B.2})$$

¹Also known as biquadratic interpolation, as it interpolates a two-dimensional periodogram

where a_n and a_m are the gradient parameters for the parabola, and $\check{\check{n}}$, $\check{\check{m}}$ and $\check{\check{\text{Per}}}_{\mathbf{F}}(\check{\check{n}}, \check{\check{m}})$ are the sought-after interpolated values.

From the five supporting points, an equal number of equations can be formed:

$$\check{\check{\text{Per}}}_{\mathbf{F}}(-1, 0) = a_n + 2a_n\check{\check{n}} + a_n\check{\check{n}}^2 + a_m\check{\check{m}}^2 + \check{\check{\text{Per}}}_{\mathbf{F}}(\check{\check{n}}, \check{\check{m}}) \quad (\text{B.3})$$

$$\check{\check{\text{Per}}}_{\mathbf{F}}(0, -1) = a_m + 2a_m\check{\check{m}} + a_n\check{\check{n}}^2 + a_m\check{\check{m}}^2 + \check{\check{\text{Per}}}_{\mathbf{F}}(\check{\check{n}}, \check{\check{m}}) \quad (\text{B.4})$$

$$\check{\check{\text{Per}}}_{\mathbf{F}}(1, 0) = a_n - 2a_n\check{\check{n}} + a_n\check{\check{n}}^2 + a_m\check{\check{m}}^2 + \check{\check{\text{Per}}}_{\mathbf{F}}(\check{\check{n}}, \check{\check{m}}) \quad (\text{B.5})$$

$$\check{\check{\text{Per}}}_{\mathbf{F}}(0, 1) = a_m - 2a_m\check{\check{m}} + a_n\check{\check{n}}^2 + a_m\check{\check{m}}^2 + \check{\check{\text{Per}}}_{\mathbf{F}}(\check{\check{n}}, \check{\check{m}}) \quad (\text{B.6})$$

$$\check{\check{\text{Per}}}_{\mathbf{F}}(0, 0) = a_n\check{\check{n}}^2 + a_m\check{\check{m}}^2 + \check{\check{\text{Per}}}_{\mathbf{F}}(\check{\check{n}}, \check{\check{m}}). \quad (\text{B.7})$$

By subtracting (B.5) from (B.3) and (B.6) from (B.4), this leaves

$$a_n\check{\check{n}} = \frac{\check{\check{\text{Per}}}_{\mathbf{F}}(-1, 0) - \check{\check{\text{Per}}}_{\mathbf{F}}(1, 0)}{4} \quad (\text{B.8})$$

$$a_m\check{\check{m}} = \frac{\check{\check{\text{Per}}}_{\mathbf{F}}(0, -1) - \check{\check{\text{Per}}}_{\mathbf{F}}(0, 1)}{4}. \quad (\text{B.9})$$

Also, (B.7) can be inserted into (B.3), yielding

$$\check{\check{\text{Per}}}_{\mathbf{F}}(-1, 0) = a_n + 2a_n\check{\check{n}} + \check{\check{\text{Per}}}_{\mathbf{F}}(0, 0). \quad (\text{B.10})$$

If the central summand is expressed by (B.8), this can be solved for the only unknown remaining,

$$a_n = \frac{1}{2}(\check{\check{\text{Per}}}_{\mathbf{F}}(-1, 0) + 2\check{\check{\text{Per}}}_{\mathbf{F}}(1, 0) - 2\check{\check{\text{Per}}}_{\mathbf{F}}(0, 0)). \quad (\text{B.11})$$

In an analog fashion, a_m can be determined by inserting (B.7) into (B.4) and inserting (B.9) into the result, which leaves

$$a_m = \frac{1}{2}(\check{\check{\text{Per}}}_{\mathbf{F}}(0, -1) + \check{\check{\text{Per}}}_{\mathbf{F}}(0, 1) - 2\check{\check{\text{Per}}}_{\mathbf{F}}(0, 0)). \quad (\text{B.12})$$

Going backwards, (B.11) can be inserted into (B.8) and (B.12) can be inserted into (B.9) to solve for $\check{\check{n}}$ and $\check{\check{m}}$, respectively

$$\check{\check{n}} = \frac{\check{\check{\text{Per}}}_{\mathbf{F}}(-1, 0) - \check{\check{\text{Per}}}_{\mathbf{F}}(1, 0)}{2(\check{\check{\text{Per}}}_{\mathbf{F}}(-1, 0) + \check{\check{\text{Per}}}_{\mathbf{F}}(1, 0) - 2\check{\check{\text{Per}}}_{\mathbf{F}}(0, 0))} \quad (\text{B.13})$$

$$\check{\check{m}} = \frac{\check{\check{\text{Per}}}_{\mathbf{F}}(0, -1) - \check{\check{\text{Per}}}_{\mathbf{F}}(0, 1)}{2(\check{\check{\text{Per}}}_{\mathbf{F}}(0, -1) + \check{\check{\text{Per}}}_{\mathbf{F}}(0, 1) - 2\check{\check{\text{Per}}}_{\mathbf{F}}(0, 0))} \quad (\text{B.14})$$

B Quadratic Interpolation

In order not to have to solve for a_n and a_m , insert (B.8) and (B.9) into (B.7) before solving that for $\check{\text{Per}}_{\mathbf{F}}(\check{n}, \check{m})$, which returns

$$\begin{aligned} \check{\text{Per}}_{\mathbf{F}}(\check{n}, \check{m}) &= \check{\text{Per}}_{\mathbf{F}}(0, 0) - \\ &\frac{1}{4}((\check{\text{Per}}_{\mathbf{F}}(-1, 0) - \check{\text{Per}}_{\mathbf{F}}(1, 0))\check{n} + (\check{\text{Per}}_{\mathbf{F}}(0, -1) - \check{\text{Per}}_{\mathbf{F}}(0, 1))\check{m}) \end{aligned} \quad (\text{B.15})$$

To return the equations from Section 3.3.5, the indices must be shifted back to their original position,

$$\check{n} = \hat{n} + \hat{n} \quad (\text{B.16})$$

$$\check{m} = \hat{m} + \hat{m}. \quad (\text{B.17})$$

Notations & Symbols

Notations

$(\cdot)_{k,l}$	Element at indices k, l of a matrix
\otimes	Outer product
$s(t)$	Time-continuous one-dimensional signal
$s(k)$	Time-discrete one-dimensional signal
$\text{sinc}(x)$	Normalized sinc function, $\text{sinc}(x) = \frac{\sin(\pi x)}{\pi x}$
\hat{x}	Estimate of quantity x
$\text{Re}[\cdot]$	Real part of a complex variable
$\text{var}[\cdot]$	Variance of a random variable (second central moment)
$\text{bias}[\cdot]$	Bias of the estimate of a random variable
$\text{Pr}[\cdot]$	Probability of an event

Symbols

\mathcal{A}	Modulation alphabet, e.g. QPSK	11
b	Signal attenuation (target-dependant)	20

c_0	Speed of light	21
c_{norm}	Hardware-dependant normalization factor	26
d_h	Distance of target with index h	18
f_C	Centre frequency	12
$f_{D,h}$	Doppler shift of receive signal with respect to transmit signal, caused by $v_{\text{rel},h}$	19
\mathbf{F}	Two-dimensional complex sinusoid matrix	21
\mathbf{F}_{Tx}	Transmitted OFDM frame	19
\mathbf{F}_{Rx}	Received OFDM frame	20
$G(\phi)$	Total antenna gain (transmit and receive paths) for angle ϕ	102
H	Number of backscattering objects (including clutter)	18
I	Number of interfering nodes	101
\mathbf{I}_N	Identity matrix of dimension $N \times N$	101
L	Number of multipaths for communications links	80
N	Number of active OFDM carriers	19
N_{Per}	Number of rows per two-dimensional periodogram	25
N_{max}	Number of relevant rows from the two-dimensional periodogram	30
N_{Total}	Number of available OFDM carriers (typically the IFFT length)	17
M	Number of OFDM symbols per frame	20
M_{Per}	Number of columns per two-dimensional periodogram	25
M_{max}	Number of relevant columns from the two-dimensional periodogram	30
p_D	Detection probability	99
p_F	False alarm probability	20
p_{Tx}	Transmit probability per node and timeslot	97
p_{out}	Radar network outage probability	99
P_{max}	Maximum transmit power	82
T	Duration of one OFDM symbol	13
T_G	Duration of one guard interval	14
T_O	Duration of one OFDM symbol, including guard interval	14
T_S	Sampling time (inverse of sampling frequency)	15
U	Number of orthogonal channels in the frequency domain (sub-carrier subsets)	68,97
$v_{\text{rel},h}$	Relative velocity of target with index h	19
\mathbf{w}	Tapering window vector	41
\mathbf{W}	Tapering window matrix	41

Υ	Normalized, random interference caused by network geometry (unit-less)	106
$\tilde{\Upsilon}$	Total random interference caused by network geometry (Watts)	102
Z	WGN Matrix	20
α	Path loss exponent	102
β	Constant signal attenuation (independent of targets)	102
Δf	Sub-carrier spacing	12
Δd	Range resolution	79
Δv_{rel}	Velocity resolution	79
$\Delta_{\text{abs}}x$	Absolute error of quantity x	131
$\Delta_{\text{rel}}x$	Relative error of quantity x	131
$\Gamma(\cdot)$	Gamma function	109
λ	Network density	100
σ_N	Power (variance) of thermal noise	20
σ_{RCS}	Radar cross-section	18
τ_h	Time delay of receive signal with respect to transmit signal, caused by d_h	18
φ	Phase offset	18
ϕ_h	Azimuth of target with index h	102
ϕ_0	Beam width of receiver gain	103
ω	Normalized power threshold	107
Ω	Normalized frequency, $ \Omega \leq \pi$	20

Abbreviations

ADC	Analog-to-Digital Converter
AGC	Automatic Gain Control
AWGN	Additive white Gaussian noise
BPSK	Binary Phase-Shift Keying
CFAR	Constant False Alarm Rate
CP	cyclic prefix
DAC	Digital-to-Analog Converter
DSP	Digital Signal Processor
FDMA	Frequency Division Multiple Access
FFT	Fast Fourier Transformation
FPGA	Field Programmable Gate Array
GPP	General Purpose Processor
ICI	Inter-Carrier Interference
IDFT	Inverse Discrete Fourier Transformation

IEEE	Institute of Electrical and Electronics Engineers
IFFT	Inverse Fast Fourier Transformation
ISI	Inter-Symbol Interference
LNA	Low Noise Amplifier
LO	Local Oscillator
MAC	Medium Access Control
MANET	Mobile ad-hoc network
MLE	Maximum Likelihood Estimator
OFDMA	Orthogonal Frequency Division Multiple Access
OFDM	Orthogonal Frequency Division Multiplexing
PA	Power Amplifier
PAPR	Peak-to-average Power Ratio
pdf	Probability density function
PHY	Physical Layer
PPP	Poisson Point Process
PSR	Peak-to-spur Ratio
QAM	Quadrature Amplitude Modulation
QPSK	Quadrature Phase-Shift Keying
RCS	Radar Cross Section
RMS	Root Mean Square
SIMD	Single-Instruction Multiple-Data
SNR	Signal-to-Noise Ratio
TDMA	Time Division Multiple Access
USRP	Universal Software Radio Peripheral
VANET	Vehicular ad-hoc network
WGN	white Gaussian noise
WLAN	Wireless Local Area Network

Bibliography

- [1] M. Braun, C. Sturm, A. Niethammer, and F. K. Jondral, "Parametrization of Joint OFDM-based Radar and Communication Systems for Vehicular Applications," *20th IEEE Symposium on Personal Indoor and Mobile Radio Communications*, 2009.
- [2] M. Braun, C. Sturm, and F. K. Jondral, "On the Frame Design for Joint OFDM Radar and Communications," *15th International OFDM Workshop, Hamburg*, 2010.
- [3] M. Braun and F. K. Jondral, "High-Resolution Spectral Estimation Algorithms in OFDM Radar," *16th International OFDM Workshop, Hamburg*, 2011.
- [4] M. Braun, C. Sturm, and F. K. Jondral, "Maximum Likelihood Speed and Distance Estimation for OFDM Radar," *Radar Conference, IEEE International*, 2010.
- [5] M. Braun, Y. Koch, C. Sturm, and F. K. Jondral, "Signal Design and Coding for High-Bandwidth OFDM in Car-to-Car Communications," *Vehicular Technology Conference, 2010. 72nd IEEE*, September 2010.

- [6] M. Braun, C. Sturm, and F. K. Jondral, "On the Single-Target Accuracy of OFDM Radar Algorithms," *22nd IEEE Symposium on Personal Indoor and Mobile Radio Communications*, 2011.
- [7] M. Fuhr, M. Braun, C. Sturm, L. Reichardt, and F. K. Jondral, "An SDR-based Experimental Setup for OFDM-based Radar," *Proceedings of the 7th Karlsruhe Workshop on Software Radio Karlsruhe*, March 2012.
- [8] M. Braun, M. Fuhr, M. Braun, and F. K. Jondral, "A USRP-based Testbed for OFDM-based Radar and Communication Systems," *Proceedings of 22nd Virginia Tech Symposium on Wireless Communications, Blacksburg*, June 2012.
- [9] M. Braun, M. Fuhr, and F. K. Jondral, "Spectral Estimation-based OFDM Radar Algorithms for IEEE 802.11a Signals," *Vehicular Technology Conference, 2012. 76nd IEEE*, September 2012.
- [10] M. Braun, R. Tanbourgi, and F. K. Jondral, "Co-Channel Interference Limitations of OFDM Radar Networks," *IEEE Transaction on Vehicular Technology*.
- [11] J. Fink, M. Braun, and F. K. Jondral, "Effects of Arbitrarily Spaced Subcarriers on Detection Performance in OFDM Radar," *Vehicular Technology Conference, 2012. 76nd IEEE*, September 2012.
- [12] C. Sturm, T. Zwick, and W. Wiesbeck, "An OFDM System Concept for Joint Radar and Communications Operations," *Vehicular Technology Conference, 2009. 69th IEEE*, April 2009.
- [13] C. Sturm, E. Pancera, T. Zwick, and W. Wiesbeck, "A Novel Approach to OFDM Radar Processing," *Radar Conference, IEEE*, May 2009.
- [14] C. Sturm, M. Braun, T. Zwick, and W. Wiesbeck, "Performance Verification of Symbol-Based OFDM Radar Processing," *Radar Conference, IEEE International*, 2010.
- [15] —, "A Multiple Target Doppler Estimation Algorithm for OFDM based Intelligent Radar Systems," *7th European Radar Conference*, 2010.

- [16] C. Sturm, M. Braun, and W. Wiesbeck, "Deterministic Propagation Modeling for Joint Radar and Communication Systems," in *Proceedings 2010 International Symposium on Electromagnetic Theory*, Aug 2010.
- [17] C. Sturm, L. Reichardt, T. Zwick, and W. Wiesbeck, "Evaluation of beam-forming algorithms for automotive OFDM signal based radar," in *Proceedings of the European Radar Conference EuRAD 2009*, Rome, Sept 2009, pp. 141–144, 2009.09.30.
- [18] C. Sturm, "Gemeinsame Realisierung von Kommunikation und Radar auf Basis von OFDM," Ph.D. dissertation, Karlsruhe Institute of Technology, 2011, available online at www.ubka.uni-karlsruhe.de.
- [19] C. Sturm and W. Wiesbeck, "Waveform Design and Signal Processing Aspects for Fusion of Wireless Communications and Radar Sensing," *Proceedings of the IEEE*, vol. 99, no. 7, pp. 1236–1259, July 2011.
- [20] Y. Sit, L. Reichardt, C. Sturm, and T. Zwick, "Extension of the OFDM joint radar-communication system for a multipath, multiuser scenario," in *Radar Conference (RADAR), 2011 IEEE*, may 2011, pp. 718–723.
- [21] C. Sturm, Y. L. Sit, M. Braun, and T. Zwick, "Spectrally Interleaved Multi-Carrier Signals for Radar Network Applications and MIMO-Radar," *IET Radar, Sonar and Navigation*, 2012.
- [22] L. Cheng, B. Henty, R. Cooper, D. Standi, and T. F. Bai, "A Measurement Study of Time-Scaled 802.11a Waveforms Over The Mobile-to-Mobile Vehicular Channel at 5.9 GHz," *Communications Magazine, IEEE*, vol. 46, no. 5, pp. 84–91, May 2008.
- [23] M. Takeda, T. Terada, and R. Kohno, "Spread spectrum joint communication and ranging system using interference cancellation between a roadside and a vehicle," *Vehicular Technology Conference, 1998. VTC 98. 48th IEEE*, vol. 3, pp. 1935–1939 vol.3, May 1998.
- [24] H. Zhang, L. Li, and K. Wu, "24GHz Software-Defined Radar System for Automotive Applications," *Wireless Technologies, 2007 European Conference on*, pp. 138–141, Oct. 2007.

- [25] C. Cseh, R. Eberhardt, and W. Franz, “Mobile Ad-Hoc Funknetze für die Fahrzeug-Fahrzeug-Kommunikation,” *1. Deutscher Workshop über Mobile Ad Hoc Netze, WMAN 2002, Ulm, March 2002*.
- [26] “Forschungsinitiative Ko-FAS,” *www.kofas.de*.
- [27] T. Schipper, J. Fortuny-Guasch, D. Tarchi, L. Reichardt, and T. Zwick, “RCS measurement results for automotive related objects at 23-27 GHz,” in *Antennas and Propagation (EUCAP), Proceedings of the 5th European Conference on*, april 2011, pp. 683–686.
- [28] P. Papadimitratos, A. La Fortelle, K. Evenssen, R. Brignolo, and S. Cosenza, “Vehicular communication systems: Enabling technologies, applications, and future outlook on intelligent transportation,” *Communications Magazine, IEEE*, vol. 47, no. 11, pp. 84–95, 2009.
- [29] K. Dar, M. Bakhouya, J. Gaber, M. Wack, and P. Lorenz, “Wireless communication technologies for ITS applications [Topics in Automotive Networking],” *Communications Magazine, IEEE*, vol. 48, no. 5, pp. 156–162, 2010.
- [30] E. Ström, H. Hartenstein, P. Santi, and W. Wiesbeck, “Vehicular Communications: Ubiquitous Networks for Sustainable Mobility [Point of View],” *Proceedings of the IEEE*, vol. 98, no. 7, pp. 1111–1112, 2010.
- [31] P. Belanovic, D. Valerio, A. Paier, T. Zemen, F. Ricciato, and C. Mecklenbrauker, “On Wireless Links for Vehicle-to-Infrastructure Communications,” *Vehicular Technology, IEEE Transactions on*, vol. 59, no. 1, pp. 269–282, 2010.
- [32] G. Karagiannis, O. Altintas, E. Ekici, G. Heijenk, B. Jarupan, K. Lin, and T. Weil, “Vehicular networking: A survey and tutorial on requirements, architectures, challenges, standards and solutions,” *Communications Surveys & Tutorials, IEEE*, vol. 13, no. 4, pp. 584–616, 2011.
- [33] N. Dinur and D. Wulich, “Peak-to-Average Power Ratio in high-order OFDM,” *Communications, IEEE Transactions on*, vol. 49, no. 6, pp. 1063–1072, Jun 2001.

- [34] P. Robertson and S. Kaiser, "Analysis of Doppler Spread Perturbations in OFDM(A) Systems," *European Transactions on Telecommunications*, vol. 11, pp. 585–592, Nov./Dec. 2000.
- [35] G. E. A. Franken, H. Nikookar, and P. van Genderen, "Doppler tolerance of OFDM coded Radar Signals," *Proc. 3rd European Radar Conference*, pp. 108–111, Sep 2006.
- [36] B. Donnet and I. Longstaff, "Combining MIMO Radar with OFDM Communications," *Radar Conference, 2006. EuRAD 2006. 3rd European*, pp. 37–40, Sept. 2006.
- [37] Y. Paichard, "OFDM Waveforms for Multistatic Radars," *Radar Conference, IEEE International*, May 2010.
- [38] P. Falcone, F. Colone, C. Bongioanni, and P. Lombardo, "Experimental results for OFDM WiFi-based passive bistatic radar," in *Radar Conference, 2010 IEEE*, May 2010.
- [39] D. Garmatyuk, J. Schuerger, Y. Morton, K. Binns, M. Durbin, and J. Kimani, "Feasibility study of a multi-carrier dual-use imaging radar and communication system," in *Radar Conference, 2007. EuRAD 2007. European*, 2007, pp. 194–197.
- [40] D. Garmatyuk and J. Schuerger, "Conceptual design of a dual-use radar/communication system based on OFDM," in *Military Communications Conference, 2008. MILCOM 2008. IEEE*, 2008, pp. 1–7.
- [41] D. Garmatyuk, J. Schuerger, K. Kauffman, and S. Spalding, "Wideband OFDM system for radar and communications," in *Radar Conference, 2009 IEEE*, 2009, pp. 1–6.
- [42] D. Garmatyuk and K. Kauffman, "Radar and data communication fusion with UWB-OFDM software-defined system," in *Ultra-Wideband, 2009. ICUWB 2009. IEEE International Conference on*, 2009, pp. 454–458.
- [43] J. Schuerger and D. Garmatyuk, "Performance of random OFDM radar signals in deception jamming scenarios," in *Radar Conference, 2009 IEEE*, 2009, pp. 1–6.
- [44] D. Garmatyuk, J. Schuerger, and K. Kauffman, "Multifunctional Software-Defined Radar Sensor and Data Communication System," *Sensors Journal, IEEE*, vol. 11, no. 1, pp. 99–106, 2011.

- [45] L. Reichardt, C. Sturm, F. Grunhaupt, and T. Zwick, “Demonstrating the use of the IEEE 802.11P Car-to-Car communication standard for automotive radar,” in *Antennas and Propagation (EUCAP), 2012 6th European Conference on*, 2012, pp. 1576–1580.
- [46] N. Levanon, “Multifrequency radar signals,” in *Radar Conference, 2000. The Record of the IEEE 2000 International*, 2000, pp. 683–688.
- [47] Q. Pu, S. Jiang, and S. Gollakota, “Whole-home gesture recognition using wireless signals,” in *Proceedings of the ACM SIGCOMM 2013 conference on SIGCOMM*. ACM, 2013, pp. 485–486.
- [48] A. Capria, M. Conti, D. Petri, M. Martorella, F. Berizzi, E. Dalle Mese, R. Soleti, and V. Carulli, “Ship detection with DVB-T software defined passive radar,” in *IEEE Gold Remote Sensing Conference*, 2010.
- [49] J. Wenger, “Automotive mm-wave radar: status and trends in system design and technology,” in *Automotive Radar and Navigation Techniques (Ref. No. 1998/230), IEE Colloquium on*, 1998, pp. 1/1–1/7.
- [50] B. Schöne, “Schutzengel aus Silizium,” *Die Welt*, p. 24, December 2012.
- [51] R. Stevenson, “A driver’s sixth sense,” *Spectrum, IEEE*, vol. 48, no. 10, pp. 50–55, 2011.
- [52] H. Groll and J. Detlefsen, “History of automotive anticollision radars and final experimental results of a mm-wave car radar developed on the Technical University of Munich,” in *Radar, 1996. Proceedings., CIE International Conference of*, 1996, pp. 13–17.
- [53] S. Yi and Y. Pei, “On the Capacity Improvement of Ad Hoc Wireless Networks Using Directional Antennas,” 2003.
- [54] R. Ramanathan, “On the Performance of Ad Hoc Networks with Beamforming Antennas,” In *2nd ACM MobiHoc*, 2001.
- [55] S. Eichler, “Performance Evaluation of the IEEE 802.11p WAVE Communication Standard,” in *Vehicular Technology Conference, 2007 Fall. IEEE 66th*, 30 2007-Oct. 3 2007.

- [56] Y. Wang, A. Ahmed, B. Krishnamachari, and K. Psounis, "IEEE 802.11p performance evaluation and protocol enhancement," in *Vehicular Electronics and Safety, 2008. IEEE International Conference on*, Sept. 2008.
- [57] *IEEE 802.11 Standard, Part 11*, 2005.
- [58] *IEEE 802.11 Standard, Part 11*, 2005.
- [59] J. Tsao and B. Steinberg, "Reduction of sidelobe and speckle artifacts in microwave imaging: the CLEAN technique," *Antennas and Propagation, IEEE Transactions on*, vol. 36, no. 4, pp. 543–556, 1988.
- [60] "More Safety for All by Radar Interference Mitigation (MOSARIM). 7th Frame EU-Project, FP7/2007-2013." [Online]. Available: <http://www.mosarim.eu>
- [61] T. M. Consortium, "Study on the state-of-the-art interference mitigation techniques," *Work Package 1, General Interference Risk Assessment*, 2010.
- [62] J. Karedal, F. Tufvesson, N. Czink, A. Paier, C. Dumard, T. Zemen, C. Mecklenbrauker, and A. Molisch, "A geometry-based stochastic MIMO model for vehicle-to-vehicle communications," *Wireless Communications, IEEE Transactions on*, vol. 8, no. 7, pp. 3646–3657, 2009.
- [63] L. Reichardt, J. Maurer, T. Fügen, and T. Zwick, "Virtual Drive: A Complete V2X Communication and Radar System Simulator for Optimization of Multiple Antenna Systems," *Proceedings of the IEEE*, vol. 99, no. 7, pp. 1295–1310, 2011.
- [64] M. Hischke, "Collision warning radar interference," in *Intelligent Vehicles '95 Symposium., Proceedings of the*, 1995, pp. 13–18.
- [65] M. Goppelt, H.-L. Blocher, and W. Menzel, "Analytical investigation of mutual interference between automotive FMCW radar sensors," in *Microwave Conference (GeMIC), 2011 German*, 2011, pp. 1–4.
- [66] M. Goppelt, H.-L. Blöcher, and W. Menzel, "Automotive radar - Investigation of mutual interference mechanisms," *Advances in Radio Science*, vol. 8, pp. 55–60, 2010. [Online]. Available: <http://www.adv-radio-sci.net/8/55/2010/>

- [67] G. Brooker, "Mutual interference of millimeter-wave radar systems," *Electromagnetic Compatibility, IEEE Transactions on*, vol. 49, no. 1, pp. 170–181, 2007.
- [68] T. Schipper, M. Harter, L. Zwirello, T. Mahler, and T. Zwick, "Systematic approach to investigate and counteract interference-effects in automotive radars," in *Radar Conference (EuRAD), 2012 9th European*, 2012, pp. 190–193.
- [69] D. Oprisan and H. Rohling, "Analysis of mutual interference between automotive radar systems," in *Proc. International Radar Symposium*, 2005, p. 84.
- [70] D. Shnidman, "The calculation of the probability of detection and the generalized Marcum Q-function," *Information Theory, IEEE Transactions on*, vol. 35, no. 2, pp. 389–400, Mar 1989.
- [71] H. Fussler, J. Widmer, M. Mauve, and H. Hartenstein, "A novel forwarding paradigm for position-based routing (with implicit addressing)," in *Computer Communications, 2003. CCW 2003. Proceedings. 2003 IEEE 18th Annual Workshop on*, Oct. 2003, pp. 194–200.
- [72] J. Maurer, "Strahlenoptisches Kanalmodell für die Fahrzeug-Fahrzeug-Funkkommunikation," Ph.D. dissertation, Karlsruhe, 2005, available online at www.ubka.uni-karlsruhe.de.
- [73] National instruments / ettus research llc website. [Online]. Available: www.ettus.com
- [74] Maxim MAX2829 datasheet. [Online]. Available: www.maxim-ic.com
- [75] J. C. Lagarias, J. A. Reeds, M. H. Wright, and P. E. Wright, "Convergence Properties of the Nelder-Mead Simplex Method in Low Dimensions," *SIAM Journal of Optimization*, vol. 9, no. 1, pp. 112–147, 1998.
- [76] A. . B. Labs, "Army Ordnance Guided Missile Job," *Case Files*, 1944.
- [77] R. Cager, D. LaFlame, and L. Parade, "Orbiter Ku-Band Integrated Radar and Communications Subsystem," *Communications, IEEE Transactions on*, vol. 26, no. 11, pp. 1604–1619, 1978.

- [78] W. Wiesbeck, "SDRS: Software Defined Radar Sensors," *IEEE International Geoscience and Remote Sensing Symposium (IGARSS'01), Sydney, Australia.*, pp. 3259–3261, 2001.
- [79] S. Bundesamt, "Verkehr Aktuell Stand 30.7.2013, Fachserie 8 Reihe 1.1," 2013.
- [80] W. H. Organization, "Estimated total deaths in 2002, by cause and WHO member state," 2004.
- [81] J. A. Davis and J. Jedwab, "Peak-to-mean power control in OFDM, Golay complementary sequences and Reed-Muller codes," *IEEE Transactions on Information Theory*, vol. 45, no. 7, November 1999.
- [82] B. Popovic, "Synthesis of power efficient multitone signals with flat amplitude spectrum," *IEEE Transactions on Communications*, vol. 39, no. 1, July 1991.
- [83] F. MacWilliams and N. Sloane, *The Theory of Error-Correcting Codes*. North-Holland Mathematical Library, 1977.
- [84] "Error correcting codes : proceedings of a symposium, conducted by the mathematics research center, united states army, at the univ. of wisconsin, madison, may 6 - 8, 1968," ser. Publications of the Mathematics Research Center ; 21, H. B. H. Mann, Ed. New York: Wiley, 1968.
- [85] S. M. Kay, *Modern Spectral Estimation*. Prentice Hall, 1988.
- [86] P. G. Stoica and R. L. Moses, *Introduction to spectral analysis*. Upper Saddle River, NJ: Prentice Hall, 1997.
- [87] D. Rife and R. Boorstyn, "Single tone parameter estimation from discrete-time observations," *Information Theory, IEEE Transactions on*, vol. 20, no. 5, pp. 591–598, Sep 1974.
- [88] R. Schmidt, "Multiple Emitter Location and Signal Parameter Estimation," *Antennas and Propagation, IEEE Transactions on*, vol. 34, no. 3, pp. 276 – 280, Mar. 1986.
- [89] A. Barabell, "Improving the Resolution Performance of Eigenstructure-based Direction-finding Algorithms," in *Acoustics, Speech, and Signal Processing, IEEE International Conference on ICASSP '83.*, vol. 8, Apr. 1983, pp. 336 – 339.

- [90] J. Li and P. Stoica, “Efficient mixed-spectrum estimation with applications to target feature extraction,” *Signal Processing, IEEE Transactions on*, vol. 44, no. 2, pp. 281–295, Feb 1996.
- [91] P. Stoica, P. Babu, and J. Li, “New Method of Sparse Parameter Estimation in Separable Models and Its Use for Spectral Analysis of Irregularly Sampled Data,” *IEEE Transactions on Signal Processing*, vol. 59, no. 1, pp. 35–47, Jan. 2011.
- [92] P. Babu and P. Stoica, “Spectral analysis of nonuniformly sampled data – a review,” *Digital Signal Processing*, vol. 20, pp. 359–378, 2010.
- [93] B. Sklar, *Digital Communications: Fundamentals and Applications*. Prentice Hall.
- [94] R. van Nee and R. Prasad, *OFDM for wireless multimedia communications*. Artech House, 2000.
- [95] R. Roy, A. Paulraj, and T. Kailath, “ESPRIT—A subspace rotation approach to estimation of parameters of cisoids in noise,” *Acoustics, Speech and Signal Processing, IEEE Transactions on*, vol. 34, no. 5, pp. 1340–1342, Oct. 1986.
- [96] J. Gansman, M. Zoltowski, and J. Krogmeier, “2-D angle estimation in beamspace featuring multidimensional multirate eigenvector processing,” in *Signals, Systems and Computers, 1994. 1994 Conference Record of the Twenty-Eighth Asilomar Conference on*, vol. 2, 1994, pp. 785–789 vol.2.
- [97] M. I. E. Skolnik, Ed., *Radar handbook*, 2nd ed. Norwich, NY: Knovel, 2003.
- [98] M. A. Richards, Ed., *Principles of Modern Radar*. Raleigh, NC: SciTech Publ.
- [99] K.-D. Kammeyer, *Nachrichtenübertragung*, 5th ed., M. Bossert, Ed. Wiesbaden: Vieweg + Teubner, 2011.
- [100] A. Goldsmith, *Wireless communications*. Cambridge University Press, 2005.
- [101] J. O. Smith, *Spectral Audio Signal Processing*, accessed 24 March 2012, online book.

- [102] K.-D. Kammeyer and K. Kroschel, *Digitale Signalverarbeitung : Filterung und Spektralanalyse; mit MATLAB-Übungen; mit 35 Tab.*, 5th ed. Stuttgart: Teubner, 2002.
- [103] M. Engels, Ed., *Wireless OFDM systems: how to make them work?* Kluwer Academic Publ., 2002.
- [104] L. Hanzo, Ed., *OFDM and MC-CDMA for broadband multi-user communications, WLANs and broadcasting.* Wiley, 2003.
- [105] A. V. Oppenheim, R. W. Schaffer, and J. R. Buck, *Discrete-time signal processing*, 2nd ed., ser. Prentice Hall signal processing series. Upper Saddle River, NJ: Prentice Hall, 1999.
- [106] W. Hengartner and R. Theodorescu, *Einführung in die Monte-Carlo-Methode.* Carl Hanser Verlag, 1978.
- [107] J. G. Proakis, *Digital communications*, 4th ed., ser. McGraw-Hill series in electrical and computer engineering. Boston [u.a.]: McGraw-Hill, 2001.
- [108] R. G. Lyons, *Understanding digital signal processing*, 3rd ed. Upper Saddle River, NJ [u.a.]: Prentice Hall, 2011.
- [109] M. Pätzold, *Mobilfunkkanäle: Modellierung, Analyse und Simulation.* Braunschweig: Vieweg, 1999.
- [110] N. Geng and W. Wiesbeck, *Planungsmethoden für die Mobilkommunikation : Funknetzplanung unter realen physikalischen Ausbreitungsbedingungen.* Berlin: Springer, 1998.
- [111] Bundesnetzagentur, “Allgemeinzuteilung von Frequenzen für nichtöffentliche Funkanwendungen geringer Reichweite; Non-specific Short Range Devices (SRD),” *Verfügung 76/2003*, 2003.
- [112] F. Jondral, *Nachrichtensysteme.* J. Schlembach Fachverlag, 2001.
- [113] D. Stoyan, W. Kendall, and J. Mecke, *Stochastic geometry and its applications*, 2nd ed. Wiley, 1995.
- [114] A. Baddeley, “Spatial Point Processes and their Applications,” in *Stochastic Geometry: Lectures given at the C.I.M.E. 2004*, ser. Lecture Notes in Mathematics 1892. Springer Verlag, 2006, pp. 1–75.

- [115] S. Weber, X. Yang, J. Andrews, and G. de Veciana, “Transmission Capacity of Wireless Ad Hoc Networks with Outage Constraints,” *IEEE Trans. Inf. Theory*, Aug. 2005.
- [116] F. Baccelli and B. Blaszczyszyn, “Stochastic Geometry and Wireless Networks, Volume 1+2: Theory and Applications,” *Foundations and Trends in Networking*, 2009.
- [117] A. Gut, *Probability: a graduate course*, ser. Springer Texts in Statistics. New York, NY: Springer, 2005.
- [118] J. Andrews, R. Ganti, M. Haenggi, N. Jindal, and S. Weber, “A primer on spatial modeling and analysis in wireless networks,” *IEEE Commun. Magazine*, vol. 48, no. 11, pp. 156–163, Nov. 2010.

Supervised Theses

- [119] M. Müller, “Software Radio-basierte Implementierung von OFDM-Radar Algorithmen,” Bachelor’s thesis, Karlsruhe Institute of Technology, 2012.
- [120] S. Hoscheid, “Analyse eines Systems fusionierter Fahrzeug-Fahrzeug-Kommunikation und Radarsensorik,” Master’s thesis, Karlsruhe Institute of Technology, 2011.
- [121] N. Otterbach, “Anwendung von Reed-Muller Codes bei OFDM-basierter Datenübertragung,” Bachelor’s thesis, Karlsruhe Institute of Technology, 2011.
- [122] M. Plock, “Implementierung von Relay-Netzen auf Software Radio Basis,” Studienarbeit, Karlsruhe Institute of Technology, 2011.
- [123] T. Schu, “Parametrische Methoden für OFDM-basiertes Radar,” Diplomarbeit, Karlsruhe Institute of Technology, 2011.
- [124] M. Linde, “Analyse und Synthese von Mobilfunkkanälen für die Fahrzeug-Fahrzeug Kommunikation,” Diplomarbeit, Karlsruhe Institute of Technology, 2009.

- [125] T. Mönicke, “Software Radio-basierte Detektion und Rahmenschätzung beim Empfang von GSM Datenpaketen,” Bachelor’s thesis, Karlsruhe Institute of Technology, 2010.
- [126] A. Niethammer, “Untersuchungen zur Synchronisation breitbandiger OFDM-Übertragung,” Diplomarbeit, Karlsruhe Institute of Technology, 2010.
- [127] T. Mönicke, “Aufbau und Evaluation einer Cell BE-basierten SDR Plattform,” Studienarbeit, Karlsruhe Institute of Technology, 2010.
- [128] Y. Koch, “Untersuchung von Codierungsverfahren für breitbandige OFDM-Übertragung,” Diplomarbeit, Karlsruhe Institute of Technology, 2010.
- [129] R. M. Estrem, “Implementation of a Cognitive Radio Handshake Protocol,” Master’s thesis, Karlsruhe Institute of Technology, 2010.
- [130] I. Karle, “Aufbau einer Messeinrichtung für mobile OFDM-Übertragung,” Studienarbeit, Karlsruhe Institute of Technology, 2010.
- [131] K. Nagaraj, “Wireless Networks in-the-loop: Software Radio as the Enabler,” Master’s thesis, Karlsruhe Institute of Technology, 2009.
- [132] M. Fischer, “Demonstration eines Konzepts zur Over-the-air Rekonfiguration für Cognitive Radio Terminals,” Bachelor’s thesis, Karlsruhe Institute of Technology, 2011.
- [133] A. Niethammer, “Rahmenentwurf für OFDM-basierte Fahrzeug-Fahrzeug-Kommunikation,” Studienarbeit, Karlsruhe Institute of Technology, 2010.
- [134] S. Ehrhard, M. Fischer, M. Fuhr, M. Mouazzen, M. Müller, and M. L. Schulz, “Spektralschätzung mit MUSIC und ESPRIT,” Team project, Karlsruhe Institute of Technology, 2011.
- [135] C. Kaiser, “Zyklische Spektralschätzung in GNU Radio,” Bachelor’s thesis, Karlsruhe Institute of Technology, 2011.

- [136] R. D. Billerbeck, “Fusion von Algorithmen für OFDM-Radar auf Basis von Spektralschätzung,” Bachelor’s thesis, Karlsruhe Institute of Technology, 2011.
- [137] S. Koslowski, “Emulation einer RF-Hardware für Software Radios,” Studienarbeit, Karlsruhe Institute of Technology, 2010.
- [138] T. Lutz, “Optimization of OFDM Radar Algorithms by Means of Tracking,” Diplomarbeit, Karlsruhe Institute of Technology, 2011.
- [139] J. Fink, “Optimale Schätzalgorithmen für OFDM-Radar mit zufälligen Unterträgern,” Diplomarbeit, Karlsruhe Institute of Technology, 2011.
- [140] M. Fuhr, “Zeit- und Frequenzsynchronisation von Software Defined Radio Terminals als Basis für OFDM-Radar Systeme,” Bachelor’s thesis, Karlsruhe Institute of Technology, 2011.
- [141] J. Eisenbeis, “Integration von Kommunikationsmessungen in die OFDM-Radar-Umgebung,” Bachelor’s thesis, Karlsruhe Institute of Technology, 2012.
- [142] N. Otterbach, “Evaluierung der Wireless Networks in-the-loop Methode für Cognitive Radios,” Master’s thesis, Karlsruhe Institute of Technology, 2013.

Index

- auto-covariance matrix, 73
- car-to-car communication, 5
- centre frequency, 12
- CFAR, *see* constant false alarm rate
- clutter, 131
- code rate, 92
- coherence bandwidth, 82
- collision, 95
- complex periodogram, 25
- constant false alarm rate, 53
- Cramér-Rao lower bound, 34, 135
 - averaged, 35
- delay spread, 81
- detection probability, 99
- detector loss, 119, 143
- Doppler spread, 81
- ESPRIT, 72
- estimator
 - bias, 39
 - maximum likelihood, 31
 - parametric, 72
 - variance, 39
- fading parameters, 102
- implementation
 - parallel, 31
 - serialized, 31
- intelligent transportation systems,
 - 5
- inter-carrier interference, 82
- inter-symbol interference, 81
- interpolation, 48
 - by optimization, 50
 - linear, 49
 - quadratic, 50
- irregular sampling, 70
- MANETs, 5
- Marcum Q-function, 38

- maximum excess delay, 81
- maximum likelihood estimator,
 - 31
- monostatic radar, 18
- multipath propagation channel,
 - 80
- mutual interference, 8

- noise power density, 27
- noise power estimation, 55

- OFDM
 - cyclic prefix, 14, 81
 - DC carrier, 62
 - frame, 13
 - frame structure, 90
 - orthogonality, 13
 - PAPR, 16
 - physical structure, 11
 - radar network, 95
 - received frame matrix, 19
 - sub-carrier spacing, 82
- outage probability, 99
 - lower bound, 107
 - upper bound, 110

- path loss, 106
- peak-to-spur ratio, 67
- perfect detector, 117
- periodogram
 - irregular, 70
 - two-dimensional, 25
- platooning, 6
- point-scatter model, 26
- PPP, 101
- processing gain, 29
- PSR, 67

- quantization error, 34, 45, 138
- quantization noise, 47

- radar
 - combined with communication, 9
 - passive, 2
 - vehicular, 6
- radar imaging, 18
- radar network outage, 98
- range resolution, 79
- received frame matrix, 19
- Reed-Muller codes, 92
- reference target, 98
- roadside units, 90

- sampling rate, 14
- scalloping loss, 47
- signal constraints, 79
- signal requirements, 79
- signal subspace, 73
- signal-to-noise ratio, 26
- SIMD, 31
- simulations, 121
- SNR, 26
- software radio, 126
- spatial randomness, 101
- sub-carrier allocation, 62
 - random, 69
 - regular, 68
- successive target cancellation, 56
 - binary, 56
 - coherent, 59
 - residual, 59

- thermal noise, 27
- transmit frame matrix, 19

- unambiguous range, 24, 80
- USRP, 126

- VANETs, 5
- velocity resolution, 79

window
 Blackman-Harris, 44
 Dolph-Chebyshev, 44
 Hamming, 43
 rectangular, 43
 SNR loss, 45
window functions, 41